



Zentrum für optische Technologien – ZOT

Optische Messtechnik - OMT

Investigation of defined Layer  
Generation for Projection Micro  
Stereolithography (P $\mu$ SL) via  
the Deep Dip Method

A Master Thesis

In Partial Fulfilment for the Degree of

Master of Science

(M.Sc.)

By Hannes Suhr, B. Eng

56935

31<sup>st</sup> of January 2022

1<sup>st</sup> Auditor: Prof. Dr. Andreas Heinrich

2<sup>nd</sup> Auditor: Prof. Dr. Rainer Börret

## I Affidavit

I affirm that I have produced the work independently and without the use of any aids other than those specified. All passages taken literally or in spirit from publications or other sources are marked as such. This paper has not yet been submitted to any examination office in the same or similar form and has not yet been published.



---

Aalen, 31<sup>st</sup> of January 2022

(Hannes Suhr)

## II Acknowledgement

Hereby I want to thank my family for enabling me the opportunity to accomplish my master's degree. Furthermore, I want to thank my great colleagues and friends for helping and guiding me throughout this endeavour.

### III Abstract

The layer generation with the Deep Dip Method for projection micro stereolithography in the realm of additive manufacturing lacks significant research. As a result, this thesis presents an investigation into this method of layer generation for a planned projection micro stereolithography system to print defined layers. Therefore, a confocal chromatic measurement setup was developed allowing the measurement of the PR48 liquid photopolymer layer formation with the Deep Dip method. Here, a parameter analysis was conducted finding multiple influences of different parameters regarding the maximum layer height as well as the radius of curvature of the liquid layers under ambient conditions. Furthermore, the influence of the viscosity onto layer formation was investigated in more detail, by heating the liquid photopolymer. Additionally, an first empirically modified model was proposed to fit the observed measurements and to forecast the layer generation process.

---

## IV Table of Contents

List of Abbreviations .....	8
1. Introduction .....	9
1.1. Background .....	9
1.2. State of the Art .....	12
1.3. Goals .....	15
2. Theoretical Background .....	17
2.1. Additive Manufacturing .....	17
2.1.1. Projection Micro Stereolithography (PμSL) .....	19
2.1.2. Digital Light Processing .....	22
2.2. Layer Generation .....	24
2.2.1. Layer Generation Methods .....	24
2.2.2. Deep Dip Method .....	27
2.2.3. Layer Measurement Methods .....	32
2.2.4. Chromatic Confocal Measurement Principle .....	33
2.3. Photopolymers .....	37
2.3.1. Photopolymerisation .....	37
2.3.2. Oxygen Inhibition .....	39
2.3.3. Printing Resolution .....	40
2.3.4. Rheological Properties .....	40
2.4. Mathematical Model of Drop Spreading .....	43
3. Experiments .....	53
3.1. PμSL Setup .....	55
3.2. Setup for Deep Dip Analysis .....	56
3.3. Software for Controlling Measurement Setup .....	60

---

3.4.	Validation measurements.....	61
3.4.1.	Movement Validation Z-Axis.....	62
3.4.2.	Confocal Sensor Test.....	64
4.	Experiment Methodology.....	67
4.1.	Layer Measurement Methods.....	68
4.1.1.	Confocal Sensor Scan.....	68
4.1.2.	Data Post Processing and Extraction.....	70
5.	Layer Generation with Deep Dip Method.....	79
5.1.	Motivation and Goal.....	79
5.2.	Methodology.....	79
5.3.	Results.....	83
5.4.	Discussion.....	92
6.	Extension of the Setup with a Heated Resin Vat.....	106
6.1.	Motivation and Goal.....	106
6.2.	Heated Resin Vat Setup.....	106
6.3.	Heated Resin Vat Software.....	109
6.4.	Changes to the Experimental Setup.....	110
6.5.	Validation Measurements.....	111
6.5.1.	PR48 Viscosity Measurement.....	111
6.5.2.	Refractometer Measurements PR48.....	113
6.5.3.	Temperature Sensor Calibration.....	114
6.5.4.	PID tuning Measurements.....	116
6.5.5.	Resin Vat point temperature measurement.....	118
6.6.	Methodology.....	121
6.7.	Results.....	123
6.8.	Discussion.....	124
7.	Mathematical Model.....	128

---

---

7.1.	Motivation and Goal.....	128
7.2.	Methodology .....	128
7.3.	Results .....	132
7.4.	Discussion .....	138
8.	Summary and Discussion .....	142
9.	Outlook .....	146
10.	References.....	147
11.	Table of Figures .....	152
	Appendices .....	160
	Specifications - Confocal Sensor - ICF2461.....	160
	Specifications - Confocal Optical Head – IFS2405-1 .....	161
	Specifications – Stage - XMS-50S .....	162
	Specifications – Stage- GTS30V.....	163
	Specifications – Controller – XPS D4 .....	164
	Specifications - Refractometer DR 6000.....	165
	Specifications – Temperature Sensor - DS18B20 .....	166
	Specifications – Heating Foils - .....	167
	Specifications – Peltier-Element - .....	168
	Specifications – Temperature Sensor – Trotec T210.....	169
	Specifications – DC Powersupply – HP E3610 A.....	170

## List of Abbreviations

Acrylonitrile Butadiene Styrene	ABS
Additive Manufacturing	AM
Build platform to Resin vat ratio	BP to RV ratio
Continuous Liquid Interface Production	CLIP
Complementary Metal-Oxide-Semiconductor	CMOS
Deep Dip Offset	DDD
Deep Dip Offset	DDO
Digital Light Processing	DLP
Digital Mirror Device	DMD
Fused Deposition Modelling	FDM
Graphical User Interface	GUI
Large Area Projection Micro Stereolithography	LAP $\mu$ SL
Liquid Crystal Display	LCD
Liquid Crystal on Silicon (LCoS)	LCoS
Light Emitting Diode	LED
Microelectromechanical System	MEMS
Metal-Oxide-Semiconductor-Field Effect-Transistor	MOSFET
Polycarbonate	PC
Partial Differential Equation	PDE
Polylactic Acid	PLA
Polyphenylsulfone	PPSF
Projection Micro Stereolithography	P $\mu$ SL
Pulse Width Modulation	PWM
Radius of Curvature	ROC
Stereolithography	SLA
Spatial Light Modulator	SLM
Shape Memory Alloy	SMA
Two Photon Absorption	TPA
Two Photon Polymerisation	TPP
Ultraviolet	UV
Volume of Fraction	VOF

# 1. Introduction

This chapter will give the reader an introduction to the background and goal of this thesis. The increasing interest in projection micro stereolithography (P $\mu$ SL) in the realm of additive manufacturing (AM) for microfabrication shall be explained in 1.1. Furthermore, the importance of research in recoating methods for P $\mu$ SL will be drawn up in 1.2. Finally, the goals of this work are formulated in 1.3.

## 1.1. Background

AM is a collection of techniques that allow real objects to be quickly created layer-by-layer from computer-generated models. A manual or traditional technique such as milling or routing of a workpiece can also be used to build a physical model, but such models require long manufacturing times, high costs, and much labour. A new set of additive manufacturing technologies has been developed to solve these difficulties over the last ten years.

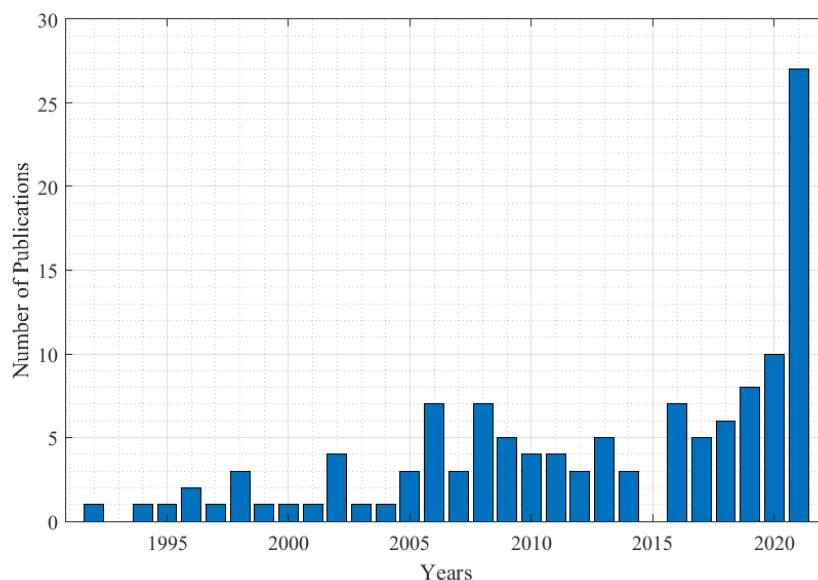


Figure 1-1: The increasing number of publications to a search in Web of Science platform for the keywords "projection micro stereolithography," "PuSL", "P mu SL", "projection microsterolithography" and "Stereolithography DLP".

One of those new AM techniques is P $\mu$ SL, which can produce 3D objects with complex shapes and exquisite details at a far higher resolution than other AM techniques like fused deposition modelling (FDM). Here, UV-light is projected onto build platform submerged in a photopolymer in a resin vat and is subsequently cured. The irradiation pattern is generated via a spatial light modulator (SLM) and is downscaled with a optical system allowing for a resolution in the micrometre range. Additionally, in P $\mu$ SL models are build layer-by-layer and new layers must be generated. Fast prototyping and microengineering applications could benefit from this process [1, p. 102]. A keyword search in Web of Science for P $\mu$ SL results in the statistic from Figure 1-1 and a positive trend in scientific publications for P $\mu$ SL can be observed. Especially for the year 2021 there are more than double as much publications to the previous year 2020. Therefore, it can be stated that this additive manufacturing technique is, in the beginning, to become more popular.

Since P $\mu$ SL systems work with liquid photopolymers and build models layer-by-layer, the layer generation or recoating process can lead to a high degree of errors in parts fabrication. Therefore, one should investigate how defined and homogenous layers in P $\mu$ SL can be formed. One method to generate layers is the Deep Dip method, which is commonly employed in free surface P $\mu$ SL systems, where the liquid photopolymer has contact to air. In the Deep Dip method, the build platform with a previous cured structure is submerged deeply into the RV with the photopolymer and is emerged subsequently. Therefore, a new liquid photopolymer layer will be formed under gravity. A keyword search in Web of Science for "Deep Dip Recoating", "Deep Dip Layer Recoating" and "Deep Dip projection micro stereolithography" shows almost no publications or only publications regarding a different research field, manifesting that the Deep Dip recoating technique lacks experimental research. The Deep Dip technique is in its form one of the most straightforward recoating techniques depending only on a single axis movement and gravity to form new layers. Therefore, if a proper physical model describes this process, new stereolithography systems could quickly implement this

simplistic layer generation method. One significant paper about this topic was written by W. Tan et al. who investigated the layer preparation with the Deep Dip method via numerical simulations and discovered the dependency of viscosity and the RV to build platform ratio on the final layer height and layer settling time.

Additionally, the comprehensive goal of this work is to develop a printing system for the manufacturing of microscale actuators and optics and an example of a microactuator can be seen in Figure 1-2. Such components have a maximal size of a few cm or lower. Therefore, a printing resolution of the printing system should be targeted at about 1  $\mu\text{m}$ .

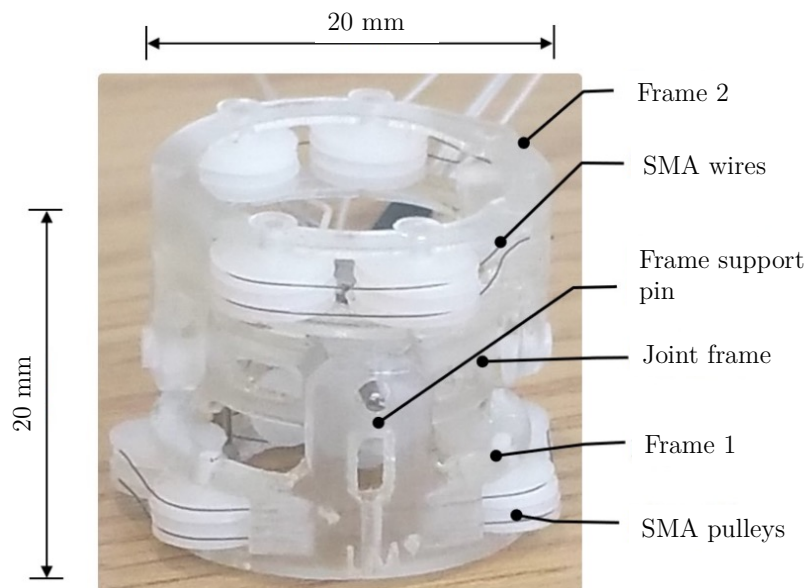


*Figure 1-2: A miniaturized actuator using wires made out of shape memory alloys (SMA) [2, p. 6].*

In previous works, mechanical and optical components of the printing system were successfully controlled via a developed software system. Furthermore, a foregoing study was conducted to quantify the resolution limit of the printing system for three different photopolymers which will act as a baseline regarding the print resolution and therefore a first printing system was built to cure fine structures for the resolution tests. Here the photopolymer PR48 from Autodesk showed the smallest possible printable feature size and as a result it will be used throughout this work. Regarding the layer recoating of the

printing system still no investigation was conducted. As a result, this thesis will primarily be based around the layer generation for the printing system with the Deep Dip method and W. Tans work will form the base of this thesis. Experiments were planned to investigate the layer preparation with this method and will be discussed in the following chapters.

## 1.2. State of the Art

AM becomes more and more important in the space of manufacturing as a report from Qi et al. states. Furthermore, the report states that the 3D printing industry will exceed \$21 billion by the early 2020s in market share [3, p. 1]. Especially in the realm of manufacturing tiny, customised objects, AM printing can help to reduce cost and one example here is the manufacturing of small micro-optics [4, p. 1]. Logically, a high printing resolution is needed for small optics. One established AM printing technique with a high resolution is P $\mu$ SL, which closes the gap between two-photon polymerization (TPP) and stereolithography (SLA) systems in terms of resolution and therefore is suitable for micro-optics fabrication [3, p. 1]. The first paper describing a projection micro stereolithography process was published by Zissi et al. in 1994 and from there, P $\mu$ SL has advanced as a reliable fabrication technique [1, p. 91].

Additionally, with high-resolution kinematics controlling the x and y-axis, stitching multiple masks together is possible and recently became an essential component in commercial systems called large area projection micro stereolithography (LAP $\mu$ SL). And noteworthy here is Boston Manufacturing [5] [3, p. 4]. Furthermore, with the introduction of the digital mirror device (DMD), digital mask creation became fast and reliable in P $\mu$ SL systems, allowing for constrained surface systems like continuous liquid interface production (CLIP), where uninterrupted and dynamic irradiation through an oxygen diffused photopolymer layer is used and build time is significantly reduced.

Coming back to micro-optics recent demonstrations showed, that functional lenses can be manufactured via AM. Chen et al. reported the fabrication of an aspherical lens of 5 mm height and a 7 nm surface roughness relying on grey scaling individual pixels with the DMD mask and post-processing techniques which can be seen in Figure 1-3. The printed lens had a resolution limit of up to 373.2 lp/mm [4, p. 4]. Additionally, Li Yu et al. demonstrated printing an array of microlenses with a diameter of 250  $\mu\text{m}$  and the Airy disks half-width for the 0th peak order was 10  $\mu\text{m}$  [6, p. 92]. Additionally, Figure 1-4 illustrates the ability of P $\mu$ SL to fabricate multiple small-scale objects simultaneously, increasing production output. All in all, it can be stated that P $\mu$ SL will become more important in the realm of printing micro-optics in the following years.

Next to printing micro-optics there are also other application for P $\mu$ SL, for example the combination of P $\mu$ SL with traditional silicon-based micromachining processes were explored. For instance the UV-LIGA process was combined with P $\mu$ SL in order to print 3D parts via P $\mu$ SL onto substrates manufactured with the traditional microfabrication method [1, p. 102].

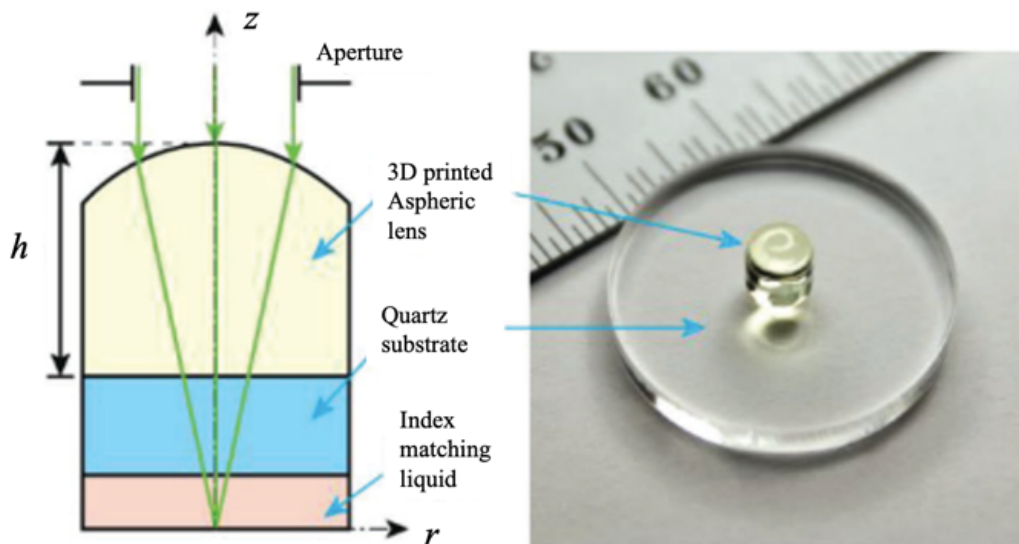


Figure 1-3: The 3D printed aspheric lens with a diameter of 5 mm on top of a quartz substrate

[4, p. 4].

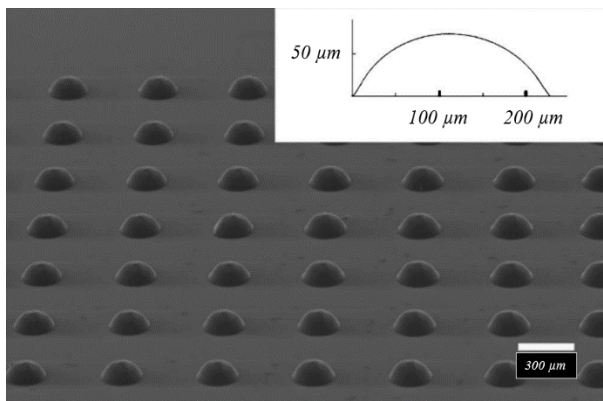


Figure 1-4: A micro-lens array printed with a  $P\mu SL$  system. All lenses here were manufactured parallel [6, p. 92].

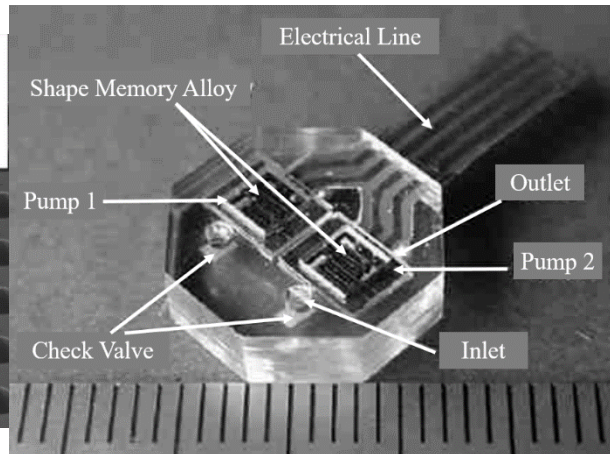


Figure 1-5: A micropump made with  $P\mu SL$  combined with traditional microsystem fabrication systems [1, p. 105].

An additional breakthrough in  $P\mu SL$  was achieved with the CLIP technology. Here the irradiation and lifting of the build platform are executed synchronously meaning the the liquid photopolymer is flowing beneath the cured structure and effectively reducing stair-step effects and increasing build speed. This is achieved by partially diffusing a liquid polymer layer with oxygen so that curing and solidification is inhibited at a first thin layer. [7, p. 24] [8, p. 21].

Apart from CLIP, almost all  $P\mu SL$  systems print layer-by-layer and it is important to note is that the generation of new layers strongly influences the printing quality, making layer preparation a needed research topic for  $P\mu SL$ . For this reason, multiple techniques were explored and summarized by Hafkamp et al. and will be explained in more detail in the subchapter 0. From the multitude of options in layer preparation, the Deep Dip method is the "simplest" technique. Here a new layer is produced by immersing a cured structure into a photopolymer vat deeply and emerging it subsequently. While waiting, a new fresh layer will form under gravity. Since the recoating process deals with liquid photopolymers, the physical process can only be accurately described with the Navier-

Stokes equation. Since the Navier-Stokes equation mostly leads to non-linear partial differential equations, analysis is not trivial. Unfortunately, not much research is known regarding the Deep Dip method. Noteworthy is W. Tan et al., who has done a purely numerical analysis of the Deep Dip method to find dependencies of some parameters [9]. His publication points out, that layer generation time depends mainly on the photopolymer viscosity and resin vat size, where decreasing the first and increasing the second will lead to a shorter recoating time. However, W. Tan. et al. also notes that those results are solely simulations and therefore need to be approved with experimental results. Furthermore, the publication's scope does not include an investigation of the material properties used in the simulation. For this reason, it is essential to investigate the Deep Dip method further, confirm simulation results as well as search for further dependencies in this recoating process.

### 1.3. Goals

Layer preparation for PμSL is as previously mentioned an important aspect and only a limited amount of scientific work can be found on this topic. This is especially true for the Deep Dip recoating method. This work will solely be based around the layer generation with the Deep Dip method in order to generate defined layers. Therefore, it will try to confirm the findings of W. Tan. et al. as well as search for additional dependencies on the layer height and layer curvature.

As a result, the first experiment is about a parameter analysis to confirm dependencies from W. Tans simulation and search for additional dependencies. Here great emphasis shall be placed on the influence on layer height and curvature.

After identifying important parameters to the layer height and curvature, an investigation of the layer height shall be done while the resin temperature is increased to decrease layer height and speed up settling time. This forms the basis of the second experiment.

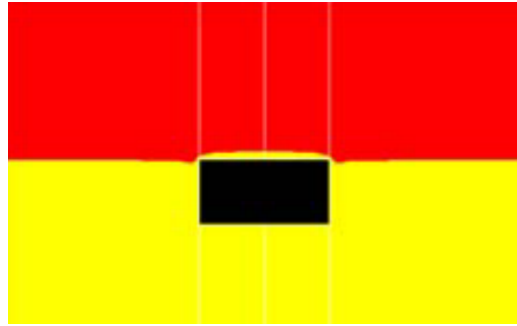


*Figure 1-6: The simulation scenario as described in W. Tan's numerical study. A curved layer can be seen on top of the build platform. The red area represents air and the yellow area environment the liquid [9].*

With the obtained knowledge from experiments 1 and 2, the first layers will be generated with found parameters and subsequently cured. Furthermore, the output of the new layer on top of cured layers shall be investigated. As a result, those three experiments formulate the goal of this work. An overview of the three experiments can be seen in Figure 1-7:

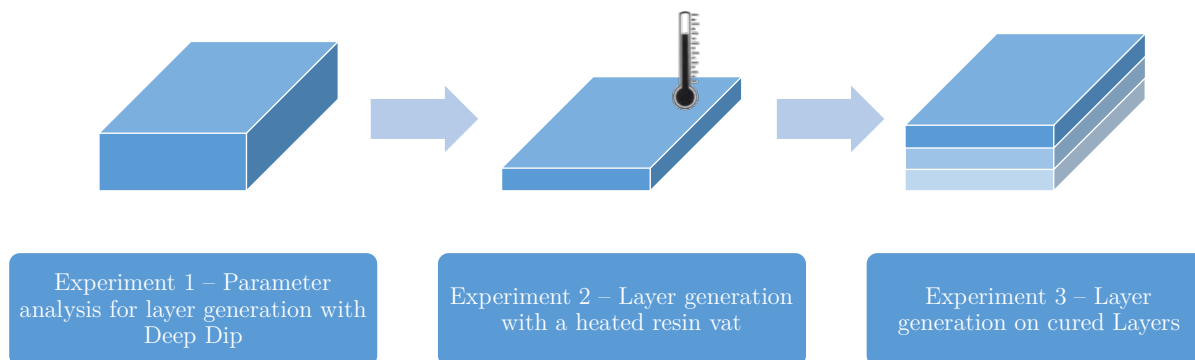


*Figure 1-7: The three planned consecutive experiments, formulating the goal for this work.*

## 2. Theoretical Background

This chapter will explain the basic concepts of AM in 2.1. Additionally, the AM technique of P $\mu$ SL is explained in more detail in 2.1.1 with its core technology DLP in 2.1.2. followed by the basics of layer generation in 2.2. regarding layer generation techniques in 2.2.1 and the Deep Dip method in 2.2.2. In 2.2.3 some layer measurement techniques are discussed as well as the confocal measurement principle in 2.2.4. Subchapter 2.3. will give a brief introduction into photopolymers with respect to photopolymerization process in 2.3.1, oxygen inhibition in 2.3.2, printing resolution in 2.3.3 and rheological properties in 2.3.4. With the knowledge in photopolymers subsequently the mathematical model of drop spreading will be derived and explained in 2.4. With this the fundamental knowledge is given to understand the experimental part of this work.

### 2.1. Additive Manufacturing

AM describes a set of manufacturing techniques where parts are created by merging multiple layers of a defined thickness together and as a result components with complicated geometries can be manufactured. This allows designers and engineers more freedom when designing new systems. However, AM has multiple drawbacks, which are slow manufacturing speed and lower parts quality compared to established manufacturing processes. Furthermore, when it comes to producing a high number of the same components most AM techniques cannot compete with traditional methods and therefore AM is mostly used in the rapid prototyping space [10].

Most AM methods generate parts in 2D rather than 3D since manufacturing is done mostly layer-by-layer in a x-y-plane. Because of this, stair step effects can be visible in z-direction of those parts, which can be reduced by lowering the layer height or using more advanced techniques such as CLIP [7, p. 21]. The minimal achievable layer height is different for each AM technique. In FDM for example a typical minimal layer thickness can be up to around 0.25 mm. In FDM plastic filaments are pulled into a printhead and

the printhead then melts and extrudes the plastic onto a build platform. The materials used in FDM include polycarbonate (PC), acrylonitrile butadiene styrene (ABS), polyphenylsulfone (PPSF), Polylactic acid (PLA) and multiple other thermoplastic materials [11, p. 4].

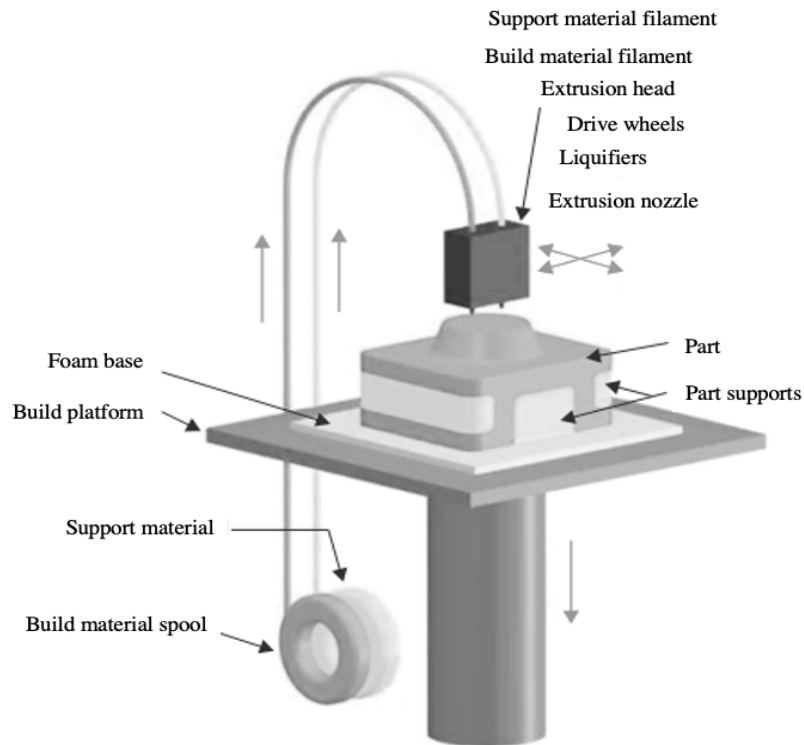


*Figure 2-1: Principle of the FDM technique. An extruder moves above a build platform, melting and extruding a thermoplastic on top of the previous layer. As support, dissolvable thermoplastics can be used and extruded through a second nozzle. The build material is stored in spools[12].*

Other techniques like Polyjet or Inkjet can achieve z-axis resolutions up to 16  $\mu\text{m}$  whereas the TPP technique can achieve micro to sub-micrometre resolution making it suitable for micro/nano fabrication. TPP uses a three-stage photochemical process called two photon absorption (TPA) which is the underlying mechanism of TPP [13]. The key elements of TPP manufactured parts are voxels which are placed next to each other, and the small size of the voxels help to achieve high dimensional accuracy in the sub micrometre regime. As a result, the accuracy of the printed structures depends on the voxels' size and spatial arrangement [13].

Regarding the resolution in AM, P $\mu$ SL closes the gap between Polyjet/Inkjet and TPP and can be used for microfabrication as well and it will be explained in more detail in the following section 2.1.1.

### 2.1.1. Projection Micro Stereolithography (P $\mu$ SL)

AM photopolymerization based printing techniques are feasible production methods in terms of microfabricating parts since they exhibit micrometre or even sub-micrometre resolutions [14]. The first technique using photopolymers as a build material was stereolithography (SLA) and is the predecessor of P $\mu$ SL which is now commonly used in the AM industry. In SLA, UV-light commonly from a laser is used to polymerise photosensitive materials selectively. The laser light is redirected by two galvanometers, so that individual points on the liquid photopolymer surface can be solidified. Additionally, components are made by successively tracing 2D cross-sections of the model step by step whereas in comparison P $\mu$ SL cures an entire layer at ones instead of tracing sections of a single layer like in SLA [15]. SLA is in terms of surface quality, dimensional accuracy and resolution close to P $\mu$ SL [16].

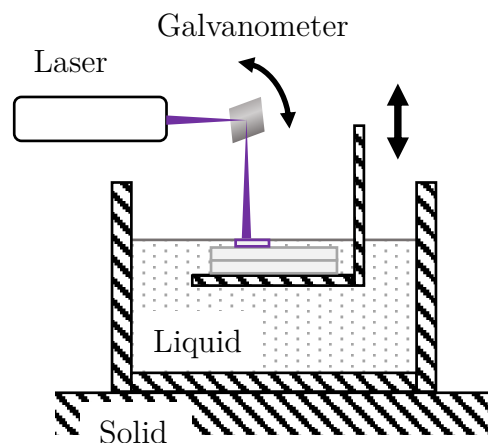


*Figure 2-2: The principle of an SLA system, where a UV-Laser source is deflected by 2 galvanometers. The galvanometers are mirrors, which will be rotated to reflect the laser beam into any 2D point into the liquid photopolymer surface. Additionally, scan lenses are usually employed to correct the length difference of the laser beam for different lateral positions.*

The first P $\mu$ SL system was proposed by Bertsch in 1997. In his proposal, a spatial light modulator (SLM) is used to generate a dynamic mask. Here depending on the type of SLM UV-light can pass through or is reflected from it and subsequently shaped like the cross-section of the part to manufacture. In order to achieve a high resolution, the cross-sectional image passes through a optical systems reducing the original feature size of the image. There are three commonly used types of SLM's, which are liquid crystal display (LCD), liquid crystal on silicon (LCoS) and digital mirror devices (DMD). A comparison between all 3 reveals, that the DMD has the highest efficiency and since the LCoS and LCD have worse light transmission, contrast and switching time compared to the DMD. [17]. Normally a light emitting diode (LED) especially a UV-LED is used in P $\mu$ SL as a light source. Compared to lasers which are used in SLA, LED's exhibit a wider spectral range but they are less expensive. Additionally, most P $\mu$ SL systems feature a build platform on which the actual printing is performed as it can be seen in Figure 2-3. Depending on the build topology, the UV-light comes from the top or bottom and is imaged via the optical system onto the build platform and subsequently a structure will be cured onto it.

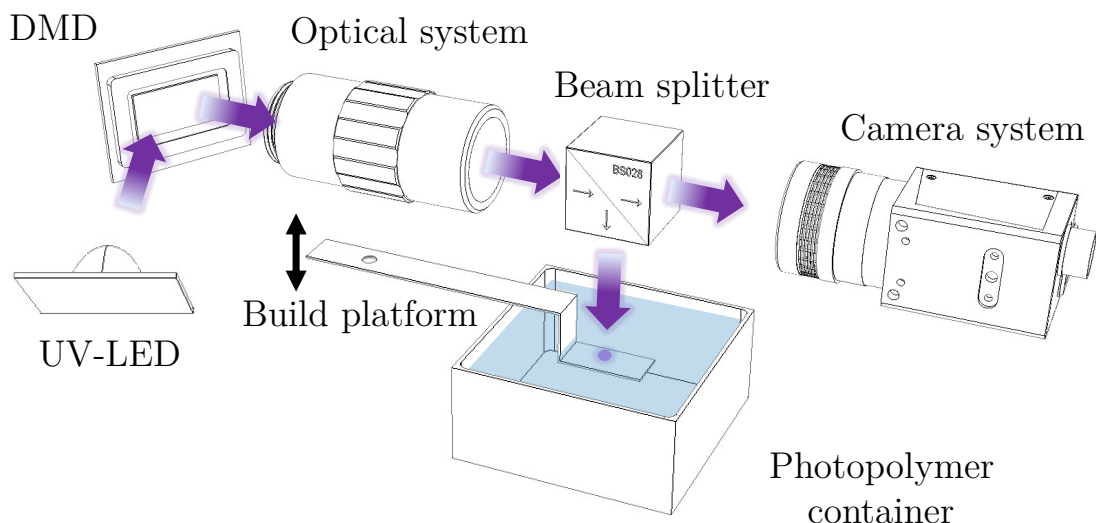
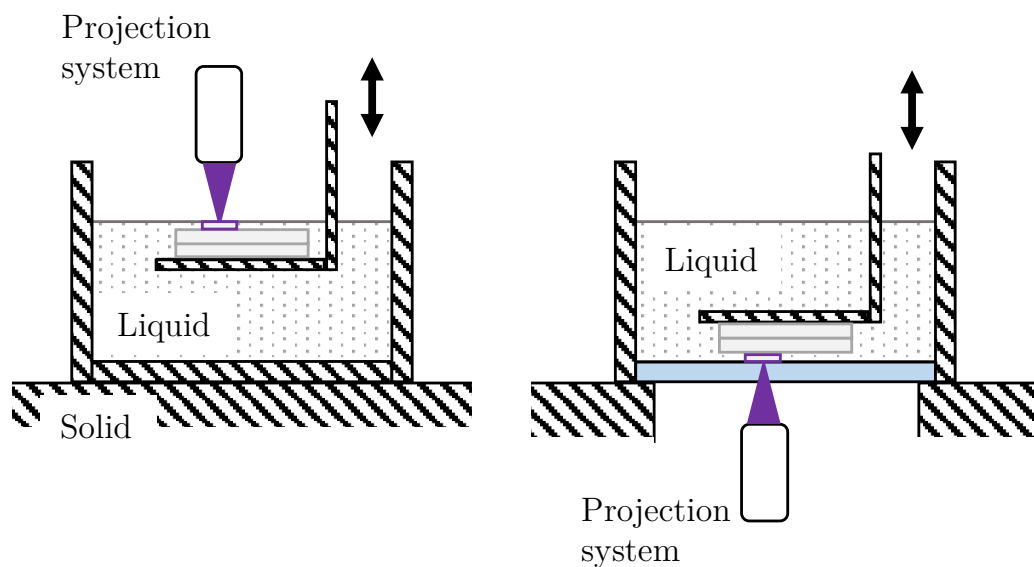


Figure 2-3: Components of a P $\mu$ SL system include a UV-LED, Digital Mirror Device (DMD), Optical System, Beam Splitter, Camera System, and Photopolymer.

The build platform is then moved to generate a fresh liquid layer of photopolymers and following a new structure is cured. This cycle is repeated over and over until the desired part is fully cured. As implied, there are basically 2 different build philosophies in P $\mu$ SL called top-down and bottom-up. In top-down printing, the object to be printed is put on top of the build platform and is moved downwards layer-by-layer into the resin vat during printing, which can be seen in the Figure 2-4 on the left-hand side. The maximum printing height of the system is restricted due to the resin vat and amount of photopolymer inside it. In bottom up printing the printed object hangs upside-down on the platform and has contact to a transparent window so that the light still can reach the photopolymer at the build platform, which can be seen in Figure 2-4 in the right-hand side. As the printing progresses, the build platform is moving upwards layer-by-layer. Here the main advantage is that the vat only requires a thin resin covering where in contrast to the top-down topology the resin vat must be filled much more.



*Figure 2-4: The two topologies are on the left-hand side, top-down, and the right-hand side, bottom-up. In top-down, the curing radiation comes from the top, and the platform is lowered into the resin for each layer. In the bottom-up, the curing radiation comes from the bottom through a window, and the platform is raised for each layer.*

One drawback for the bottom-up topology is that the object to print will have contact to the transparent window and the adhesion force must be overcome, which can lead to the damage of the part itself. However, this problem can be avoided by using anti-stick coatings on the window or using window materials such as PDMS [18, pp. 23-24]. Top-down printers have a significant benefit over bottom-up printers since they are easier to build because there is no adhesion to break between the resin vat and the object [18, p. 23]. The bottom-up method of printing can save time and money by reducing the quantity of resin used and creating items using high viscosity materials. Since the Deep Dip method will be investigated, the planned printing system will be constructed with top-down topology.

### 2.1.2. Digital Light Processing

Today most P $\mu$ SL systems use the digital light processing (DLP) technology to dynamically create masks for the curing process and therefore this technology will be explained here briefly. The DLP technology was introduced in 1996 by Texas Instruments and is widely used in AM for structured light purposes. In DLP a digital mirror device (DMD) is used. Those DMD devices are made up of millions of individual tiny mirrors.

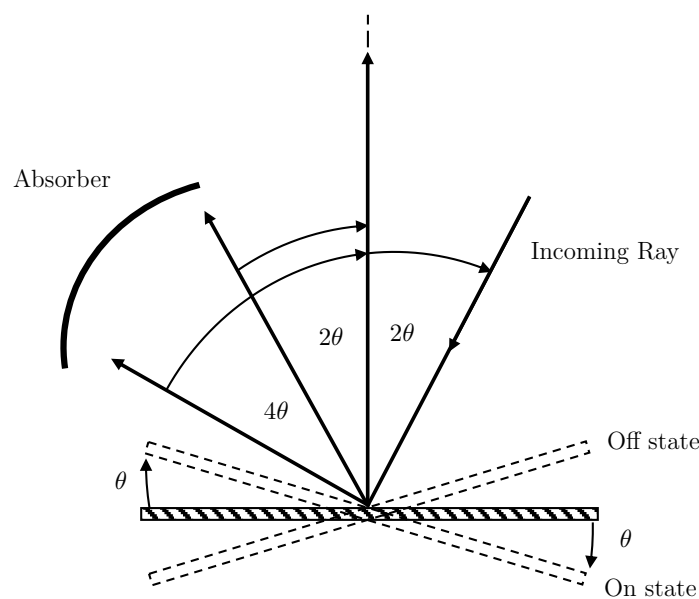


Figure 2-5: The working principle of a single DMD mirror element.

The individual mirrors are controlled via complementary metal-oxide-semiconductor (CMOS) circuits which are buried beneath the mirrors. The mirrors can be switched between on and off states. Here an off state corresponds to a mirror tilt of mostly +12 degrees and an on state to -12 degrees relative to the surface normal [19, p. 1] [20, p. 14].

Figure 2-5 the working principle of a single mirror element is displayed. It shows that in the beginning the mirror is in a horizontal state and therefore the optical axis is vertical. The on state of the mirror is defined as  $-\theta$  relative to the horizontal position and the off state is defined as  $+\theta$ . If an incoming ray hits a DMD mirror element in its on state ( $-\theta$ ), with an angle of  $2\theta$  relative to the optical axis, the reflected ray will have an angle of zero to the normal. Otherwise, if the mirror is in its off state ( $+\theta$ ) then the ray will be reflected to an angle of  $4\theta$  relative to the surface normal and will hit an absorber. Additionally, if the mirror is in its initial state, then an incoming ray with  $2\theta$  will be reflected at  $2\theta$  and will hit the absorber too. The individual components of a DMD can be seen in Figure 2-6. The mirror elements are mounted onto a yoke. The yoke is mounted on a hinge which creates a tilting motion. The landing tip stops the tilting motion resulting in a fixed angle.

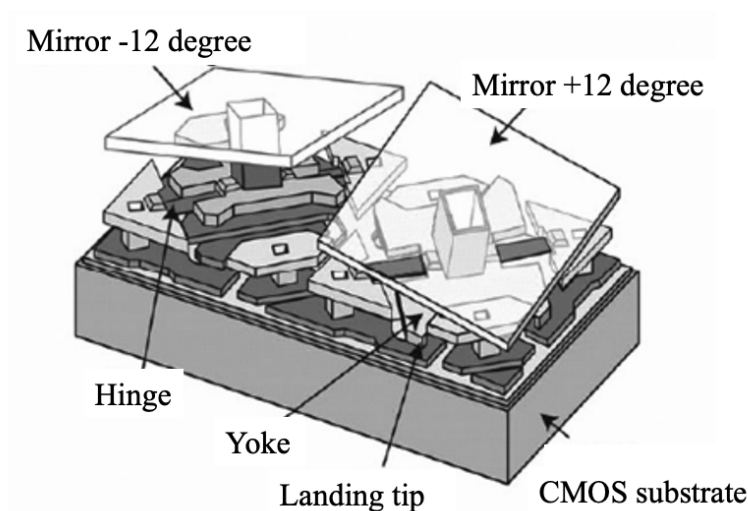


Figure 2-6: Two DMD mirror units are shown in more detail, sitting on top of the CMOS substrate [19].

The DMD is both an optical microelectromechanical system (MEMS) and a spatial light modulator (SLM) due to its highly reflective mirrors used to control light [20, pp. 14-15]. Another notable benefit of DLP is the relative rapidity with which each mirror may flip between on and off states [19, pp. 447-448]. Furthermore, a DMD is deployed in the used projection system for the experiment 3. Even though UV-light is reflected in the off state to an absorber, some light can still pass to the projection optics and therefore unwanted background illumination can be created. This can result in a problem where patterns must be cured with a precise energy dose. Since only a full layer must be cured in experiment 3, background radiation from the projection system can be ignored.

## 2.2. Layer Generation

The recoating technique directly impacts the layer height and therefore z-axis resolution [9, p. 53]. Most recoating methods cannot create a perfect homogenous resin layer and surface. As a result, compensation techniques must be employed. Layer non-uniformity compensation requires the availability of a 2D height map measurement at high spatial resolution, which is not easy, as proven by the few sensing methods utilised in the literature. Therefore, it is important to discuss the generation methods for new layers as well as layer measurement methods.

### 2.2.1. Layer Generation Methods

There exist many layer generation techniques for different applications, but this section will focus on recoating techniques commonly used in stereolithographic systems. Those recoating procedures can be grouped in the self-metered (also called free surface) systems and constrained surface systems. For example in self-metered systems mostly only a coating applicator largely determines the final layer thickness and a liquid-to gas contact (mostly air) is present, whereas in constrained surface systems the liquid has no contact

to an gas but rather to a surface of a transparent material [21, p. 691]. Constrained surface systems will be neglected and not be described in this section since they don't play an important role in this work, but a brief introduction will be given to some free surface techniques and the deep dip method too. Some of the layer recoating methods can be seen in Figure 2-7.

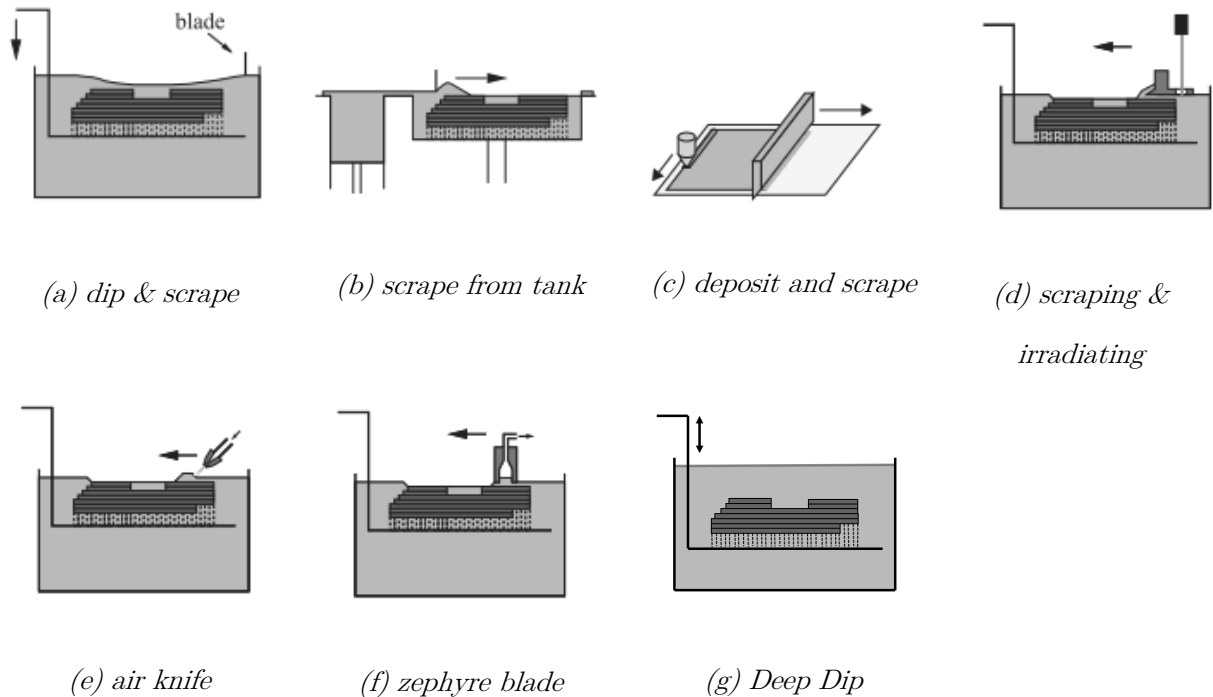


Figure 2-7: Showing different self-metered, free surface recoating systems and their working principles [21].

One example is (a) the dip and scrape technique. Here the build platform is moving downwards into the resin vat to apply a new fresh liquid layer to the cured structure on top. After driving up again, a doctor-blade scrapes the uneven liquid surface to obtain a flat homogeneous layer. In the scrape from tank technique which can be seen in (b), new liquid is applied with an external tank. Here the liquid is pushed out of the external tank and an doctor-blade applies the liquid onto the cured structure. For the deposit and scrape method in (c) a syringe can be used to apply a single line of photopolymer. Again, a doctor-blade is used to scrape down the photopolymer liquid. As it can be seen in (d) it is also possible to scrape and level the liquid layer while irradiating the flattened layer

in the same time, reducing processing time. In (e) an air knife is used to flattening a liquid layer after the cured structure was dipped into the resin vat. With (f) a hollow blade is used which pumps unnecessary liquid away after dipping the part into the resin vat. [21, p. 692]

In (g) the Deep Dip method can be seen. Here the layer generation just depends on the dipping of the build platform and cured structure into the photopolymer. It can be observed that the Deep Dip method is the only one method that does not need additional components besides a stage for driving up and down the build platform.

*Table 2-1: Comparing different recoating methods.*

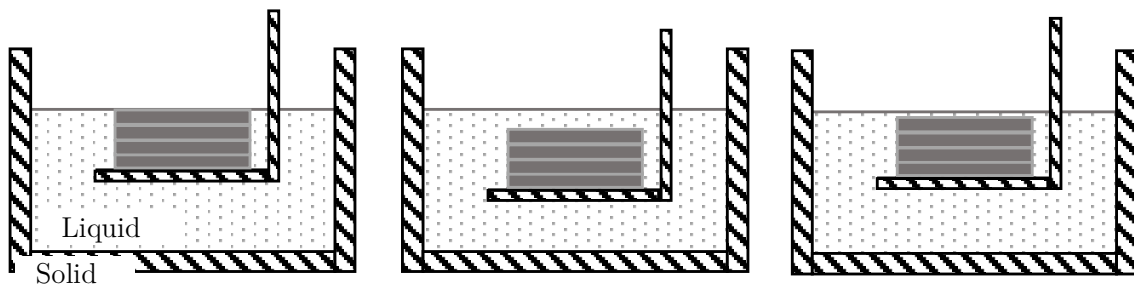
<b>Recoating Method</b>	<b>Resin metering</b>	<b>Contact</b>	<b>Min Layer Thickness in [<math>\mu\text{m}</math>]</b>
Deep Dip	self-metered	contactless	10 (W. Tan et al.)
Dip & Scrape Recoating	self-metered	contact	150
Scrape from Tank	self-metered	contact	25
Simultaneously scraping & irradiating	self-metered	contact	50
Deposit & Scrape recoating	self-metered	contact	10
Air Knife Recoating	self-metered	contactless	5

Additionally, from Table 2-1 it can be observed that the lowest layer thickness can be achieved with the air knife recoating technique with up to 5  $\mu\text{m}$  layer thickness. Furthermore, the air knife recoating is a contactless method, and as a result, no care must be taken regarding accidental destruction of the printed objects. Additionally, it can be seen that the Deep Dip method, which is also contactless, cannot achieve that much of a low layer thickness, but it comes close with around 10  $\mu\text{m}$ . No data on the layer thickness for the Deep Dip method is given from Hafkamp. Here only W. Tan et al. delivers values from numerical simulations. Since the Deep Dip method can achieve

low layer thickness without additional actuators, generating a new layer is a less complex with this method. The Deep Dip will be discussed in the following section 2.2.2.

### 2.2.2. Deep Dip Method

As seen in 2.2.1 the Deep Dip method can potentially generate thin layers and the method can simply be described as the following: After one layer of photopolymer is polymerised and in a solid state, the z-stage drops downwards, and the solidified object is immersed deeply into the resin vat and photopolymer, ensuring that the already solid layer's surface is entirely coated by the liquid. Afterwards, the z-stage climbs higher, bringing the cured object's upper surface closer to the resin's surface. From Figure 2-8 the height difference between the surface of the cured structure and the liquid surface defines the new layer height. When the component reaches this point, the resin near the next layer is still moving and the system must wait for the liquids surface to settle under gravity before curing the new layer. This process can be seen in the following illustration with all three stages of the process:



(a) *The initial state.*

(b) *Immersing deeply.*

(c) *Lifting to surface.*

*Figure 2-8: The states of the Deep Dip procedure generate new layers on top of a freshly cured structure inside of a photopolymer reservoir. The movement is created by attaching the build platform to a stage.*

It should be mentioned that the final position of the build platform can be varied, meaning its final position can be above or below the initial height of the liquid surface.

This can lead to different layer heights and settling times of the liquid layers and the principle can be seen in Figure 2-9.

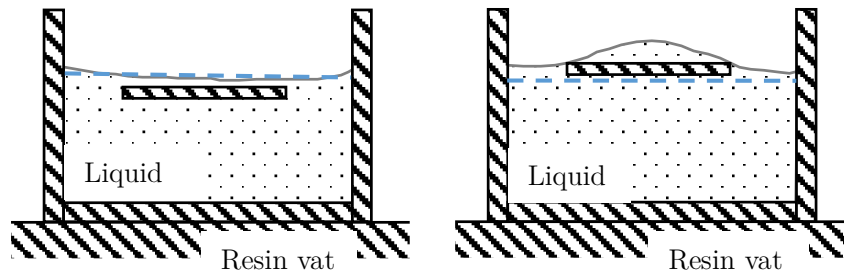


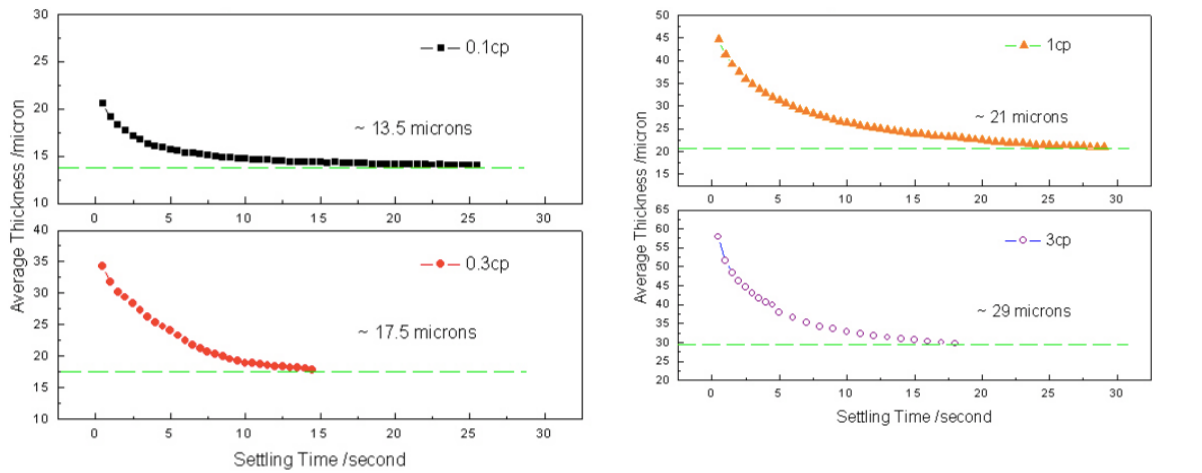
*Figure 2-9: The build platform's final position can be either above (left-hand-side) or below (right-hand-side) to the initial liquid surface height (blue dashed line) leading to different flow behaviour of the liquid.*

Since the layer generation relies on the liquid to settle down by itself under gravity, this method must spend a significant amount of time to form new layers and is highly influenced by the viscosity of the used material. To reduce the viscosity of some photopolymers nonreactive additives or solvents are sometimes mixed in [8, p. 18].

Not much research is known about the Deep Dip method in the recoating process, even though it is commonly used in PµSL. W. Tan et al. investigated the Deep Dip method with a numerical simulation approach to find correlations between final layer thickness, settling time, resin viscosity, and build platform to resin vat ratio [9, p. 50].

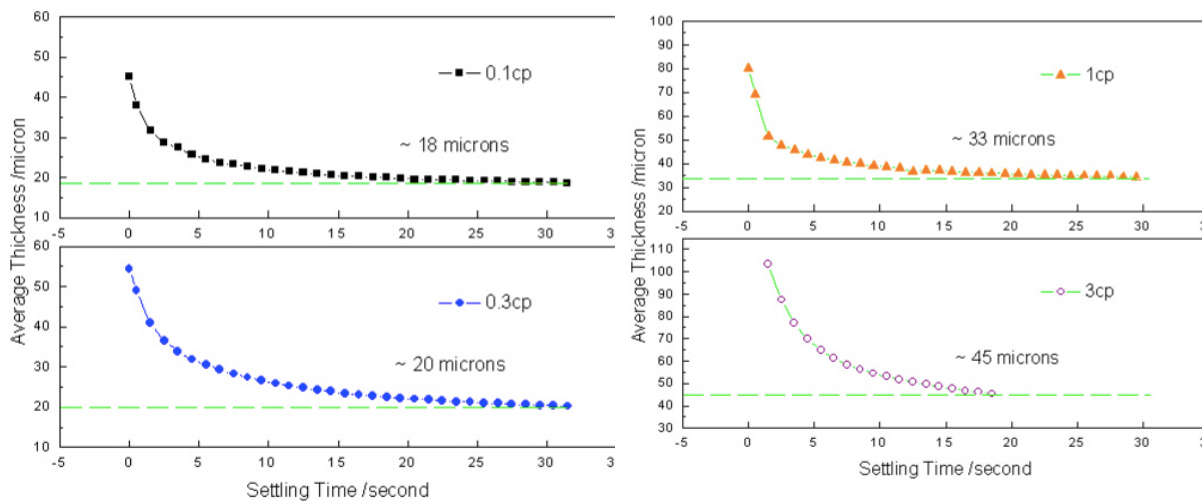
The simulations were conducted with the Ansys Fluent software and there the Navier-Stokes equation was solved numerically with the volume of fraction method (VOF), which is suited for free surface fluid flow. Additionally, a user defined function was implemented to control the movement of the build platform. Measurements of the average layer thickness and settling time were only conducted after the build platform movement was finished. It should be mentioned that the final build platform position always matches the initial liquid surface height. In the simulation four viscosities were

iterated and for each viscosity the 4 build platform to resin vat ratios where iterated [9]. The results of the four changed viscosities for a ratio of 0.0323 and 0.0645 can be seen in Figure 2-10. The actual values of the viscosity and BP to RV ratios can be seen in Table 2-2.



(a) Average layer height for 0.1 and 0.3 mPas with a BP to RV ratio of 0.0323

(b) Average layer height for 1 and 3 mPas with a BP to RV ratio of 0.0323



(c) Average layer height for 0.1 and 0.3 mPas with a BP to RV ratio of 0.0645

(d) Average layer height for 1 and 3 mPas with a BP to RV ratio of 0.0645

Figure 2-10: The obtained results from the simulation with four different viscosities each for two BP to RV ratios. The average layer height is plotted over time for a maximum settling time of 30s.

From Figure 2-10 it can be observed that an increase in viscosity results in an increase in average layer thickness. Here the average layer thickness increases from around 13.5  $\mu\text{m}$  to 29  $\mu\text{m}$  for the lowest to the highest viscosity. When comparing the figures

(a) and (b) to (c) and (d) one can observe an overall increase in the final average layer thickness where the BP to RV ratio was increased. Therefore, it can be stated that with an higher BP to RV ratio the average layer thickness will be increased.

Table 2-2: The changed parameters of the numerical simulation.

Viscosity in [mPa s]	0.1	0.3	1	3
RV to BP Ratio in [a.u.]	0.0161	0.0323	0.0645	0.129

The relationship of the viscosity onto the final average layer height for two different BP to RV ratios can be seen here in Figure 2-11. Here the dependency of the viscosity on the final average layer height seems to be logarithmic.

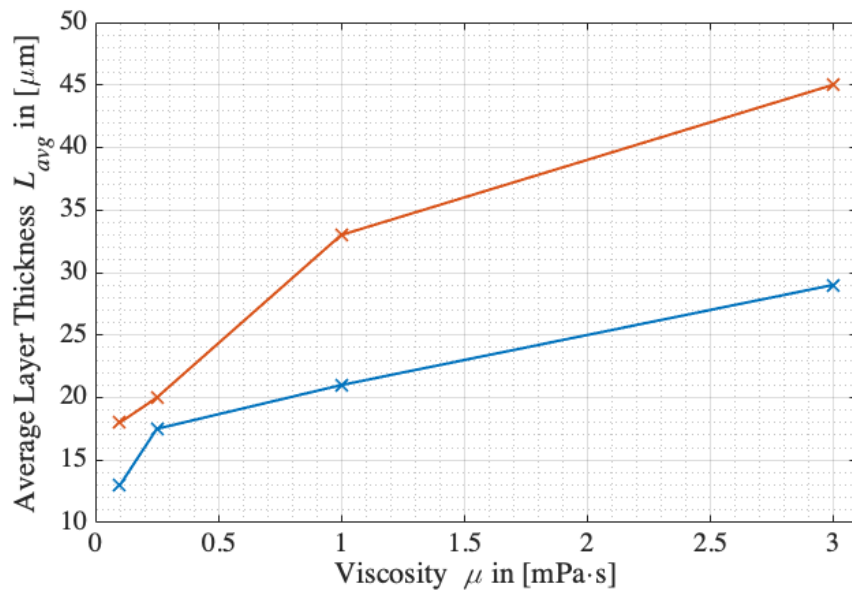


Figure 2-11: Dependency of the numerical obtained average layer thickness on the liquid viscosity [9].

Whereas the relationship between the BP to RV ratio to the final average layer thickness can be described as linear as it can be observed in figure 2-12.

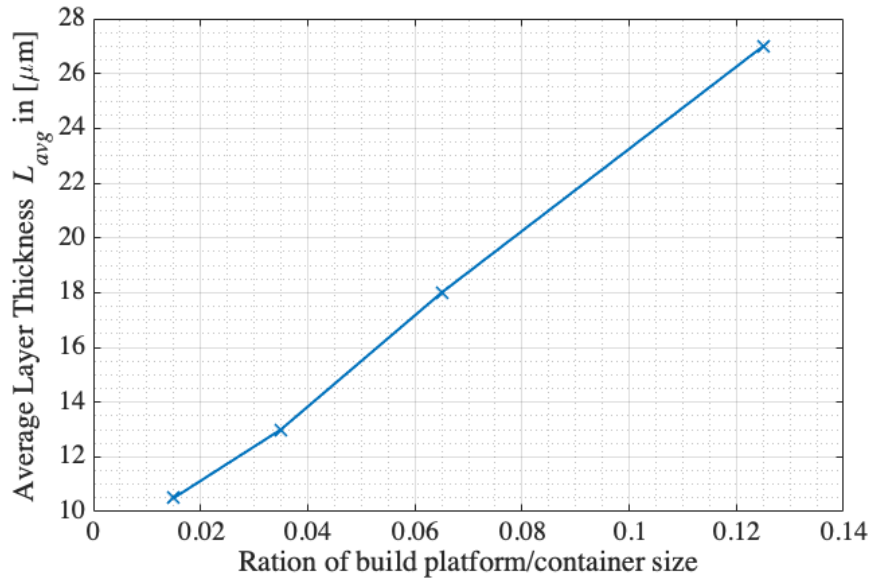


Figure 2-12: Dependency of the numerical average layer thickness from the ratio between the build platform and resin vat sizes for a viscosity of 0.1 mPas [9].

Regarding the settling time, the simulations also show a logarithmic dependency on the layer height, for a change in BP to RV ratio, which can be seen in the figure 2-13:

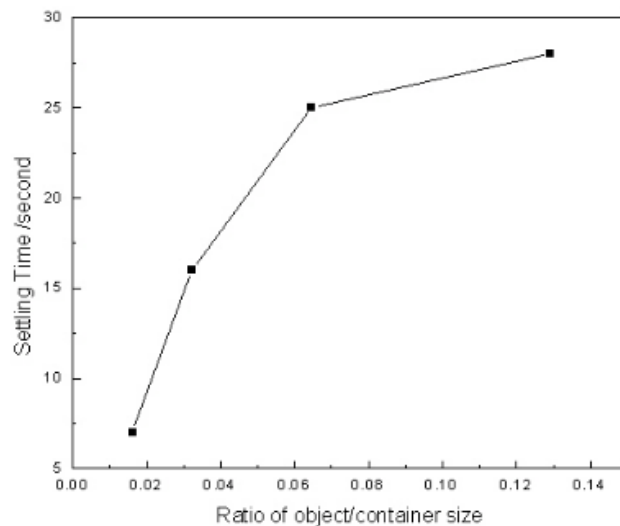


Figure 2-13: Dependency of the settling time from the ratio between the build platform and resin vat sizes for a viscosity of 0.1 mPas [9].

All in all, it can be stated that W. Tan's simulations showed a logarithmic dependency of the average layer thickness on the viscosity as well as linear dependency of the average layer height from the BP to RV ratio. Furthermore, it can be seen, that the viscosity of the resin determines the layer thickness, and thinner layer thicknesses can be attained via gravity levelling with lower viscosities.

W. Tan et al. suggests from his results, that resin viscosity should be close or below 0.1 mPas to create a layer thickness of less than 10  $\mu\text{m}$ . Therefore, in P $\mu$ SL different approaches should be utilised to minimise the higher viscosities of current resins and larger resin vats are suggested for thinner layers. [9, pp. 56-57]. Since a simulation only obtained those dependencies, there is a need to prove those with experimental results.

### 2.2.3. Layer Measurement Methods

Recoating is one of the most important subjects to P $\mu$ SL since the recoating techniques have a direct influence on the part quality and because of this reason techniques should be developed to monitor the recoating process in P $\mu$ SL. For example, Park et al. created a sensor system for assessing the surface of stereolithography products throughout the manufacturing process. The measurement approach of their sensor system is comparable to laser scanning confocal microscopy [21, pp. 697-698]. Furthermore, Narahara et al proposed a system to measure the flatness of a freeform liquid surface. The measurement was implemented by generating a grating image of entire reflection off a freeform surface. [23, p. 1] [21, p. 698].

To measure transparent layer of liquid photopolymers only non-destructive measurements techniques must be used so that the liquid film is not disturbed. Therefore, optical non-contact measurement methods are a good choice. In the past different optical measurements like ellipsometry reflectometry, confocal systems and interferometry were used successfully to measure the thickness of transparent films. Besides that, an increasing interest in the confocal systems is existing due to their durability in the face

of minor vibrations and harsh climatic conditions [24]. Furthermore, a chromatic confocal sensor system was available in the lab and therefore it was decided to use such a system for the upcoming experiments. As a result, the chromatic confocal sensor principle shall be describe in the following section 2.2.4.

#### 2.2.4. Chromatic Confocal Measurement Principle

The confocal principle works like the following: A light source mostly a laser is used. In front of the laser a lens system focuses the laser light onto the surface that has to be measured. The focused laser light is reflected from the surface back into the optical system. Between the optical system and the laser, as beam splitter is place, meaning the light reflected from the surface is redirected at 90 degrees and hits a detector. In front of the detector a pinhole is placed in such a way that only light reflected form the focal plane of the lens system hits the detector. Light reflected from another plane will not pass the pinhole and therefore not hit the detector [25]. To receive a height information, the sensor must be driven back or forth relative to the surface to increase and decrease the distance to the measuring target. If the focal plane matches the objects surface height, then the maximum intensity will be received at the sensor chip. The intensity can then be correlated to the driven distance to compute the surface height.

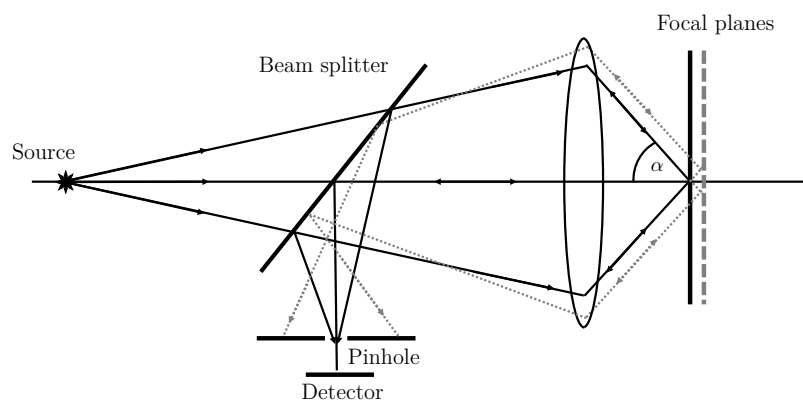


*Figure 2-14: The working principle of the confocal measurement principle. A light source is focused onto an object within the focal plane and is reflected from it. The light that is reflected precisely at the focal plane will not be blocked by the pinhole and reaches the detector [25].*

An expanded version of the confocal measurement principle is the chromatic confocal principle as the name implies. Today this technique is commonly used in order to measure surfaces in a precise manner [26, pp. 3259-3260]. The essential premise of confocal chromatic sensors is that a longitudinal chromatic aberration of the optical sensor system is wavelength dependent, meaning that now multiple foci can be used to measure a surface height.

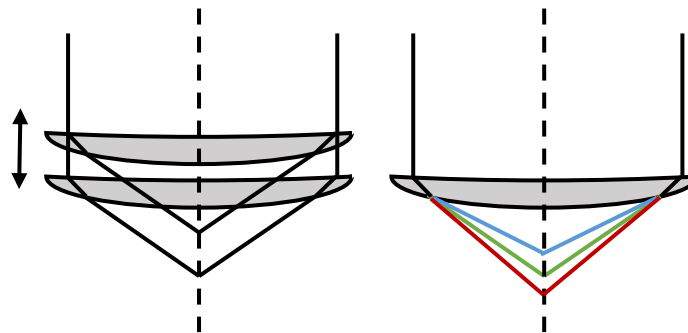


*Figure 2-15: Showing on the left how mechanical depth scanning can be achieved by moving the focus position up and down compared to the chromatic approach where the depth information is already encoded into the chromatic aberration from a lens.*

Like the confocal sensor, light from a polychromatic source is focused through a lens onto a surface. Polychromatic light sources can be halogen lamps, white light LED's or xenon lamps. The focussing optics exhibit chromatic aberration, meaning that different wavelengths from the polychromatic light source are focused at different points along the optical axis as it can be seen in Figure 2-15 on the right hand side. Furthermore, light with shorter wavelengths (e.g. blue light) can exhibit higher dispersion and are focused more near to the lens compared to light with a longer wavelength (e.g. red light). Depending on the surface topography only certain wavelengths are then reflected back through the pinhole. Behind the pinhole, a diffraction grating is placed which splits up the incoming polychromatic light into its spectral components and thus those spectral components hit then the detector [26, p. 3260]. Therefore, depending on the surface

topography only certain wavelengths are detected on the sensor at different positions which can be seen in Figure 2-16.

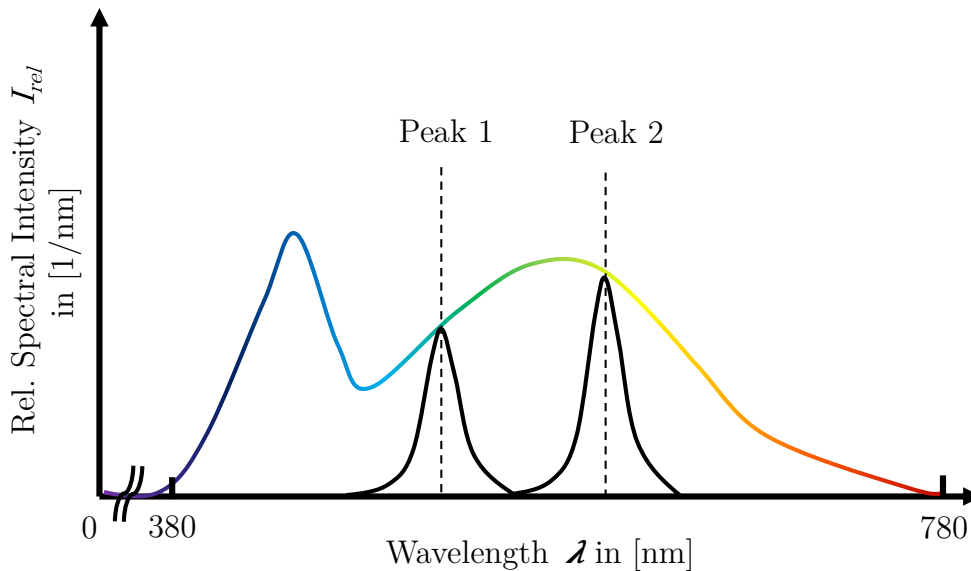


*Figure 2-16: Showing the full spectrum of a typical white light led, which can be used in a chromatic confocal sensor. The spectrum here can range from 380 nm to 780 nm. When a chromatic confocal sensor measures a single transparent layer, two peaks will appear on the spectrometer. Their intensity will be within the intensity range of the white light source. Since peak 1 appears at a shorter wavelength than peak 2, peak one must be closer to the sensor than peak 2. Applying this principle and compensating for the dispersion of the transparent layer, one can calculate the geometric thickness of the layer.*

The topography (height) of the studied surface may then be estimated using the known wavelength dependency of the optical system's longitudinal chromatic aberration. The validity of this technique is determined by the precision with which the intensity maxima corresponding to distinct wavelengths are determined [26, p. 3260]. When measuring transparent layers the refractive index difference between two measured layers must be high enough to receive two distinct reflections, The precision of measurements produced with these sensors can be influenced by the measured object's dispersion [26, p. 3264].

Throughout this work, the chromatic confocal sensor IFS2405-1 from Micro Epsilon was used to measure the layer position and thickness. This sensor features a measurement range of 1 mm, working distance of 10 mm, a spot diameter 8  $\mu\text{m}$  and a resolution of 28 nm. The IFC2461-1 (the control unit) can measure transparent films with a layer thickness up to 50  $\mu\text{m}$ . A maximum sampling frequency can be set up at 25 kHz, which can be seen in the appendix at page 160. The optical head of used is the IFS2405-1, which can be seen in 161. The sensor can be controlled programmatically via an Ethernet or RS422 connection.



Figure 2-17: IFC2461 control unit (right-hand-side) and IFS2405 optical head (left-hand-side).

## 2.3. Photopolymers

AM enables the rapid manufacturing of optical components. At the centre of the manufacturing process are photopolymers. Photopolymers consists of monomers/oligomers and binders that polymerise when they are irradiated by UV-light [27]. Here the monomers and binders have an strong impact on the physical and optical properties of the photopolymer [28]. To print optical components successfully the behaviour of the photopolymers must be understood during the printing process. Therefore, in 2.3.1. photopolymerisation will be described briefly as well as oxygen inhibition in section 2.3.2. resolution in photopolymers will be discussed in 2.3.3. and more importunately the rheological properties of photopolymer will be discussed in 2.3.4.

### 2.3.1. Photopolymerisation

In the third experiment, first layers shall be cured and therefore the process of photopolymerisation will be explained briefly. Polymerisation is a chain reaction that results in polymers from a mixture of monomer which means that the materials transform from a liquid state into a solid state. Depending on the type of reactive particles in the photopolymer different kinds of polymerization reaction can happen. They can be differentiated between radical, cationic, and anionic polymerisation [7].It should be stated, that in the conducted experiments only photopolymers were used, which underly a radical polymerisation. In the radical polymerisation process, monomers are linked together to form polymers and a free radical is used as a catalyst. This catalyst is produced from an photochemical reaction which happens when the photopolymer mixture including a photoinitiator is irradiated with UV-light. [29, p. 5]. The UV-curing process is restricted to areas which are illuminated and as a result objects can be cured in a structured manner according to the illumination pattern. Additionally, UV-blocker are incorporated into the photopolymer restricting the curing of UV-light supplementally.

To fundamentally understand the photopolymerisation process, one must also describe the working curve formulated by Jacobs et al. This equation was derived from the Beer-Lambert law of absorption, combined with the radiation profile of a gaussian laser beam, but is also applicable to DLP systems. With his equation, the relationship between curing depth and exposure dose is described and therefore the required energy for curing in a certain depth can be chosen [30]:

$$C_d = D_p \cdot \ln\left(\frac{E_{max}}{E_C}\right) \quad (2-1)$$

Here  $C_d$  is the curing depth in [m].  $D_p$  is the penetration Depth in [m] at the used wavelength and acts as the slope of the working curve.  $E_{max}$  is the energy dose used in  $[\frac{mJ}{cm^2}]$ . The natural logarithm of 1 is equal to zero and as a result, the curing depth is 0, when the used exposure  $E_{max}$  is equal to the critical energy  $E_C$  in  $[\frac{mJ}{cm^2}]$ .  $D_p$  and  $E_C$  are purely resin parameters and must be measured independently for each resin [30].

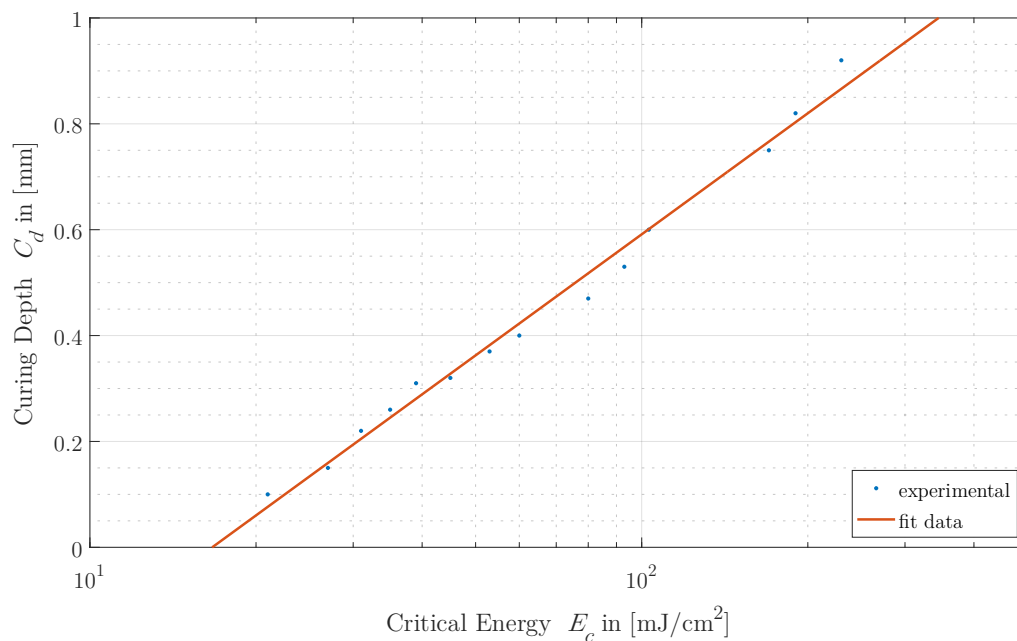


Figure 2-18: The working curve for the resin HS6603, showing  $C_d$  in relationship to the critical energy dose [18, p. 21].

An example for the logarithmic relationship can be seen in Figure 2-18 where the working curve of the HS6603 photopolymer is displayed, showing the Curing Depth in  $C_d$  dependent on the Critical energy  $E_c$ .

When structures are cured then the effect of shrinkage can be observed. This means that the structure size gets scaled smaller when curing and is not optimal in a printing process. The amount of shrink depends on the materials used for the photopolymer and the temperature. This stands especially in contrast to the experiment 2 and 3 where the photopolymer will be heated and cured. For example, Acrylics like PR48 can shrink from 5 % to 10 % [18, p. 21]. Although, shrinkage of a cured structure can be ignored for experiment 1 and 2 in this work since they will focus primarily on the generation of liquid layers. Here only experiment 3 may be affected. Another factor influencing the curing of photopolymers is the oxygen inhibition and shall be discussed in the following section 2.3.2.

### 2.3.2. Oxygen Inhibition

In oxygen inhibition, molecular oxygen inhibits the free radicals which are the catalyst for the polymerisation reaction and as a result, the polymerisation is inhibited too. Different methods were developed to mitigate the oxygen inhibition. For example the irradiation intensity can be increased strongly, which subsequently increases the free radical production [31, p. 177]. Additionally, certain additives can be mixed into the photopolymer to mitigate the effects of oxygen inhibition. Another approach is to polymerise the components in an inert environment, which suppresses the oxygen diffusion. Here nitrogen can be used to cover a liquid photopolymer so that no oxygen is present. Another gas commonly used is CO<sub>2</sub>, which can have the same effect as nitrogen. CO<sub>2</sub> as an inert gas has the advantage, that it is heavier than air and therefore liquid photopolymers can be covered more easily with it [31, p. 177][32, pp. 92-93]. When oxygen inhibition is present, the diffusion of oxygen can be up to 50  $\mu\text{m}$  in an photopolymer

layer however, the lower part of the film may be unaffected [31, p. 178]. Nonetheless, oxygen inhibition can be ignored for experiment 1 to 2 and may be only important when curing layers in experiment 3.

### 2.3.3. Printing Resolution

Since only the third experiment will deal with the curing of liquid layers and the resolution may not play an important role, this topic is not as important as the previous ones. Nonetheless, the resolution and scattering mechanism shall be explained briefly. The accuracy and resolution when printing is depended on different parameters. Most notably here is the photopolymer itself where the self-induced scattering limits the minimal printable structure size. In a polymer mixture Rayleigh scattering exists and comes mostly from medium size particles. Additionally, crystallites in the photopolymer can induce Mie scattering and increasing the overall scattering effect. Furthermore, when photopolymers are cured, then opacification can occur resulting in illumination in unwanted areas, decreasing the achievable resolution [33, pp. 10-11]. Additionally, it should be stated, that the resolution in z-direction when printing is also determined by the layer thickness formed, and therefore a lower layer height results in a higher resolution in z-direction.

### 2.3.4. Rheological Properties

The purpose of rheology is to determine the fluid flow that would be produced because of applied forces. Fluids continually distort when a force is applied, but on the other hand solids have an elastic response and do not deform continuously like fluids [33, p. 1].

To produce a fluid flow, the internal resistance to flow must be overcome. Fluid flow is depended different variables like velocity, pressure and stresses. Additionally those variables are a function of space and time [33, p. 1].

The resistance to flow can be described by the law of viscosity, which states that applied stress to a fluid is proportional to its deformation. This law was formulated by Newton and therefore fluids are either called Newtonian or Non-Newtonian fluids. [33, p. 5]. An important property which is included in Newtonian fluids is that the viscosity is not affected by shear stress [34, pp. 10-11, 35]. In this work the used fluids will be treated as incompressible Newtonian fluids, which reduces the complexity, when describing fluid motion. One metric for describing the relationship between the viscous resistance to flow and accelerated fluid is called the Reynolds number and is in itself the ratio of the fluid inertia to the viscous property [34].

$$Re = \frac{u \cdot L}{\nu} = \frac{\rho \cdot u \cdot L}{\mu} \quad (2-2-1)$$

Where:  $\rho$  is the density of the fluid in  $[\text{kg}/\text{m}^3]$ ,  $u$  is the flow speed in  $[\text{m}/\text{s}]$ ,  $L$  is a characteristic linear dimension in  $[\text{m}]$ ,  $\mu$  is the dynamic viscosity  $[\text{kg}/(\text{m} \cdot \text{s})]$ ,  $\nu$  is the kinematic viscosity  $[\text{m}^2/\text{s}]$  [33, p. 7]. If the Reynolds number is high then, fluid flow may be described as turbulent, and vortices can be formed influencing the fluid flow. On the other hand, when the Reynolds number is low, the fluid flow tends not to form vortices and the flow is laminar, and the fluids viscosity dominates [33, p. 7].



*Figure 2-19: The Schlieren imaging technique shows the airflow generated by the heat of a candle and the transition from laminar to turbulent airflow [35].*

For free-surface recoating techniques the fluid flow can mostly be described as laminar. Laminar fluid flow tends to be less complex than non-laminar fluid flow and therefore this work will assume laminar flow. An example for the transition of laminar to turbulent fluid flow can be seen in the following Figure 2-19. In this figure, the flame of a candle heats up air. As a result, the air rises in a laminar way. Due to an increase in velocity (the Reynolds number increases) and other influences (e.g., disturbance in the air), the laminar flow changes over to an turbulent flow producing vortices.

As described before, the fluid flow when laminar is highly determined by the fluid's viscosity. Therefore, the concept of viscosity shall be explained briefly. As described earlier if a liquid flows into any direction there will be friction in the fluid which will impede the fluid flow which comes from the viscosity and is known as a coefficient of proportionality [33, p. 8]. When a fluid is flowing between 2 plates with infinite length, and there is no turbulence, because the fluid's velocities are low enough (laminar flow), then the velocity of the liquid from the lower plate to the upper plate will have a gradient,  $\frac{\partial u}{\partial y}$  where  $u$  is the velocity and  $y$  is the height between the two plates. Therefore, there must be a shear stress on the fluid, and it can be calculated with the following formula [33, pp. 8-10]:

$$\tau = \mu \frac{\partial u}{\partial y} \quad (2-2)$$

Where  $\tau$  is the viscous shear stress in  $[\frac{N}{m^2}]$ ,  $\mu$  is the dynamic viscosity in  $[Pa \cdot s]$  [33, p. 8]. Since the stresses in a fluid are applied to the fluid particles and depend on their velocity,  $\tau$  is a tensor dependent on the fluid particles spatial velocity gradient and therefore can be expressed with nine spatial components [36, p. 1].

The viscosity of a liquid is influenced by its temperature. The reason for this is that viscosity arises when a liquid flows and the liquid layers are sliding past each other. This sliding process happens much easier when the molecules are in an increased state of

motion and it happens when the temperature of the liquid is increased. This mechanism can be described by the Arrhenius relationship [33, p. 10].

$$\mu = A \cdot e^{(B/T)} \quad (2-3)$$

In this formula,  $\mu$  is the viscosity as described earlier.  $A$  and  $B$  are constants of the liquid and must be determined experimentally. The constant  $B$  can be determined by plotting  $d\mu/dT$  against  $\mu$  logarithmically. The temperature dependence will be important in experiment 2 and 3 where the viscosity will be lowered when the temperature is raised.

Furthermore, it can be stated that usually, the temperature dependency is more significant for liquids with a higher viscosity. Additionally, the viscosity of a liquid increases exponentially as pressure increases. If the pressure changes are only of a few bars, then this dependency is not very relevant [33, p. 10]. Therefore, it can be ignored in the conducted experiments if the changes are small.

## 2.4. Mathematical Model of Drop Spreading

To describe the Deep Dip procedure and the flow of a liquid accurately on a platform with contact to a liquid bulk it would be desirable to use a mathematical model. If a already existing mathematical model applies correct to the physical scenario then elaborate measurements to build a own model would be redundant. Unfortunately, no mathematical Deep Dip model exists in literature. To obtain a model that accurately describes the Deep Dip scenario, a model must be derived by solving a set of non-linear differential equations arising from the Navier-Stokes equations, which is not trivial. Another way is to use other models describing a physical scenario close to the Deep Dip method. One of these models is the of the drop spreading model of fluids on a horizontal surface, developed by Lopez et. al. and it will be later used in this work to describe the obtained measurements. Therefore, in this subchapter the mathematical model will be

explained, and the used derivation are mainly based on the paper from Lopez et al. His model focuses solely on the kinetics of drop spreading, where thermodynamic effects are mostly ignored. Therefore, his model is more accurate in the macroscopic regime. Furthermore, the model implies that the solid surface beneath the drop is already wetted, which implies a low contact angle with the surface as it can be seen in Figure 2-20 is certainly also the case for the Deep Dip method.

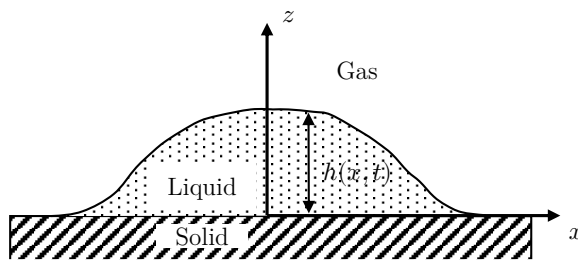


Figure 2-20: Showing the scenario described by Lopez. et al. were a drop in an initial wetted state and spreading across an infinite horizontal surface.

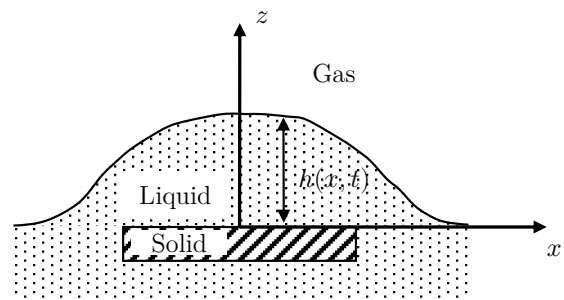


Figure 2-21: Showing the scenario for the Deep Dip method where a drop of liquid is created on top of a horizontal build platform but, the liquid on the top is still connected to the bulk liquid of the resin vat.

Additionally, the drop is mainly moved through gravitational force counteracted by the viscous resistance to flow. The model delivered is a solution to equations with boundary conditions matching the described scenario. The set of equations can be seen here [22, p. 461]:

$$0 = -\frac{\partial P}{\partial x} + \mu \frac{\partial^2 v_x}{\partial z^2} \quad (2-4)$$

$$0 = -\frac{\partial P}{\partial z} \quad (2-5)$$

$$P = p + \Phi_G + \Phi_M \quad (2-6)$$

The above-stated set of equations describes the fluid flow for a 2-dimensional case. Equation (2-4) is directly derived from the Navier-Stokes and later described in more detail. Equation (2-5) simply states that there is no energy density change  $\partial P$  over the change in the height  $\partial z$  and as a result  $P$  must be independent of  $z$ . The third equation states that the energy density  $P$  is a sum of different quantities, where  $\Phi_G$  is the local gravitational potential energy per unit volume and  $\Phi_M$  is the difference between potential energy density from the interactions between solid and liquid particles [22, p. 461]. Lopez et al. uses the following boundary conditions that the liquid flow velocity at the boundary layer with the solid and liquid is set to zero, and zero shear stress exists at the liquid's surface [22, p. 463].

To understand the equation (2-4), the Navier-Stokes equation must be discussed briefly. The general form of the Navier-Stokes equation can be seen here in equation (2-7):

$$\rho \frac{D\vec{v}}{Dt} = -\nabla p + \nabla \cdot T + \vec{f} \quad (2-7)$$

The left-hand side of the equation  $\rho \frac{D\vec{v}}{Dt}$  describes the force acting on each fluid particle and is also a material derivative [37]. The term  $\frac{D\vec{v}}{Dt}$  yields the acceleration and is multiplied with the density  $\rho$  which can be rewritten as the mass since, volume  $V$  times density  $\rho$  is equals the mass  $m$  and therefore the entire term describes a force  $F$  as it can be seen in equation (2-8).

$$F = m \cdot \vec{a} = V \cdot \rho \frac{D\vec{v}}{Dt} \rightarrow \rho \frac{D\vec{v}}{Dt} \quad (2-8)$$

The volume  $V$  can be ignored because since the Navier-Stokes equation describe a control volume with infinitesimal small fluid particles. The right-hand side of the equation (2-7) describes the sum of the acting force, where  $-\nabla p$  is a volumetric stress tensor and prevents the fluid from shrinking since the fluid presses against itself. The term  $\nabla T$  is the shear stress term, which causes motion due to horizontal friction and can be rewritten

to  $\mu \nabla^2 \vec{v}$ . The divergence  $\nabla$  is the sum of all partial spatial derivations of a vector and in a 3-dimensional case can be written as:

$$\operatorname{div} \vec{F} = \nabla \cdot \vec{F} = \left( \frac{\partial F_x}{\partial x} + \frac{\partial F_y}{\partial y} + \frac{\partial F_z}{\partial z} \right) \quad (2-9)$$

Moreover,  $\vec{f}$  is a force acting on each particle and is caused by gravity  $\rho \vec{g}$ . Each vector is 3-dimensional  $\vec{v} = (v_x, v_y, v_z)$  and as a result in the 2-dimensional case in an x-z-plane, the equation simplifies since y-direction can be ignored [37]. Adding the following boundary conditions simplifies the equation further:

$$v(x) = \text{const.}, \quad v(z) = \text{const.}$$

The boundary conditions just state that the fluid flow is constant. Consequently, the fluid acceleration must be zero  $\frac{D\vec{v}}{Dt} = 0$ , as the fluid velocity does not change over time. The divergence of the Navier-Stokes equation for the 2d case can be expanded explicitly in x and z-direction as it can be seen in equation (2-10) and equation (2-11) [38]:

$$x: 0 = - \left( \frac{\partial p}{\partial x} \right) + \mu \left( \frac{\partial^2 v_x}{\partial x^2} + \frac{\partial^2 v_x}{\partial z^2} \right) + \rho g_x \quad (2-10)$$

$$z: 0 = - \left( \frac{\partial p}{\partial z} \right) + \mu \left( \frac{\partial^2 v_z}{\partial x^2} + \frac{\partial^2 v_z}{\partial z^2} \right) + \rho g_z \quad (2-11)$$

Since a drop follows the movement in the x-direction, there is no interest in the equation in the z-direction. Also, the term  $\frac{\partial^2 v_x}{\partial z^2}$  is 0 since no velocity change in x direction depending on a change in z direction is existing. Furthermore, no gravitational force in x-direction exists and  $g_x$  becomes 0 and this leads back to equation (2-4). Additionally, the pressure  $p$  in (2-10) and (2-11) also can be expressed as  $P$ . To describe the flow of a liquid, Lopez et al. obtains the average fluid velocity by averaging the fluid velocity

depending on the film thickness. The average of a function  $f(x)$  can be found with the following formula, where  $a$  is the lower bound and  $b$  is the upper bound [39].

$$\bar{f} = \frac{1}{b-a} \int_a^b f(x) dx \quad (2-12)$$

Applying this to equation (2-4) after integrating twice over  $z$  to eliminate  $\frac{1}{\partial z^2}$  leads to equation(2-13) [22]:

$$\bar{v} = \frac{1}{h} \int_0^h v_x dz = -\frac{h^2}{3\mu} \frac{\partial P}{\partial x} \quad (2-13)$$

The gravitational potential energy density can be calculated with the following equation (2-14), where  $\rho$  is the density in  $[\frac{\text{kg}}{\text{m}^3}]$ ,  $g$  is the gravitational acceleration which is  $9.81 \frac{\text{m}}{\text{s}^2}$ ,  $h$  is the height in  $[\text{m}]$ , therefore  $\Phi_G$  is expressed in  $[\frac{\text{kg}}{\text{m s}^2}]$  or  $[\frac{\text{J}}{\text{m}^3}]$  [22].

$$\Phi_G = \rho \vec{g} h \quad (2-14)$$

The pressure  $p$  in equation (2-6) is the product of the surface tension  $\gamma$  in  $[\frac{\text{J}}{\text{m}^2}]$  and the local curvature  $\kappa$  in  $[\text{m}^{-1}]$ , which is  $\frac{1}{R}$  where  $R$  is the local radius. If only tiny are considered resulting in drops with only a slight curvature, then an influence of the curvature on the fluid flow can be neglected [22].

Furthermore, the quantity  $\Phi_M$  is the difference between the intermolecular forces between liquid molecules and solid molecules of the solid surface, therefore  $\Phi_M$  can be differentiated into  $\Phi_M - \Phi_{MF}$  where,  $\Phi_M$  is the energy density between the liquid molecules at the top of the drop and  $\Phi_{MF}$  is the energy density of the liquid molecules interacting with the surface [22]. Here the wetting and, therefore, the contact angle between the liquid and the surface is essential, and as mentioned, the surface is thoroughly wetted, and the contact angle must be set to 0:  $\alpha \rightarrow 0$  [22]. An analysis from Miller et al. delivers a description of a fluid interface moving along a solid surface during

wetting and predicts that the contact angle will exceed its equilibrium value at an advancing contact line, that is, one where liquid replaces gas in contact with the solid.

[40] Miller's analysis yields the following equation for  $\Phi_M - \Phi_{MF}$  [22]:

$$\Phi_M - \Phi_{MF} = \frac{\pi}{12d^3} (n_L^2 \beta_{LL} - n_L n_S \beta_{SL}) G(\alpha) - \frac{\pi}{12d^3} n_L n_S \beta_{SL} G(\pi - \alpha) \quad (2-15)$$

With [22]:

$$G(\alpha) = \csc^3 \alpha + \cot^8 \alpha + \frac{3}{2} \cot \alpha \quad (2-16)$$

It should be mentioned that the parameters  $\beta_{SL}$  and  $\beta_{LL}$  are inherited from the London-Van der Waals interactions between molecules [22]. Distance  $d$  is the length between a point of interest and the contact line and  $\alpha$  is the contact angle mentioned above and  $n_L$  and  $n_S$  are the molecular densities of the liquid and solid phases. As  $\alpha = 0$ , the equations above simplifies to  $G(\alpha) = (\frac{2}{\alpha^3})$  and  $G(\pi - \alpha) = 0$ , yielding [22]:

$$\Phi_M - \Phi_{MF} = \frac{\pi(n_L^2 \beta_{LL} - n_L n_S \beta_{SL})}{6h^3} = -\frac{K}{h^3} \quad (2-17)$$

Additionally,  $d$  was substituted with the height  $h$  of the drop and the upper term is now the parameter  $K$ . Lopez et al. states that the right side of the upper equation describes the so-called disjoining pressure and designates it as “the difference in behaviour between a liquid thin film and bulk liquid phase”[9]. Furthermore, the variations in disjoining pressure can cause a liquid flow in the outer regions of the drop, and it is only essential for layers with a thickness thinner than the effective intermolecular force [22, p. 463]. To summarise, the energy densities from the pressure  $p$  and  $\Phi_M - \Phi_{MF}$  Are neglectable compared to the influence of  $\Phi_G$ , when describing the initial phase of the liquid drop spreading. But for a far-spread drop  $\Phi_M - \Phi_{MF}$  must be considered again. The equations

for  $\Phi_M$ ,  $\Phi_G$  (neglecting  $p$ , since the curvature is slight) can be inserted into  $P$  from (2-13) leading to the following equations (2-18) and (2-19) [22, p. 463]:

$$P = \rho gh - \frac{K}{h^3} \quad (2-18)$$

$$\bar{v} = -\frac{h^2}{3\mu} \left( \frac{\rho gh}{\partial x} + \frac{K}{h^3} \frac{1}{\partial x} \right) \quad (2-19)$$

Since the height  $h$  is changing with a change in  $x$ , the equation (2-19) can be expanded with  $\frac{\partial h}{\partial x}$  [22]:

$$\bar{v} = -\frac{h^2}{3\mu} \left( \frac{\rho g}{\partial x} \frac{\partial h}{\partial x} + \frac{K}{h^4} \frac{\partial h}{\partial x} \right) \quad (2-20)$$

To solve the equation system, the conservation of mass must be considered, which arises from the Navier-Stokes equation and is described via a continuity equation. A continuity equation states that a quantity which is transported must be constant over a change of time  $\frac{\partial q}{\partial t}$  and a spatial change which is expressed in the form of the divergence of a vector field describing the flow of the quantity and can be expressed in the following equation in a differential form [37]:

$$\frac{\partial q}{\partial t} + \nabla \cdot j = \sigma \quad (2-21)$$

Where  $q$  is the quantity per unit volume,  $j$  is the vector field of the quantity,  $\nabla$  the divergence and  $\sigma$  the generation of the quantity per unit volume per time. Since mass is volume times density and the volume of an axisymmetric drop can be expressed in terms of the height, the continuity equation can be expressed as:

$$\frac{\partial h}{\partial t} = -\frac{1}{x^{q-1}} \frac{\partial}{\partial x} (x^{q-1} \bar{v} h) \quad (2-22)$$

The exponent  $q$  describes two cases, first the shape invariant case for  $q = 1$  and the axisymmetrical case  $q = 2$ . The equation for the velocity (2-20) above can be inserted into (2-22) [22]:

$$\frac{\partial h}{\partial t} = -\frac{1}{3\mu x^{q-1}} \frac{\partial}{\partial x} \cdot \left( \rho g h^3 x^{q-1} \frac{\partial h}{\partial x} + \frac{3K}{h} x^{q-1} \frac{\partial h}{\partial x} \right) \quad (2-23)$$

The obtained non-linear second-order partial differential equation (PDE) can be solved to describe the drop height depending on time  $t$  and the  $x$  coordinate  $h(t, x)$ . Lopez et al. states that a drop symmetry implies the following boundary condition and that the differential can be solved with a known start volume [22] :

$$\frac{\partial h}{\partial x} = 0 \text{ for } x = 0$$

The start volume of a drop can be calculated with integration, where  $x$  is equivalent to a radius  $r$ . As a result, the integration is done over many small radii pieces  $dx$ , from the centre towards the outside. Therefore, one can integrate with lower equals to 0 (centre of the drop) until the upper limit, infinity (since the starting condition assumes complete wetting and infinite surface).

$$V = (2\pi^{q-1})h \int_0^\infty x^{q-1} dx \quad (2-24)$$

To solve the PDE, Lopez et al. used a similarity solution. If the independent and dependent variables of a PDE are correctly scaled, a self-similar solution is a type of solution that is like itself. This can simplify a PDE to an ODE and therefore finding a solution may be more trivial. For this reason, Lopez et al. took the following equation as a similarity solution to the PDE, where  $x_o(t)$  is a measure of how far the drop has spread [22] :

$$h(x, t) = F_1(t)/F_2(x/x_o(t)) \quad (2-25)$$

According to the similarity solution, Lopez states the following equation, which fits the similarity solution as the boundary condition:

$$h(x, t) = \frac{V}{2w(q)x^{q_0}(t)} \left(1 - \left(\frac{x}{x_0}\right)^2\right)^{\frac{1}{3}} \quad (2-26)$$

With:

$$x_0(t) = \left(\frac{(3q+2)}{36[w(q)]^3} \cdot \frac{V^3 \rho g t}{\mu}\right)^{\left(\frac{1}{3q+2}\right)} \quad (2-27)$$

And with:

$$w(q) = \frac{\pi^{\frac{q}{2}}}{3q+2} \cdot \frac{\Gamma\left(\frac{1}{3}\right)}{\Gamma\left\{\left(\frac{1}{2}\right) + [(-1)^q/3q]\right\}} \quad (2-28)$$

Here  $\Gamma$  is the gamma function, which is defined as the following:

$$\Gamma(x) = \int_0^{\infty} u^{x-1} e^{-u} du \quad (2-29)$$

Additionally,  $x$  is a point on the x-axis of the drop, which is divided by  $x_0(t)$ , which describes the increases of the drop radius over time. Also,  $x_0(t)$  incorporates the volume  $V$  of the drop, the density  $\rho$ , the viscosity  $\mu$  and the term  $w(q)$ . The term  $w(q)$  utilising the gamma function describes the shape of the drop regarding the parameter  $q$ , which describes if the drop is cylindrical or not. The gamma function is a solution to an interpolation problem for a factorial sequence and is commonly used in physics, especially for problems dealing with decay over time [41]. Chen et. al reorganised the Lopez equation and delivered a simplified equation for the gravitational regime:

$$h = \frac{1}{\pi} \left( \frac{\mu V}{0.136 \rho g} \right)^{\frac{1}{4}} \cdot t^{-\frac{1}{4}} \quad (2-30)$$

where  $h$  is the thickness of the drop in its centre,  $V$  is the drop starting volume,  $\rho$  is the materials density and  $g$  is the earth acceleration, and  $t$  is the time. Chen mentions that this formula can be applied if the capillary length  $\lambda_l$  is much smaller than the radius of the drop  $R$  and  $\lambda_l$  can be calculated with:

$$\lambda_l = \sqrt{\frac{\gamma_{LV}}{\rho g}} \quad (2-31)$$

Here  $\gamma_{LV}$  is the surface tension between the liquid-vapour phases. From observing the Lopez model, the drop spreading is described for an infinitesimal long horizontal surface, whereas the Deep Dip scenario assumes only a finite platform below the drop. Therefore, the Lopez model is not suited for the Deep Dip model and must be modified analytically or empirically. Unfortunately, solving the Navier-Stokes equations is not trivial, and therefore the drop spreading model will later be modified empirically. Additionally, the Chen equation can be applied if the conditions are met.

### 3. Experiments

In 1.3. the overall goal of this work was formulated to build a P $\mu$ SL system for microfabrication. In the subchapter 2.2.1 and 2.2.2 it was pointed out that the Deep Dip method is a viable and simple method to generate new liquid photopolymer layers in a top down P $\mu$ SL systems for recoating and layer generation purposes. Furthermore, in 2.2.2 the work from W. Tan et al. was discussed which indicates that in the Deep Dip method two main parameters namely the viscosity of the used photopolymer and the build platform to resin vat ratio influence the average layer thickness strongly, but as W Tan et al suggests, they must be proven with experimental results. Furthermore, no research on mathematical models can be found for the Deep Dip method as stated in 1.2, where only the mathematical model from Lopez et. al comes close to the actual Deep Dip scenario but does not represent it accurately, which was discussed in the beginning of 2.4. However, this model may be used as representation of the planned Deep Dip analyses and may be altered empirically to fit the actual measurements, and this will be discussed in chapter 7. Therefore, a parameter analysis shall be conducted to prove the previous stated dependencies from W. Tan. et al. as well as search for additional ones in the experiment 1 in chapter 5 to get a better understanding of the underlying Deep Dip process. As stated in 2.3.4 the viscosity of a fluid can be lowered by increasing its temperature, which should subsequently result in lower layer heights or shorter settling times for new layers which will be advantageous for the printing process. Therefore, the experiment 1 from chapter 5 will be expanded in experiment 2 in chapter 6 by analysing new layers after heating the photopolymer. In the 3rd planned experiment a first layer shall be cured and solidified, and new layers will be generated on top of it. Here the found Deep Dip parameters from experiment 1 and 2 will be applied. The underlying photopolymerization processes were discussed in chapter 2.3.

As mentioned previously for the planned printing process with the P $\mu$ SL system a defined layer height and a defined radius of curvature (ROC) must be achieved for a given set of Deep Dip parameters. Additionally, it would be ideal to obtain a consistent layer height and a very high *ROC* resulting in a flat layer. Therefore, for the parameter analysis two metrics were chosen to characterise any obtained layers: first the maximum layer height  $H_{max}$  and second the *ROC* of the layers. The dependencies of different Deep Dip parameters onto  $H_{max}$  and *ROC* can be seen in Figure 3-1:

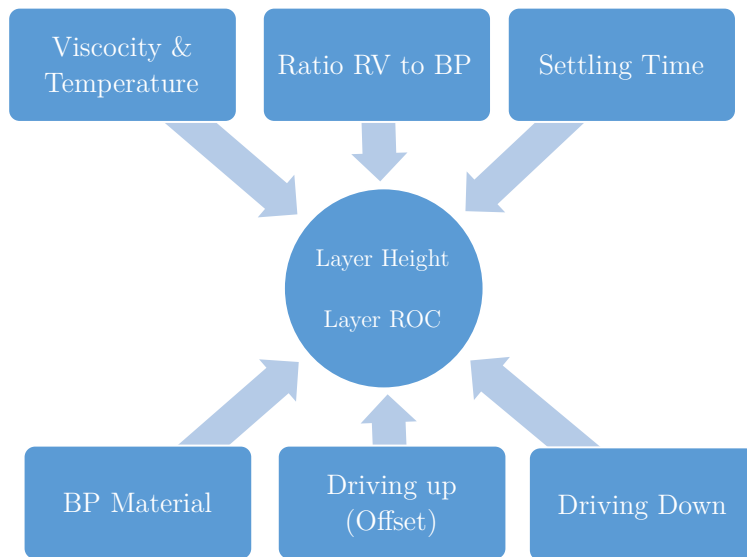


*Figure 3-1: The influence of specific parameters on the layer height and the layer ROC for the Deep Dip procedure.*

Here in Figure 3-1, additional influences like the build platform material can be seen but will be ignored in this work. Furthermore, two new Deep Dip parameters are added namely Driving Down and Driving Up (Offset), since they can influence the Deep Dip layer height and they will be discussed in more detail in chapter 67.

### 3.1. P $\mu$ SL Setup

As mentioned in the beginning of chapter 3, the overall goal of this works is to develop a P $\mu$ SL setup for printing small scale optics and actuators and as a result a conceptual system, was developed similar to the P $\mu$ SL systems described in section 2.1.1 and can be seen in Figure 3-2:

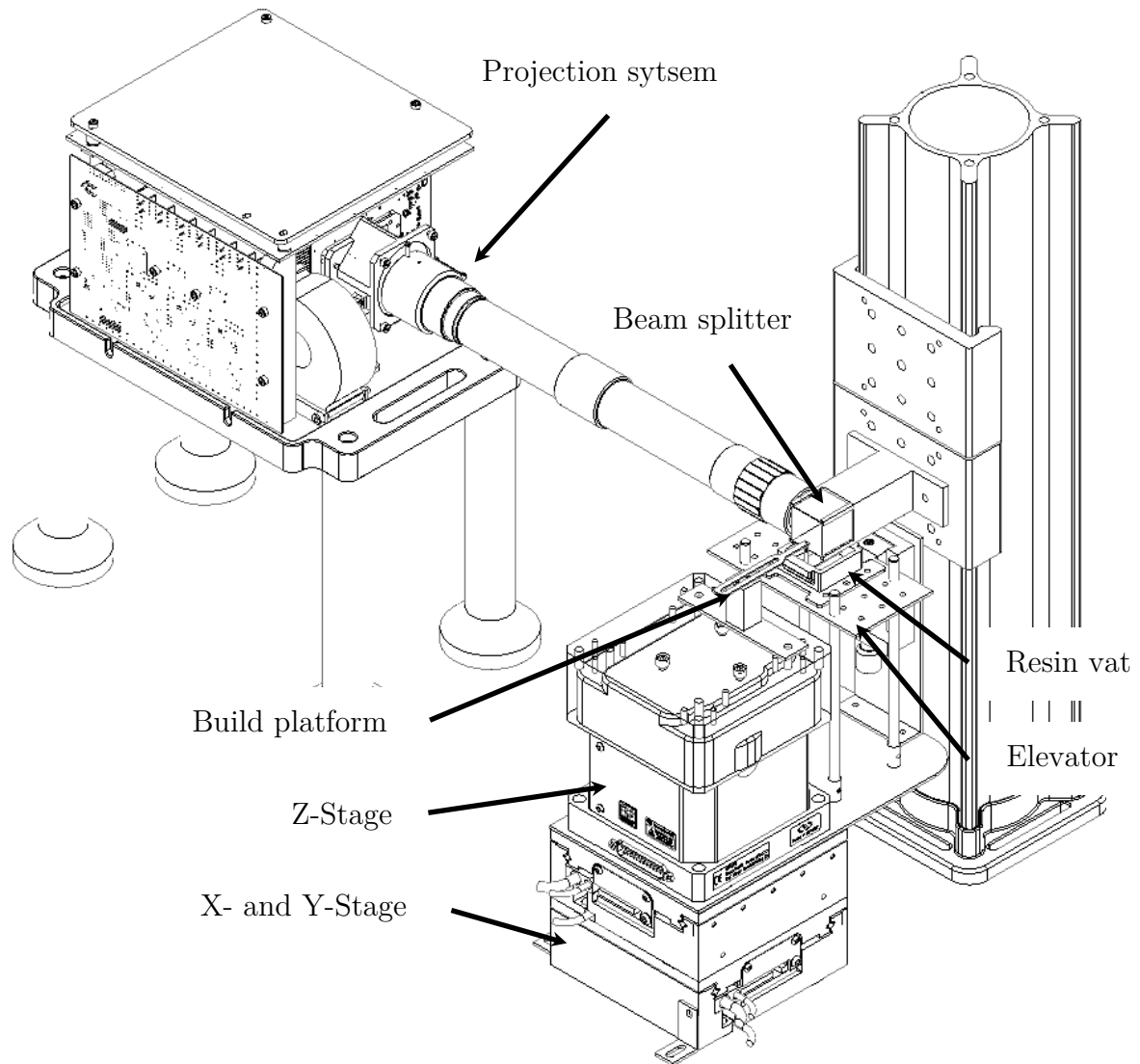


*Figure 3-2: The conceptual P $\mu$ SL system.*

As it can be seen Figure 3-2. The P $\mu$ SL system consists of two stages for the x-y-axes beneath one stage for the z-axis. Between the x-y-stage and the z-stage a platform is attached where on top of it an elevator is placed sliding between four lines rails. The

elevator can be moved in z-direction via a manual z-stage. Attached to the z-stage is a build platform which is placed into the resin vat, which is attached to the elevator. Above the build platform is an optical beam splitter, which is used to redirect the light coming from the DMD projection system onto the build platform inside the resin vat. The projection system was placed on pillars to reach the desired height and points directly at the beam splitter above the build platform. Furthermore, the beam splitter is attached to a linear rail so that it can be translated in z-direction. The build platform can be moved with the z-stage in z-direction to allow the recoating and generation of new layers. Additionally, with the x-y-stage, the z-stage as well as the build platform and resin vat can be moved relative to the beam splitter. Therefore, multiple images from the projector can be stitched together increasing print area. Furthermore, a camera system can be mounted over the beam splitter to monitor the entire printing process

This conceptual setup will be used and modified in order to construct a setup that can generate and analyse defined layers using the Deep Dip method which will be discussed in the next subchapter 3.2.

### 3.2. Setup for Deep Dip Analysis

For the Deep Dip analysis, the conceptual P $\mu$ SL setup from 3.1 was modified to enable the measurement of liquid photopolymer layers and can be seen here in Figure 3-3 and subcomponents can be seen in Figure 3-4, Figure 3-5 and Figure 3-6 on the next page.

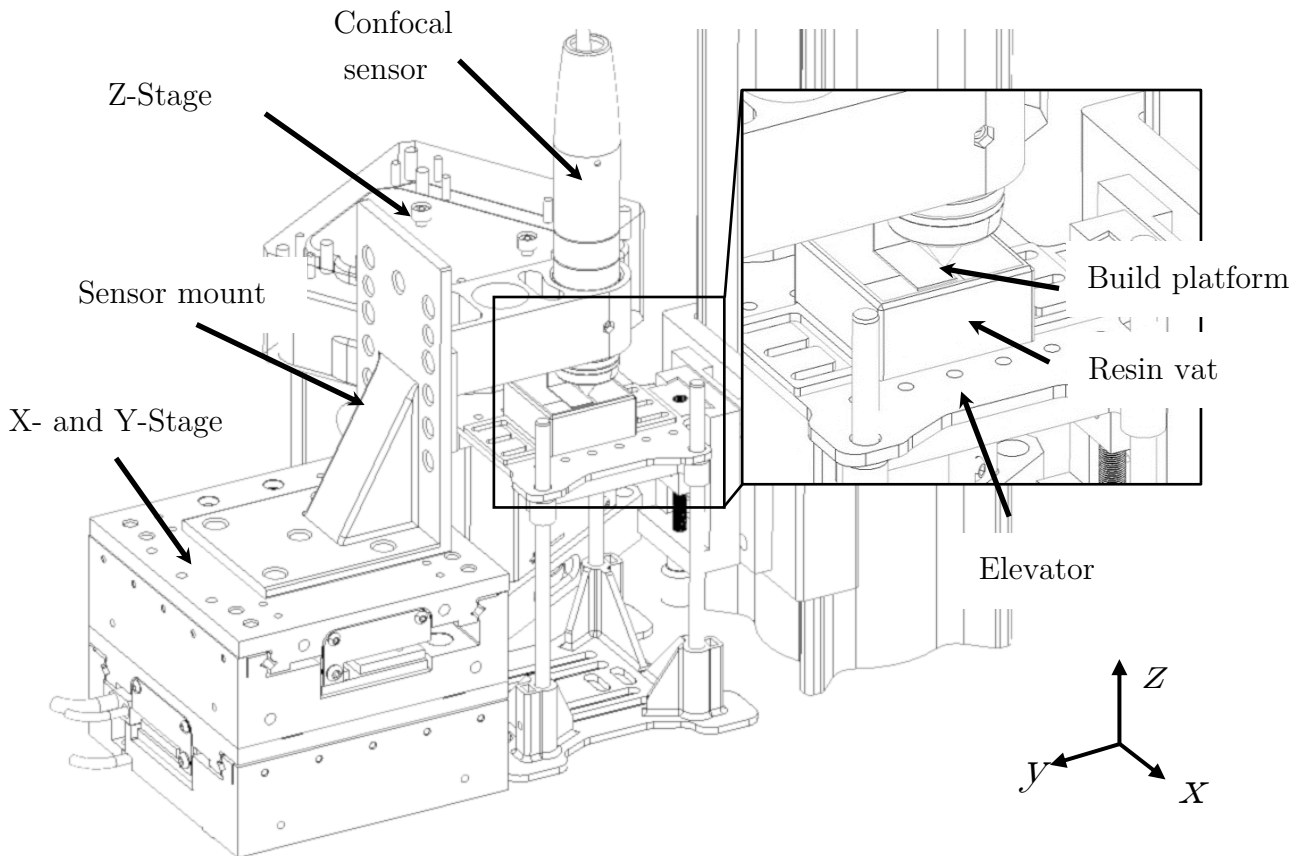


Figure 3-3: Complete assembly of the experimental setup, with the confocal chromatic sensor pointing next to the build platform.

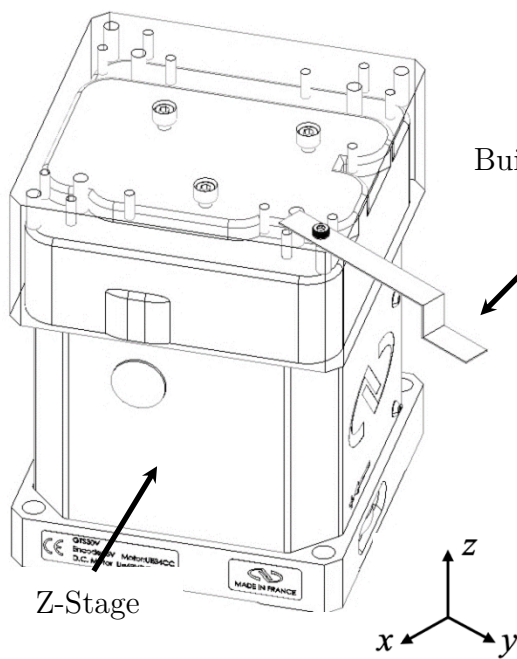


Figure 3-4: Aluminium metal strip build platform attached to the GTS30V functioning as the z-axis.

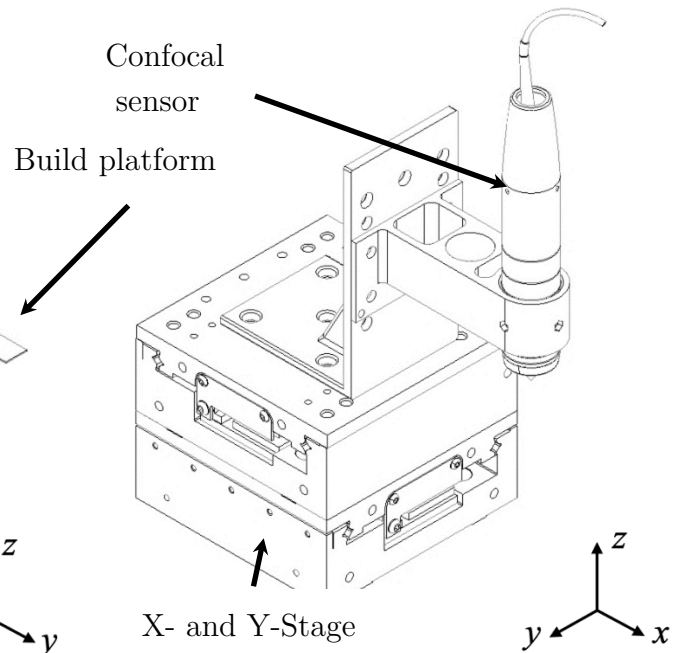
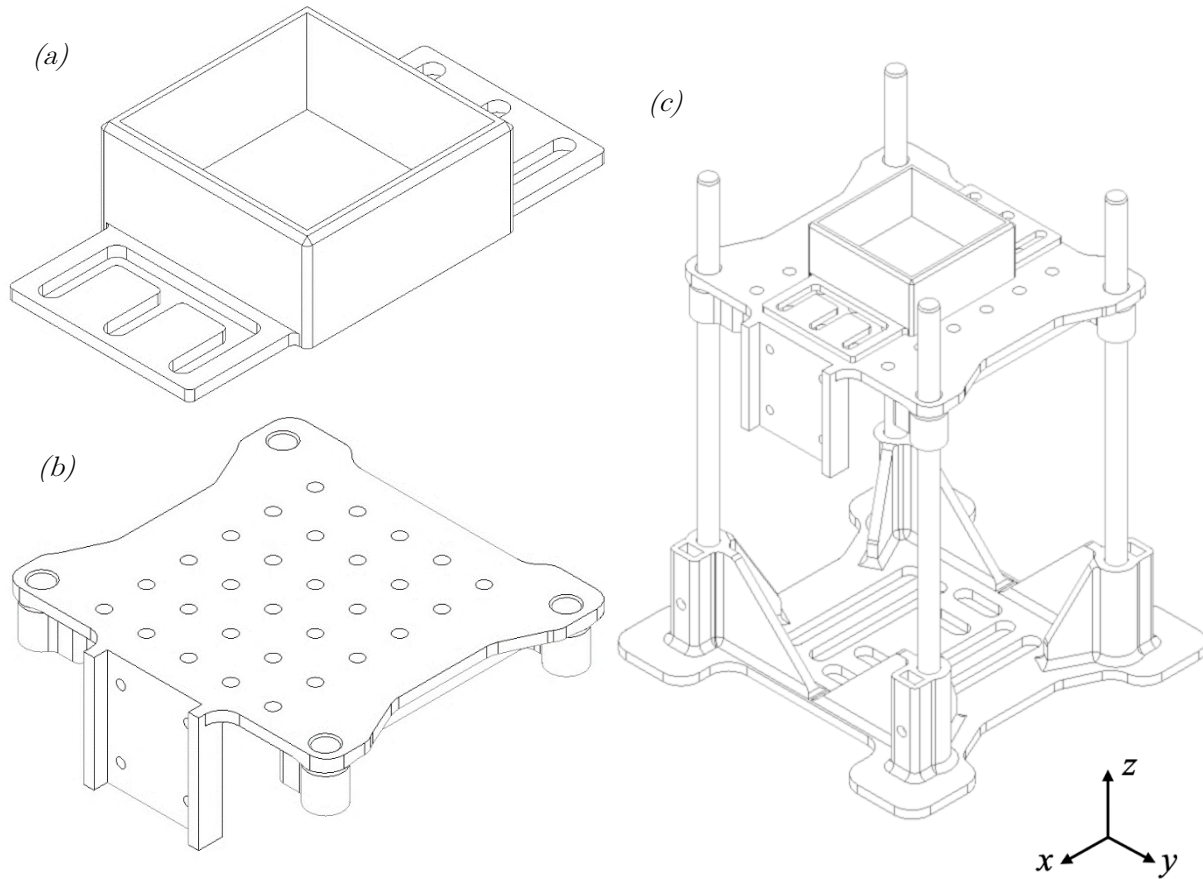


Figure 3-5: IFS2405 optical head attached to the XMS50S stages for the x-y-axis via an FDM 3D printed adapter.

In Figure 3-4 it is shown that the build platform which is an aluminium metal strip bent over two times to achieve the typical platform shape is attached to the z-stage and the end part of the build platform has a rectangular shape with a width of 10 mm and a length of 20 mm. Since the build platform is attached to the z-axis, translation in z-direction was achieved to execute the Deep Dip movement as it was explained in 2.2.2.

As it can be seen in Figure 3-5, this setup features two x-y-stages like the P $\mu$ SL concept to allow sensor movement in x and y-direction and therefore the confocal sensor was attached to the x-stage through an 3D printed sensor mount. The y-stage was placed and connected beneath the x-stage and both axes were connected to the optical table.

The two x- and y-stages feature a resolution of 1  $\mu$ m and the z-axis a resolution of 0.1  $\mu$ m. The x-y-axes can be translated with -25 mm and +25 mm, resulting in a 50 mm travel range in both directions (x-axis and y-axis). The z-stage has a travel range of -5 mm in the negative z-direction and +25 mm in the positive z-direction, resulting in a 30 mm travel range for the z-axis. For the z-axis, a GTS30V stage from Newport was used and for the x-y-axes two XMS50S stages from Newport were used.



*Figure 3-6: (a) Showing the 3D printed resin vat. (b) The platform. (c) Assembly of resin vat, build platform and adaptor for the linos rails.*

In Figure 3-6 the elevator is shown in (c) consisting of a resin vat (a) and a platform (b). In this setup, the elevator is used to adjust the height of the resin vat in z-direction relative to the build platform. Moreover, the platform is sliding in 4 guide rails providing additional stability and is connected to a manual OWIS stage in the z-direction, which can be seen in Figure 3-3. This manual stage enables translation of the elevator in z-direction and will be used to setup the fill stand of the resin vat for the experiments. The manual z-stage is connected to a Linos X95R guide rail which is vertically fixated to the optical table. The resin vat which can be seen in Figure 3-6 (a) was 3D printed via FDM, with a width of 30 mm, a length of 30 mm and a height of 10 mm.

Additionally, a lab intern logging device was employed to log environmental data like temperature, humidity, and pressure.

All in all, the setup it allows for accurate and automatic positioning of the confocal sensor in the x and y direction as well as accurate positioning of the build in the z-direction. The resin vat position with the liquid photopolymer can be adjusted in the z-direction manually. Additionally, the setup was built inside a climate-controlled box to block stray light and minimize temperature changes from outside air flow. The entire experimental setup can be seen here:

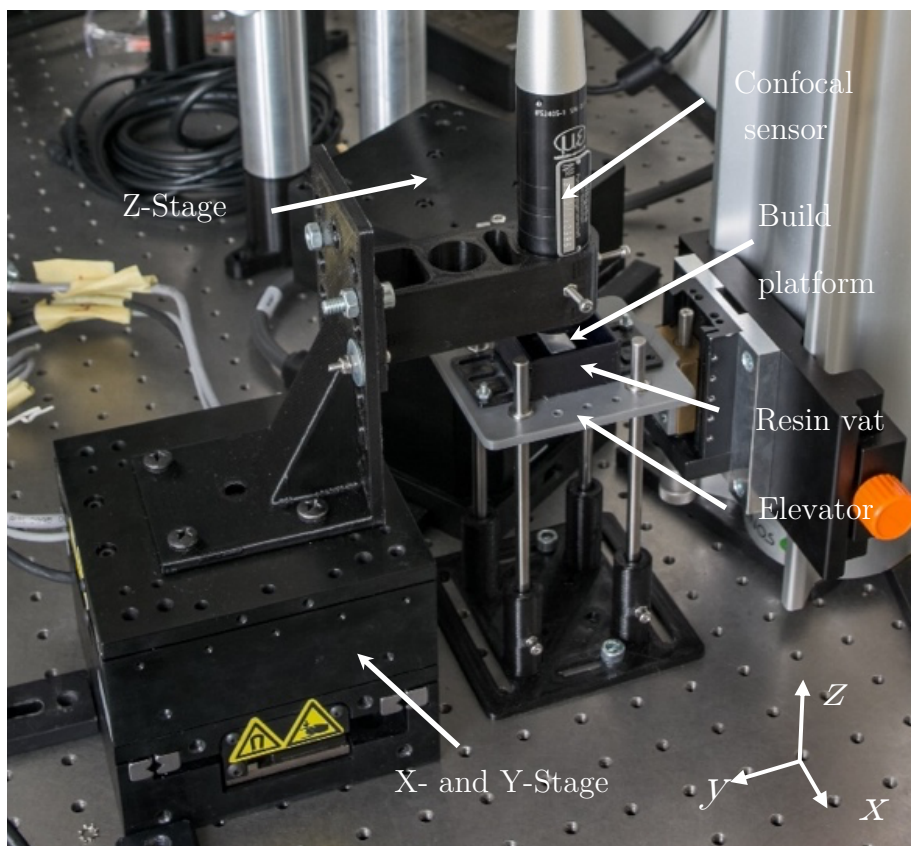


*Figure 3-7: Complete real assembly of the experimental setup.*

### 3.3. Software for Controlling Measurement Setup

An object-oriented software system was programmed to control the three axes configuration in previous work and therefore it is consisting of various classes. The software system was extended to control the axes with GCode commands. Where GCode is the standard language used to control hardware in the computer aided manufacturing (CAM) space and contains an instruction list. This choice was made to allow flexible

control of the system while not reprogramming the software system multiple times when a new movement path is changed. For this reason, the GCodeReader class was extended with new GCode entries. The responsibility of the GCode reader class is to read in GCode and parse the contained GCode commands into a list of instructions. The GCodeExecution class then executes this instruction list. The following flow charts represent the workflow of the GCodeReader and GCodeExecution classes. Additionally, a class for the confocal sensor ConfocalIDT was extended. This class connects to the confocal sensor and controls and sets up its measurement parameters.

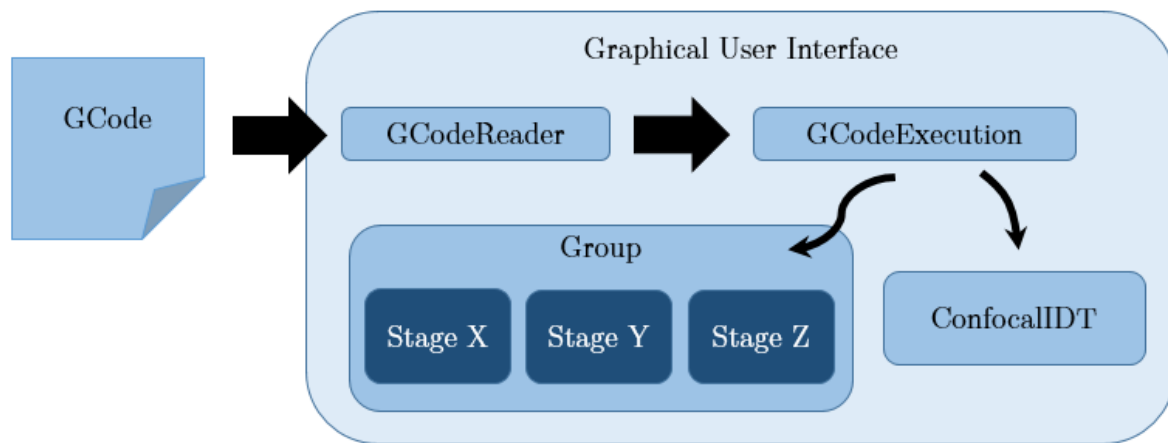


*Figure 3-8: Software system programmed in previous work which is comprised of different classes to control the measurement setup.*

### 3.4. Validation measurements

Before any actual measurements were conducted, validation measurements were executed for a proof of concept. First a test of the z-axis stage was conducted and will be described in section 0. Second the confocal sensor's ability to measure a layer of the liquid photopolymer tested and will be discussed in section 3.4.2.

### 3.4.1. Movement Validation Z-Axis

The z-axis stage was tested explicitly since the z-axis movement precision directly influences the generated layer height and therefore was characterised as important for the upcoming experiments. The measurement was conducted by attaching the confocal sensor directly above the z-stage with about 5 mm distance and moving it according to a defined set of movement instructions. The movements contained a variety of up and down movements with different speeds. With the confocal sensor, the distance of the z-stage to the sensor was measured, and a statement of the stage accuracy can be made. The accuracy of 28 nm of the sensor exceeds the accuracy of the z-stage of 100 nm and therefore was suited for this measurement.

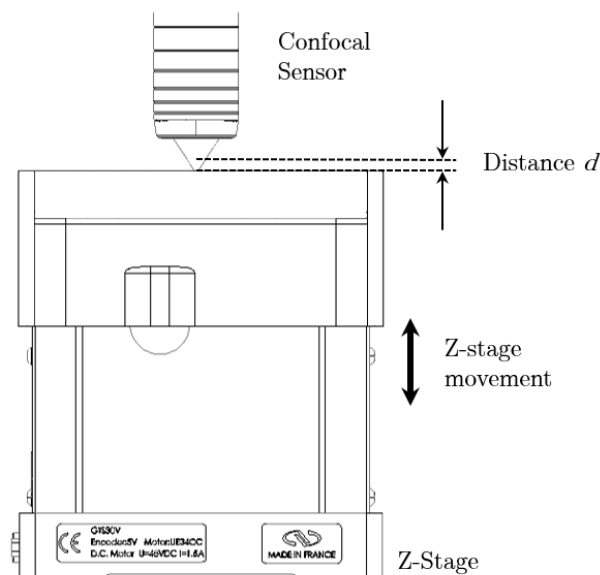


*Figure 3-9: Setup for the z-stage validation.*

In

Figure 3-9 it is shown that the test the stage was set to cycle between two positions periodically ten times. Three distances were set: 100  $\mu\text{m}$ , 10  $\mu\text{m}$  and 1  $\mu\text{m}$ . Furthermore, the movement for each distance value were performed using 3 different velocities. The test run was completed using relative movements. The following Table 3-1 shows the three distances with each 3 different velocities.

Table 3-1: Showing the distance and velocity pairs for the axis test.

Distance $d$ in [ $\mu\text{m}$ ]	100			10			1		
Velocity $v$ in [ $\mu\text{m/s}$ ]	100	50	10	10	5	1	1	0.5	0.1

For each test run, the actual driven distance was measured with the confocal sensor. The results were analysed by computing the mean and standard deviation of all 10 cycles for each test run. The results can be seen in Figure 3-10:

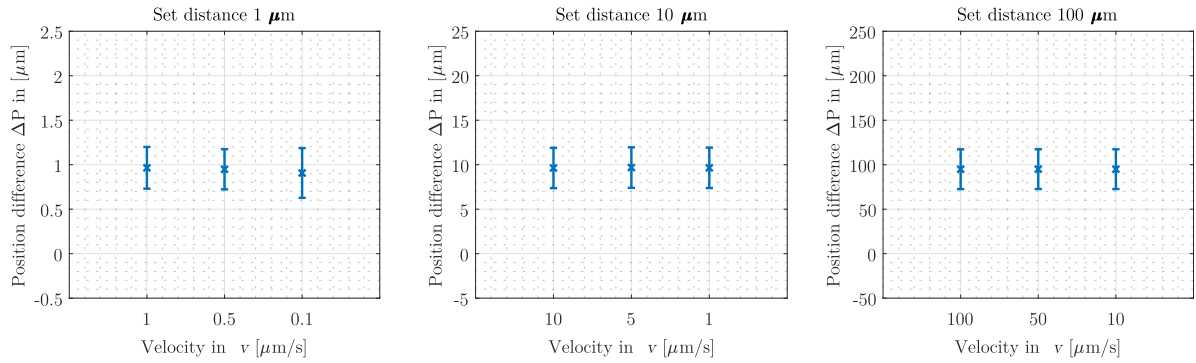
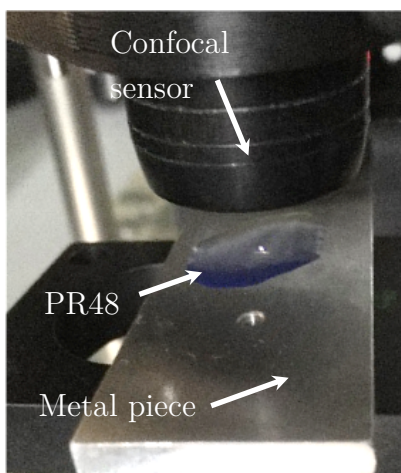


Figure 3-10: Showing the position differences for 1  $\mu\text{m}$ , 10  $\mu\text{m}$  and 100  $\mu\text{m}$  set values for 3 different velocities.

From Figure 3-10 it can be concluded that the mean values of the measurements do match the expected set values. Additionally, we can say that the mean distance value is mostly independent of the used velocity. The standard deviation is for 1  $\mu\text{m}$  set value, around 0.2  $\mu\text{m}$ . For 10  $\mu\text{m}$  the standard deviation is about 2  $\mu\text{m}$  and for 100  $\mu\text{m}$  the standard deviation is around 20  $\mu\text{m}$ . Therefore, the standard deviation is highest for greater distances. The measured deviations in z-stage movement will consequently introduce errors into the layer measurements and layers with a 20  $\mu\text{m}$  thickness may not be able to be measured.

### 3.4.2. Confocal Sensor Test

To test the ability of measuring layers of PR48 a pre-test was conducted. Here the sensors' ability to measure a liquid layer of PR48 on top of a piece of aluminium should be shown since experiment 1 will be conducted with PR48 and an aluminium build platform. The confocal sensor was positioned directly above the metal piece with around 5 mm distance. Thickness was measured via the thickness measurement mode as it was previously discussed in section 2.2.4. Additionally, the spectral signal of the sensor was recorded. To cancel out the dispersion effect of PR48 in the spectral signal, the Abbe number and refractive index of PR48 at room temperature 21°C were fed into the sensor settings. The measurement configuration can be seen in and the sensor signal can be seen in Figure 3-12 here:



*Figure 3-11: Measurement Setup for the confocal test where the confocal sensor in black is above the bluish PR48 liquid. The white dot is the measurement spot*

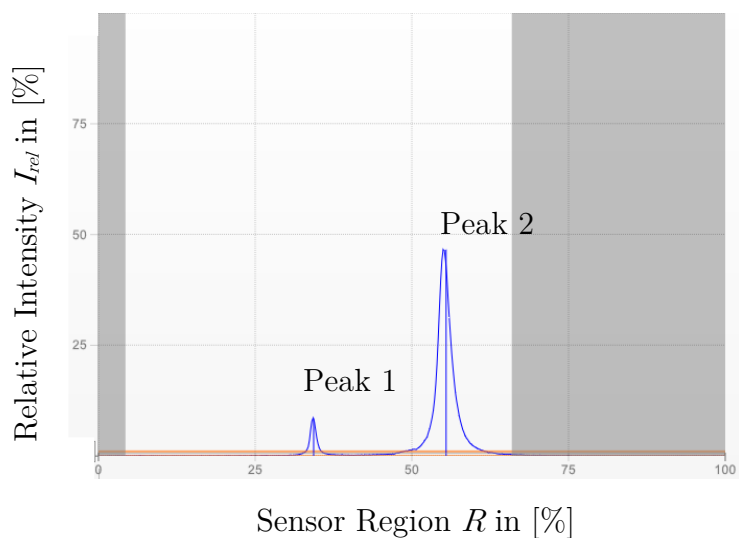


*Figure 3-12: Spectral signal for a PR48 drop on an aluminium surface.*

From Figure 3-12 can be stated that the sensors spectral signal shows two peaks, where the peak 1 is the first peak received from the sensor and peak 2 is the second peak received by the sensor. Since peak one is received first, it corresponds to a shorter wavelength and therefore must represent the liquid PR48 surface. The peak 2 represents the aluminium surface. Furthermore, the peak 2 is higher in its intensity, which is the result of the higher reflectivity from the aluminium surface. It should be mentioned, that when the thickness of the PR48 layer is reduced, the two peaks merge together and therefore, the sensor cannot distinguish between the two surfaces, and this is shown in Figure 3-13:

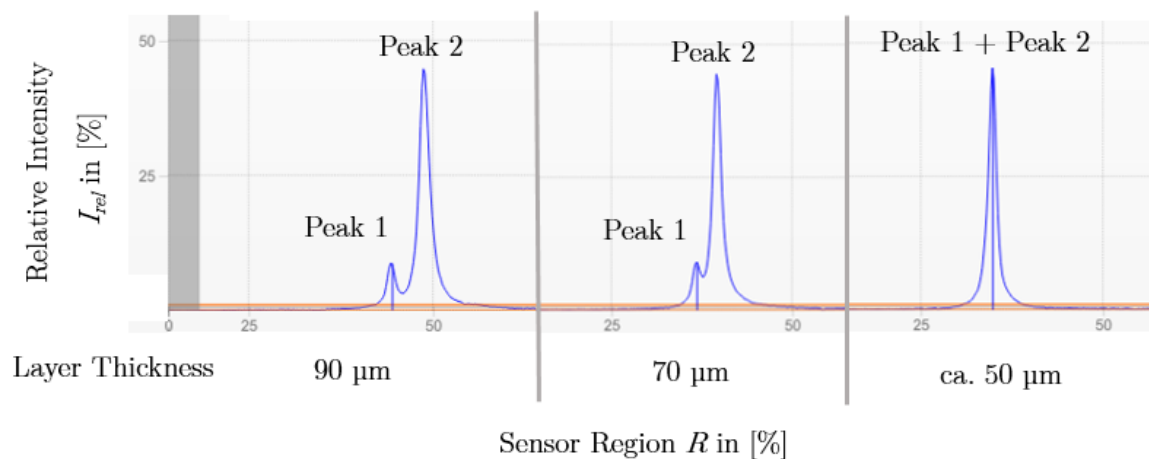


*Figure 3-13: Showing the spectral signal for three different layer heights, where in the last spectral signal, the 2 Peaks are not distinguishable.*

In Figure 3-13 three separate measurements of the spectral signal are shown each for a different layer thickness. The two peaks correspond to the liquid PR48 surface and the aluminium surface like stated before. For a layer thickness of 90  $\mu\text{m}$  the two peaks are separated and can be distinguished. At 70  $\mu\text{m}$  the two peaks start to merge but still can be differentiated. Coming to a layer thickness of about 50  $\mu\text{m}$  the 2 peaks are too close together and only the aluminium surface reflection can be recognized. As a result, in the thickness measurement mode only layer heights above 50  $\mu\text{m}$  can be measured. Finally,

we can state that a thickness measurement of PR48 can be conducted up to 50  $\mu\text{m}$  and therefore the chromatic confocal measurement principle can be used for the upcoming experiment as long this minimum layer thickness is not below this threshold.

## 4. Experiment Methodology

For experiment one, two and three, the Deep Dip parameters discussed in chapter 3 will be altered. Because of this we will discuss the parameter from Figure 3-1 explaining their definition and the reason for using them. From the parameter for driving down the build platform shall be called Deep Drive Down ( $DDD$ ), and the driving up of the build platform shall be characterised as an Offset called Deep Dip Offset ( $DDO$ ) and they can be seen in Figure 4-3.

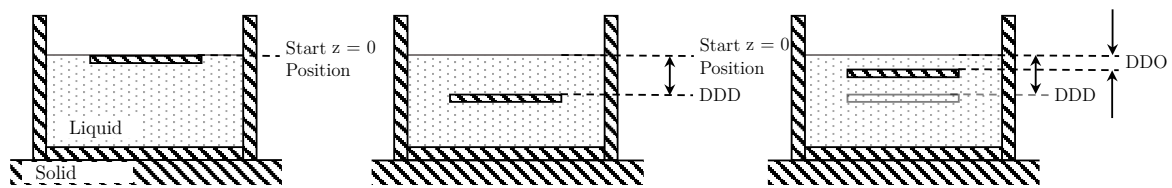


Figure 4-1: The definition of the  $DDD$  and the  $DDO$  parameters.

From Figure 4-1 it can be observed that the  $DDD$  parameter is defined as the distance from the liquid surface to the upper build platform surface after downwards movement and the  $DDO$  parameter is defined as the distance between the upper surface of the build platform to the liquid surface.

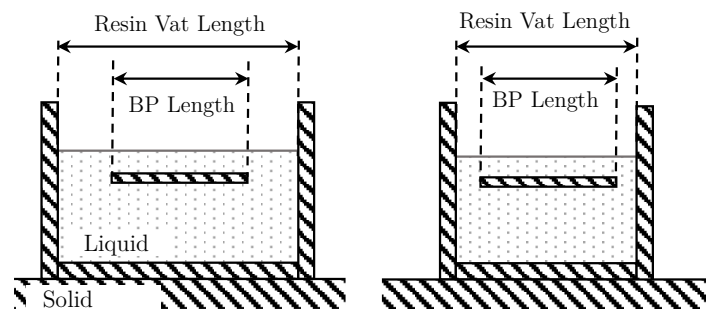


Figure 4-2: The BP to RV ratio is simply the ration between the BP length and resin vat length  
in  $y$ -direction

In Figure 4-2 the BP to RV ratio is defined as the length of the build platform divided by the length of the resin vat.

As previously stated in the beginning of chapter 3 the goal is to find additional dependencies and for this reason the *DDO* parameter was chosen for the experiments since it is suspected to have an impact onto the final layer height and *ROC*. For example, as earlier described in section 2.2.2 in Figure 2- if the *DDO* parameter is negative then the build platform is below the initial liquid surface and a new flat layer should form with a thickness equal to the *DDO* value. Otherwise, if the *DDO* is positive then the build platform is above the initial liquid surface and the liquid should flow downwards to the sides forming a convex shaped layer. Additionally, it is suspected, that the viscosity has a strong impact on the liquid flow which was discussed in section 2.3.4. Therefore the *DDO* parameter shall be investigated in more detail in experiment 1 and the viscosity will be altered in experiment 2. Furthermore, the *DDD* parameter will be changed too since it is suspected to influence the initial amount of liquid photopolymer above the build platform after it was emerged from the liquid influencing the final layer height. In addition, from the discussion in subchapter 2.2.2 it is known that the build platform to resin vat ratio also influences the final layer height and therefore this parameter will be changed throughout the experiment 1 too.

## 4.1. Layer Measurement Methods

In this subchapter the actual layer measurement methods will be discussed. Therefore, the possible confocal sensor scans will be explained in section 4.1.1 and subsequently the data post processing and data extraction will be described in the following section 4.1.2.

### 4.1.1. Confocal Sensor Scan

As mentioned in 3.2. the confocal sensor was attached to x-y-stage enabling sensor movement in two directions. Therefore, multiple ways of measuring the photopolymer

layers are possible like an 2d mapping of a layer, a linear scan or a dot measurement can be utilized. All three methods can be seen in Figure 4-3.

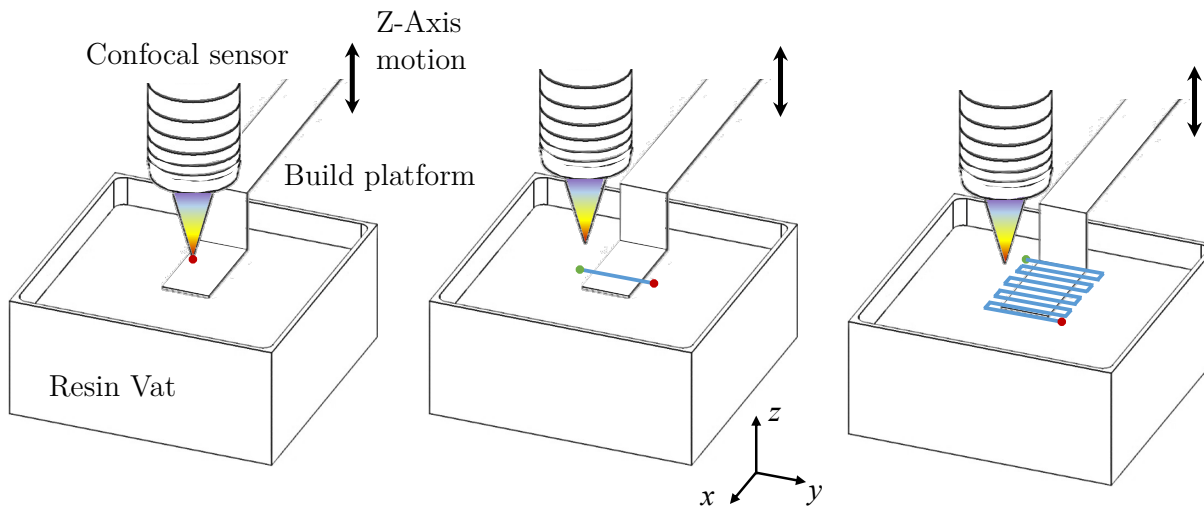


*Figure 4-3: Resin vat filled with liquid polymer and the BP with the confocal sensor on top. On the left-hand side the dot scan is shown, in the centre the line scan is shown and on the right-hand side the mapping procedure is shown. A green dot is the start point of a movement path and a red dot is the end point. The blue lines correspond to the path.*

In Figure 4-3 on the left-hand-side the dot measurement can be seen where the sensor is placed without any motion above the build platform while the Deep Dip recoating method is performed as it was described in 2.2.2 and during the execution the confocal sensor measures the thickness of the generated layer. Because of its one-dimensional nature, the dot method cannot obtain any 2-dimensional data of the surface and therefore no ROC can be measured, which is an important metric for this experimental part. As a result, the experiments will not be performed with this method.

Another method that can be seen in Figure 4-3 in the center where the sensor translates along a single axis to perform a line scan while the Deep Dip procedure is executed. Here in contrast to the dot method, 2-dimensional data can be generated and therefore the ROC and the  $H_{max}$  can be measured and analyzed. Therefore, this measurement method will be used throughout the experiments to measure the obtained layer thickness over time

during the Deep Dip process, since this method can be executed fast enough, so that the layer motion in the Deep Dip method still can be measured.

Additionally, in Figure 4-3 on the right-hand-side, one can employ mapping scan of an area instead of a single line, resulting in 3-dimensional data of the obtained new layer. It should be mentioned that this method takes a certain amount of time complete a full mapping of the build platforms layer making it not usable for the time critical Deep Dip method. Because of that, the mapping mode will only be used in the beginning of a measurement and in the end, when a new liquid layer has already settled and only a minimal motion is existing.

#### 4.1.2. Data Post Processing and Extraction

This section will give a brief introduction about the data extraction and post process for the layer measurements. As described in 4.1.1 the confocal sensor is moved in the x-y-plane to enable the layer measurements. Here the system is mapping the build platform or linearly scans the liquid surface while the build platform is performing the Deep Dip procedure. Furthermore, the system is set up so that for each movement of the x- and y-stage, the confocal sensor is measuring data and writes this data in a separate file. Therefore, for each movement from the GCode, a separate measurement file exists with an ID. This ID matches the corresponding GCode command ID. Consequently, each measurement file with the raw data is imported and will be matched with its associated axis movement from the GCode file. Additionally, independent of what measurement mode was executed (mapping or line scan method) any data extracted from the confocal sensor must be post-processed before analysed since the raw data from the sensor can contain misleading sensor output data, which can lead to a false analysis. An example for a single raw data can be seen here in figure 4-4 where the upper layer part is measured false.

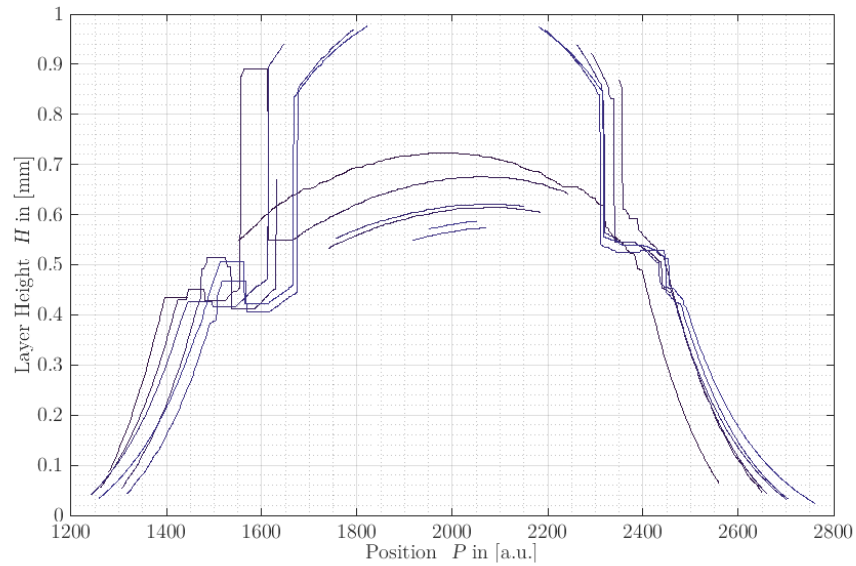


*Figure 4-4: Showing the first scans of a line measurement where the layer surface is shown. The Y-axis displays the layer height and the x-axis the scan position.*

The measured layer is fragmented, since some part of the layer distance exceeds the 1 mm measurement range of the sensor. Therefore, the sensor delivers wrong data of the upper surface which are placed at a wrong height of 0.5 mm to 0.7 mm which can be seen from position 1600 to 2300. This data must be filtered out if possible. Additionally, the sensor drives over the liquid photopolymer layer from two sides as it was explained earlier in section 4.1.1 resulting in flipped line scans, which can be seen in Figure 4-5.

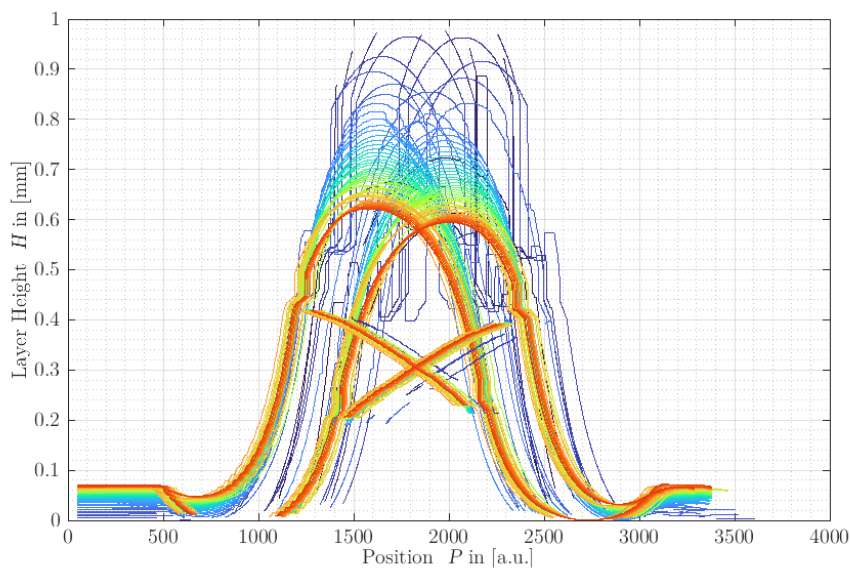


*Figure 4-5: Showing a layer measurement where the layers appear flipped horizontally.*

From Figure 4-5 it can be observed that some data is horizontally flipped resulting from two different movement directions when scanning. Here the first scans are shown in blue colour and the last scans are shown in red colour. Therefore, every second scan must be flipped back to align the data, however an additional shift is therefore introduced and can be seen in Figure 4-6 below.

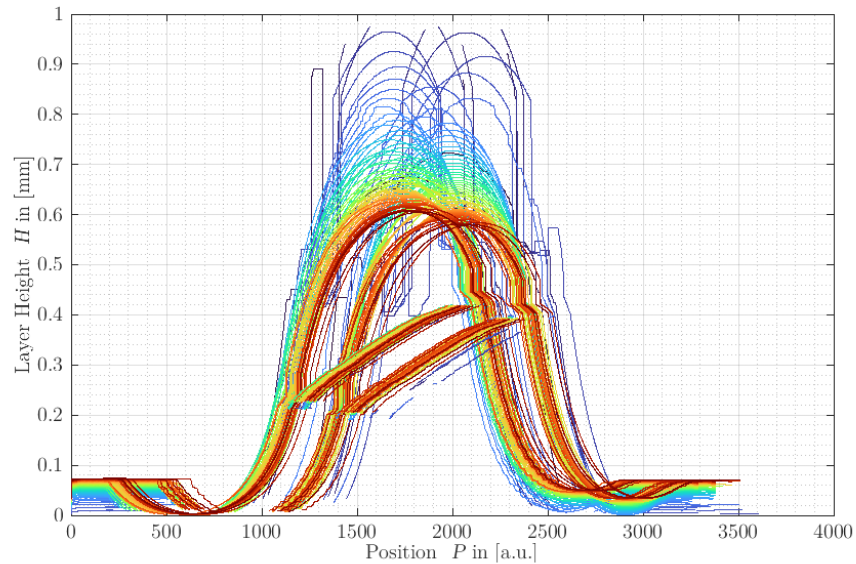


*Figure 4-6: Showing the flipped data, which exhibits a undefined shift in the data.*

From Figure 4-6 the shift in the re-flipped data can be observed. Additionally, in the upper part line measurements can be seen which are similar to a gaussian bell-curve and beneath the build platform can be seen. Here each colour corresponds to a specific line scan where the first line scans have a blue colour and the last lines scan have a red colour. The build platform can only be visible in the centre since the line scans length is higher longer than the build platform width as it was also discussed in 4.1.1. Furthermore, the upper layer declines in height while the build platform stays mostly constant regarding its height and position since it is not moved during scanning. To correct for the shifting, an additional reshifting algorithm was developed. During the shifting process, the algorithm searches for build platform data which can be seen in Figure 4-6 from above. The build platform data acts as a reference since its data remains primarily constant during the Deep Dip process. Therefore, all datasets are shifted until the build platform

data is aligned regarding its position from all scans. A fully shifted dataset can be seen in Figure 4-7.

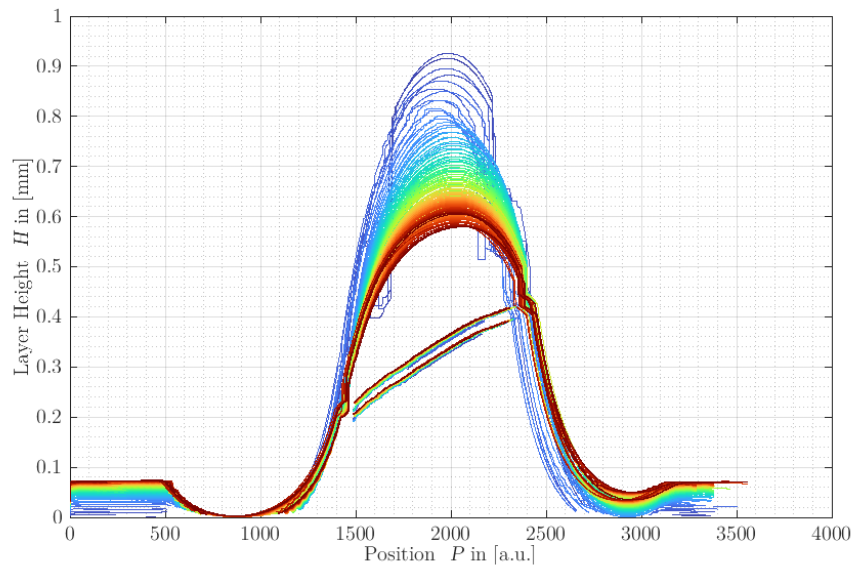


Figure 4-7: The final dataset after filtering, flipping, and shifting the layer surface and build platform data.

From Figure 4-7 it can be observed that after the shifting process the build platform aligns now regarding the position  $P$ . However, some artifacts can still be observed from the filtering process. Additionally, it should be stated, that the employed shifting algorithm can fail if no build platform data is available or disturbed, leading to a wrong shift. After the shifting process and matching process, the data gets saved in a .mat file as a table where exactly for each scan the movement coordinates are save as well as the raw data and the shifted data. Which can be seen in the following Figure 4-8:

	1		2		3		4		5		6		7		8		9		10	
	CoordsRel		Velocities		WaitTimes		Distance1	Distance2	Thickness	Distance1Shifted	Distance2Shifted	ThicknessShifted					TimeStamp			
94	26	0	0	10	0	3383x1 double	3383x1 double	3383x1 double	3383x1 double	3383x1 double	3383x1 double	3383x1 double	3383x1 double	3383x1 double	3383x1 double	3383x1 datetime				
95	-26	0	0	10	0	3561x1 double	3561x1 double	3561x1 double	3561x1 double	3561x1 double	3561x1 double	3561x1 double	3561x1 double	3561x1 double	3561x1 double	3561x1 datetime				
96	26	0	0	10	0	3472x1 double	3472x1 double	3472x1 double	3472x1 double	3472x1 double	3472x1 double	3472x1 double	3472x1 double	3472x1 double	3472x1 double	3472x1 datetime				
97	-26	0	0	10	0	3561x1 double	3561x1 double	3561x1 double	3561x1 double	3561x1 double	3561x1 double	3561x1 double	3561x1 double	3561x1 double	3561x1 double	3561x1 datetime				
98	26	0	0	10	0	3561x1 double	3561x1 double	3561x1 double	3561x1 double	3561x1 double	3561x1 double	3561x1 double	3561x1 double	3561x1 double	3561x1 double	3561x1 datetime				
99	-26	0	0	10	0	3472x1 double	3472x1 double	3472x1 double	3472x1 double	3472x1 double	3472x1 double	3472x1 double	3472x1 double	3472x1 double	3472x1 double	3472x1 datetime				
100	26	0	0	10	0	3650x1 double	3650x1 double	3650x1 double	3650x1 double	3650x1 double	3650x1 double	3650x1 double	3650x1 double	3650x1 double	3650x1 double	3650x1 datetime				
101	-26	0	0	10	0	3383x1 double	3383x1 double	3383x1 double	3383x1 double	3383x1 double	3383x1 double	3383x1 double	3383x1 double	3383x1 double	3383x1 double	3383x1 datetime				
102	26	0	0	10	0	3561x1 double	3561x1 double	3561x1 double	3561x1 double	3561x1 double	3561x1 double	3561x1 double	3561x1 double	3561x1 double	3561x1 double	3561x1 datetime				

Figure 4-8: Showing the saved coordinates, raw data and post processed data.

In Figure 4-8 the table format of the post processed data can be seen, velocities and wait times of a path are saved as well as the raw data of the layers in the “Distance1”, “Distance2” and “Thickness” rows. Here each entry contains a vector from a scan. Additionally, the table contains the post processed version of the data as “Disance1Shifted”, “Disatnce2Shifted” and “Thickness Shifted” and the timestamps.

After the shifting process, additional data from the environment temperature, pressure and humidity logging is added to the data. Here the timestamp from the environment log is matched with the timestamp of the layer measurement data. As a result, environmental data for each conducted scan, a movement exists and can later be correlated to the measured layer data. Figure 4-9 shows the pipeline of the data post processing.



*Figure 4-9: Overview of the data post-processing.*

After the post processing, the analysis of the measurements is done with the following procedure: To compute the maximum layer height  $H_{max}$ , an algorithm measures the obtained layer height from the shifted layer dataset by finding the middle point in the build platform, since the maximum layer height is mostly forming above the middle centre point of the build platform and additionally the build platform remains constant for each scan which can be seen in Figure 4-10:

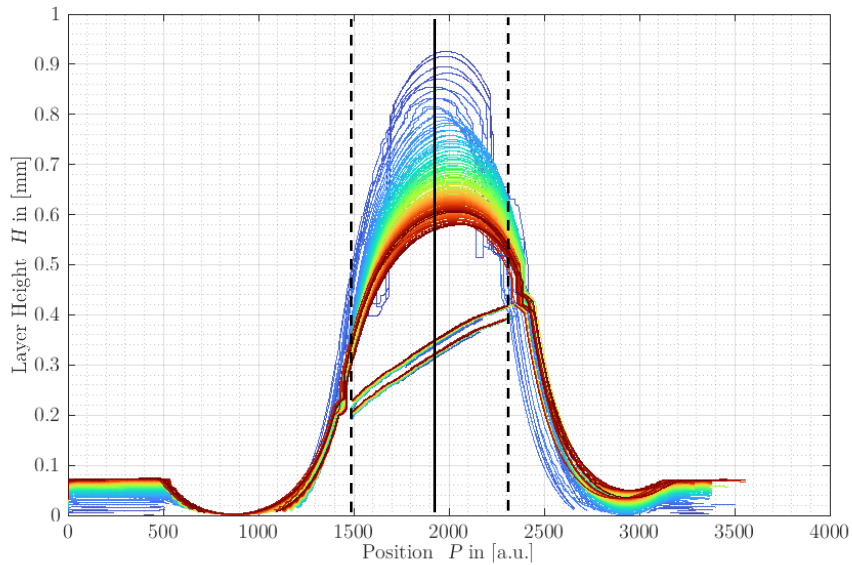


Figure 4-10: Showing the post processed layer measurement, where the middle point of the build platform is marked with a black line and its outer edges are marked with the dashed lines.

As described on the previous page 74 and as it can be seen in Figure 4-10 the algorithm is searching for the centre of the build platform beneath the liquid layer. If the middle point was found, then the algorithm will save the position and moves on to the thickness data as it can be seen in Figure 4-11:

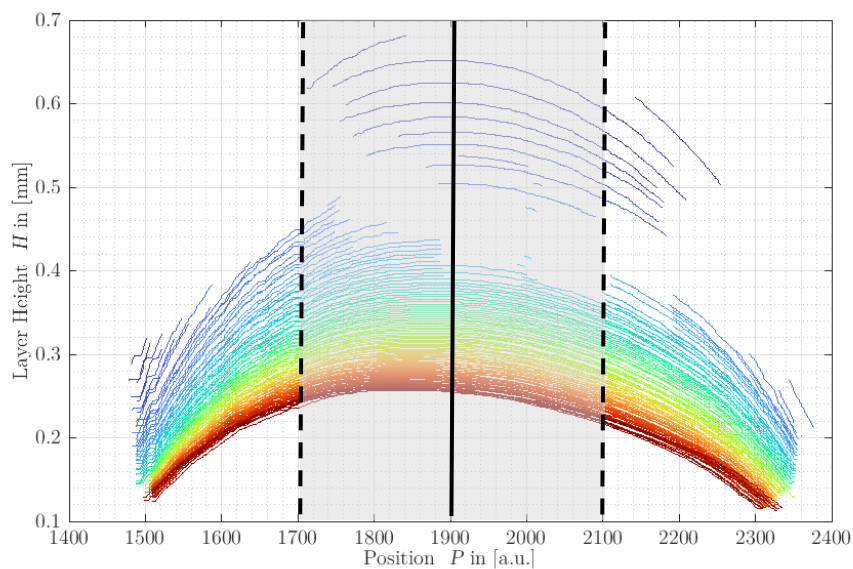


Figure 4-11: Showing the final layer height obtained from the sensor for different positions. The solid black line represents the build platform centre and the dashed lines the margin relative to the centre line defining the grey shaded analysis area.

In Figure 4-11 the layer height above the build platform for each scan can be seen. The black line in the middle represents the centre of the build platform from the algorithm and acts as a reference, from there an area is designated (shaded grey area) in which the algorithm searches for the maximum layer height. The reason for this is, that sometimes some false data can survive the filtering process and if only the MATLAB max-function would be applied to find the maximum layer height, the faulty data would be included leading to a false analysis. Therefore, with this algorithm the important piece of the thickness data is firstly spatially framed and then secondly analysed with the max-function to obtain the maximum layer height. This results in a more robust analysis. It should be mentioned that the max-function is applied after the framing to each scan individually so that the maximum layer height for each scan (or time) can be received and an example for this can be seen in Figure 4-12.

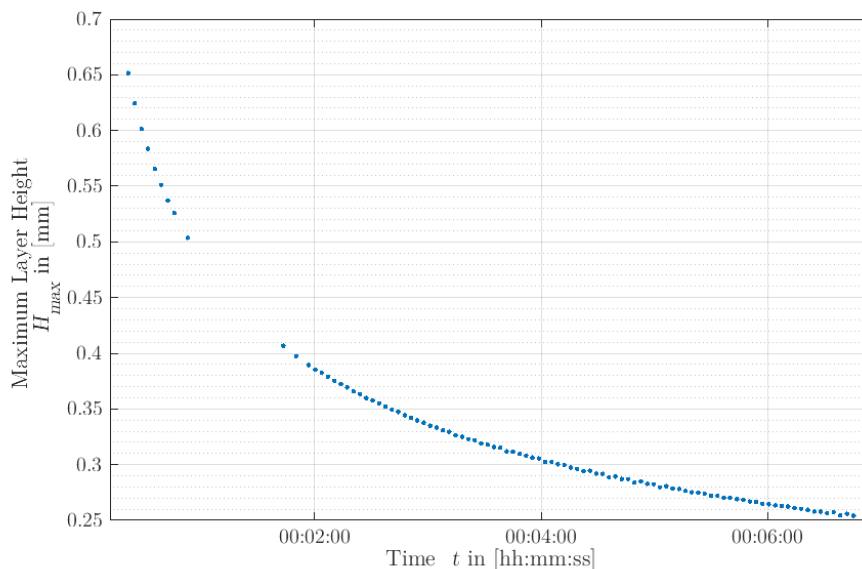


Figure 4-12: Showing the obtained maximum layer height form the analyses algorithm over time.

Here in Figure 4-12 the analysed measurement of the thickness dataset form Figure 4-11 can be seen. According to Figure 4-11 after the first few layers scans the layer thickness could not be measured by the sensor for unknown reason and this can also be observed in Figure 4-11. Regarding the *ROC*, the thickness data from Figure 4-11 is analysed by

applying a curvature-function from Mjaavatten et al. [42] to the layer data vector. The principle of the curvature function can be seen here in be Figure 4-13:

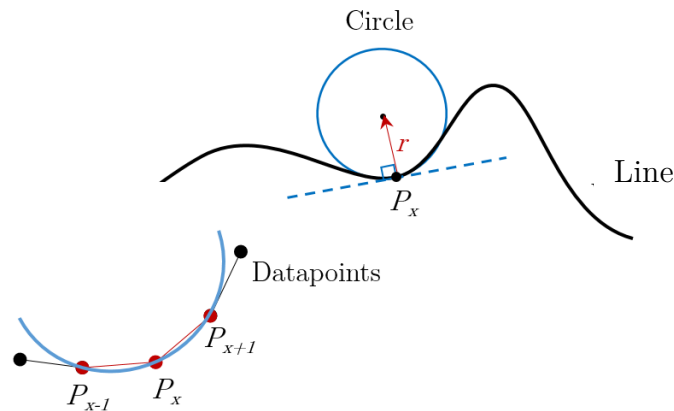


Figure 4-13: The principle of the circle fitting for the ROC analysis.

In Figure 4-13 the black line is a vector and for each point on the line a circle can be attached whose radius matches the curvature of the line and the circle radius must be normal to the tangent of an arbitrary point  $P_x$ . From the circle the radius can be obtained which becomes the *ROC*. Furthermore, this can be done numerically by iterating over each line point  $P_x$  of a vector and fitting a circle which connects all three points from  $P_{x-1}$  to  $P_{x+1}$ . Therefore, the output of the function is a vector containing all *ROC* values for each layer datapoint and this can be seen in Figure 4-14.

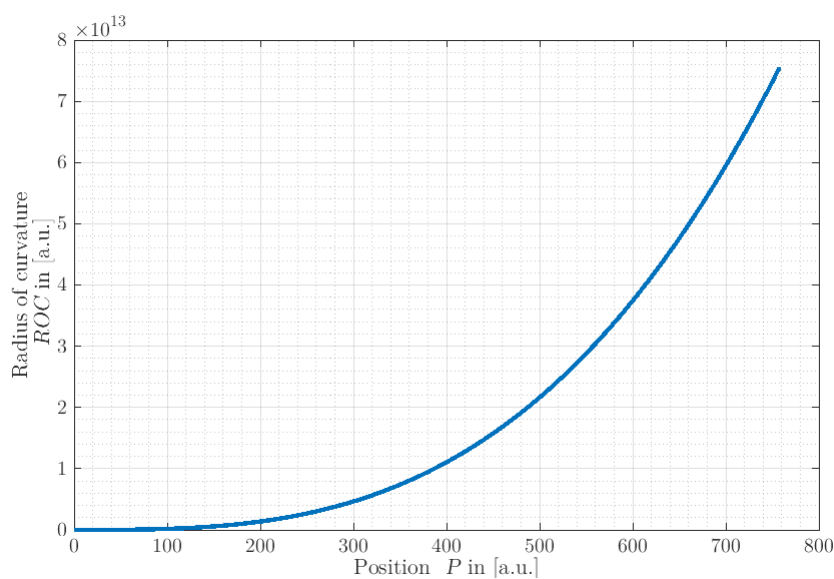
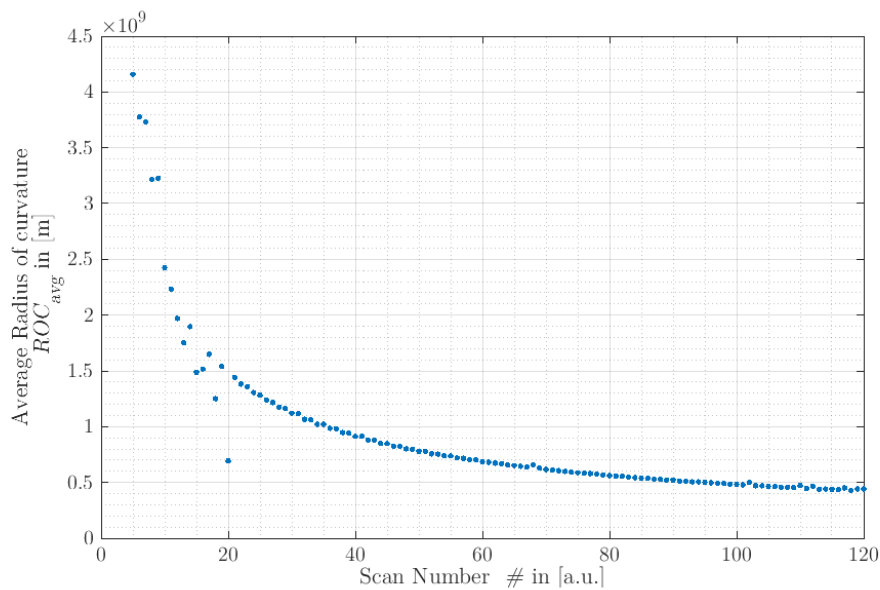


Figure 4-14: The *ROC* vector of a single measured layer.

From Figure 4-14 the resulting  $ROC$  vector is displayed for each position additionally the dimension is given in arbitrary units since the function must compute a radius with the dimensionless Position vector  $P$ . To make the analysis of the  $ROC$  simpler for a later stage, the average values of every single  $ROC$  vector for each layer scan is computed and therefore a single average  $ROC$  value can be applied to all scans (time) and it can be seen here in Figure 4-15:



*Figure 4-15: Showing the average  $ROC$  for each scan. (btw this graphic is wrong and I will change it.  $ROC$  Should be increasing)*

In Figure 4-15 the average  $ROC$  for each scan can be seen. Additionally, it can be observed that the  $ROC$  is increasing over time. This can be correlated to the Figure 4-7 where the layer thickness falls and therefore the layer flattens, which increases decreases the  $ROC$ . With this the most important aspects of the data post processing and data extraction were explained an in the upcoming chapter 5, the experiment 1 will be described and the result will be shown and explained.

## 5. Layer Generation with Deep Dip Method

After discussing the experimental setup in chapter 3 and the overall methodology in chapter 4, the first experiment will be described and discussed in this chapter and a motivation and goal for it shall be given in the next subchapter 5.1.

### 5.1. Motivation and Goal

As mentioned in chapter 3, the goal for this experiment is to generate new layers of liquid photopolymers on the build platform for a given set of parameters with the Deep Dip method, that were discussed in chapter 3 and explained in more detail in the beginning of chapter 4. Additionally, the obtained layers regarding the maximum layer height  $H_{max}$  and the average  $ROC$  will be analysed which was also described in 4.1.2. Therefore, the methodology for this first experiment will be discussed in the following subchapter 5.2.

### 5.2. Methodology

For this experiment the influence of various parameters described in the previous section on the layer height and curvature shall be determined. For this, three sets of parameters were chosen as explained before in chapter 4 and their values can be seen here in Table 5-1:

*Table 5-1: Parameter set for the experiment.*

<b>Deep Dip Offset in [<math>\mu\text{m}</math>]</b>	-300	-233	-166	-100	-33	0	33	100	233
<b>Deep Dip Downwards in [<math>\mu\text{m}</math>]</b>	-1500			-2000			-2500		
<b>BP to RV ratio in [a.u.]</b>	0.0852			0.25			0.8		

From Table 5-1 it can be seen that the  $DDO$  is differentiated to 7 different values but in contrast the  $DDD$  and BP to RV ratio were differentiated into only 3 values. The

reason for this is that a small change in the  $DDO$  can significantly influence the obtained layer height and will be investigated in more detail as it was discussed in chapter 4.

Since for this experiment a parameter analysis is conducted all different parameter values will be combined to get all possible combinations. Additionally, for each parameter combination three measurements will be conducted to yield a higher statistical certainty. Furthermore, the execution order of the parameter combinations was randomized for the  $DDO$  values and the decision was made to leave the BP to RV ratio constant at a ratio 0.0852 for the beginning. Additionally, the dataset with the  $DDD$  value with  $-2000 \mu\text{m}$  was executed first followed by the dataset with  $DDD = -1500 \mu\text{m}$  and finally with a  $DDD$  value of  $-2500 \mu\text{m}$ .

The first step in preparation for a measurement was to fill the resin vat with the PR48 photopolymer. It is only important that liquid photopolymer level is high enough, so that the build platform has enough room for movement above the resin vat in z-direction. In the second step, an appropriate distance between the confocal sensor and the build platform must be set up. For this, the confocal sensor drives to a fixed position. From there, the build platform which is initially at the homing position of the z-stage is raised until a signal of the confocal sensor appears on the IFC2461 measurement software. The ideal position for a measurement is reached when the build platform distance to the sensor is around 0.7 mm. For this, the sensor position was controlled manually with the developed graphical user interface from 3.3. After the distance is set, the levelling of the build platform relative to the liquid resin surface will be executed.

Since no fixed liquid polymer height is set up, a proper start position must be found. For this reason, the build platform must be levelled in a consistent manner relative to the liquid photopolymer surface. Therefore, the confocal sensor is used and a GCode file was written, which lets the confocal sensor drive from one side to another side of the resin vat along the y-axis in 24 cycles. Since each cycle takes around 4 s time and involves two movements, the entire levelling process takes around 3.2 minutes. In this time, the

build platform can make contact to the liquid photopolymer layer and the liquid can settle in. While in motion, the confocal sensor will not move in z-direction to maintain the optimal distance to the build platform which was set up before and the sensor measures the distance of the build platform and the liquid photopolymer surface. In the IFC2461 software, a signal will appear which is used to control the levelling process. Furthermore, the peak-to-peak metric of the software is used to set up the levelling position properly. Since the liquid photopolymer surface is not entirely flat and will always exhibit a curvature as well as the build platform is skewed in y-direction and x-direction, one must decide a for metric when levelling. For a consistent levelling, a peak-to-peak signal of 200  $\mu\text{m}$  is set. This means, that the distance from the lowest point in the scanning signal to the highest point in the signal must be 200  $\mu\text{m}$ . In the levelling process, while the sensor is moving, the resin vat is raised manually by translating the OWIS stage, which is attached to the elevator. The elevator is raised until the liquid photopolymer contacts the build platform from beneath and the peak-to-peak value is exactly 200  $\mu\text{m}$ . In the signal, the build platform can clearly be distinguished from the liquid photopolymer surface. A typical levelling measurement can be seen here Figure 5-1.

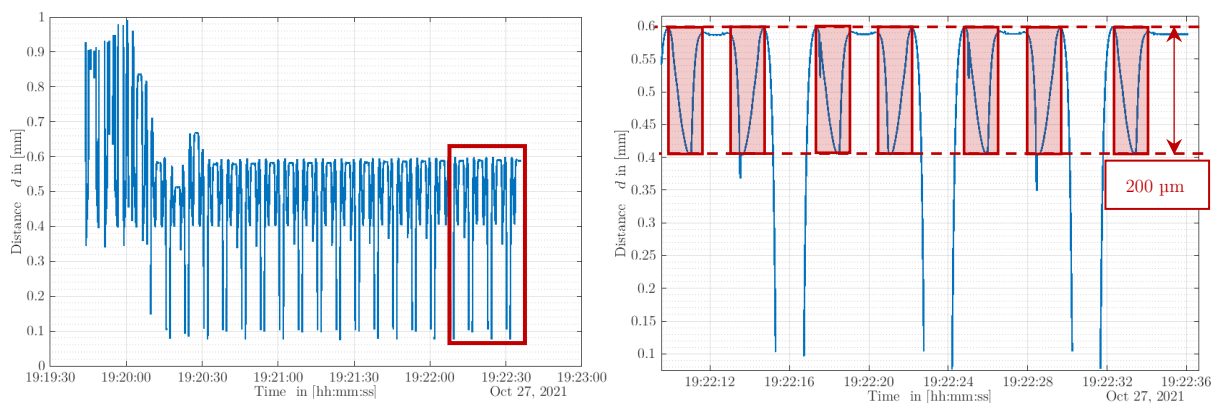


*Figure 5-1: A levelling measurement, where the peak-to-peak value of 200  $\mu\text{m}$  is set ignoring artifacts in the measurement.*

From Figure 5-1 the on the left-hand side a typical levelling measurement including multiple scans of the build platform and the liquid photopolymer surface. On the right-hand side a magnification of the last few scans can be observed. Here the upper bound and lower bound of the multiplatform and resin level are marked with the dashed lines, exhibiting peak-to-peak values of around 200  $\mu\text{m}$ . The build platform is marked with the red shaded areas. In between those areas, the liquid surface was measured and can be seen.

After the levelling process the actual measurement can take place. As described earlier in 4.1.1, each measurement is compromised out of three parts. In part one, a mapping of the build platform and the resin surface will be conducted. Here the build platform is in a levelled state relative to the liquid photopolymer. Therefore, the build platform can be mapped before any layer generation and acting as a reference for later analysis. In the mapping process, the confocal sensor scans a path of 1.5 mm in y-direction and the x-direction is shifted in +0.25 mm until the entire tip was scanned.

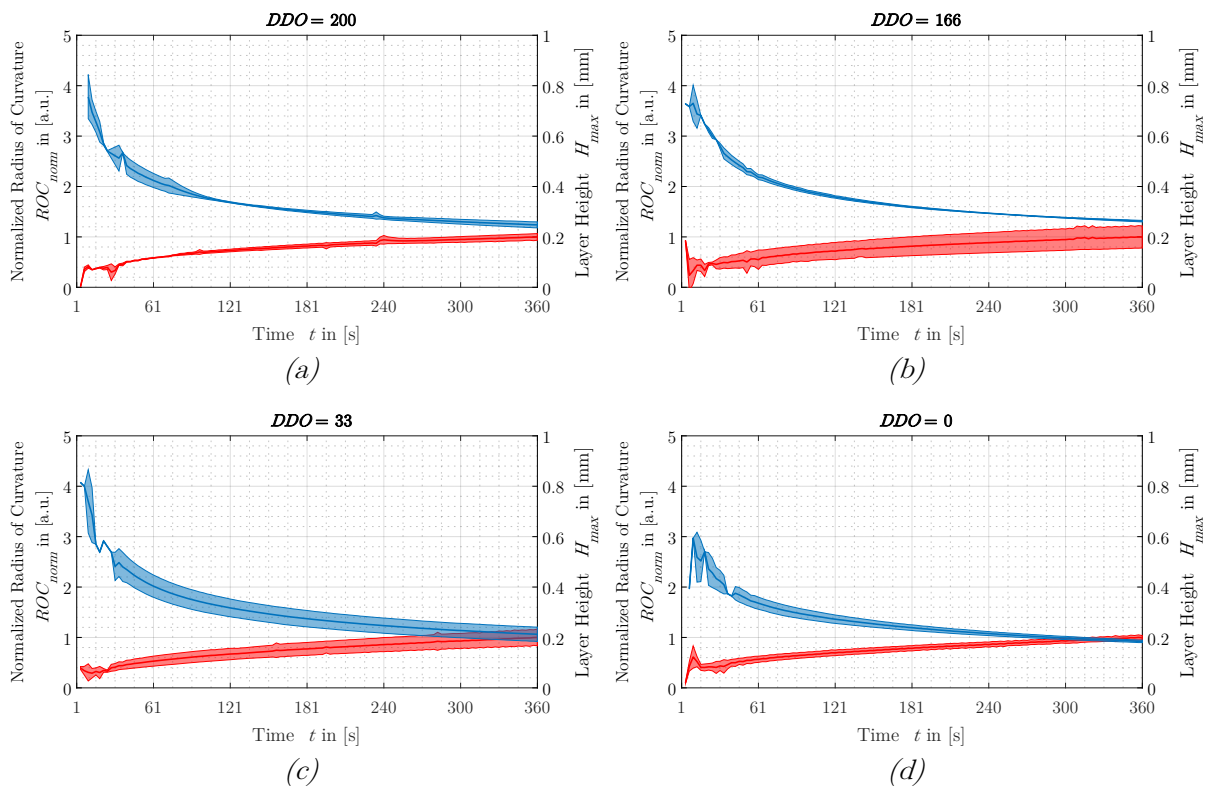
Secondly, the actual generation and scanning of the layers will be conducted. In this part, the build platform will be immersed deeply into the resin vat for around 2 minutes according to the chosen *DDD* value and subsequently be emerged according to the chosen *DDO* value. This is followed by the scanning of the layers in y-direction in 120 cycles. Here the layer height, layer curvature and settling time shall be determined and measured. In the final part, a second mapping of the build platform and layer will be conducted. Here 3-dimensional information of the final layer shall be measured. After each measurement, the build platform was cleaned from the PR48 using a fabric tissue to guarantee the same starting conditions. Besides the measurements a logging device was placed near the setup, to log the pressure, humidity, and temperature.

### 5.3. Results

The experimental results can be seen in the following figures and the dataset has a BP to RV ratio of 0.0852. They show the individual measured maximum layer heights  $H_{max}$  in blue colour and the normalized radius of curvature  $ROC_{norm}$  in red colour over time for each  $DDO$  value. Each graph shows the standard deviation as a shaded area and the mean values as a solid line.

Figure 5-2 shows the analysed measurement data for  $DDD = -2000 \mu\text{m}$ , Figure 5-3 shows the analysed measurement data for  $DDD = -1500 \mu\text{m}$  and Figure 5-4 shows it for  $DDD = -2500 \mu\text{m}$  ranging from page 84 to 89.

Figure 5-5 on page 90 shows the analysed measurements from Figure 5-2, Figure 5-3 and Figure 5-4 compressed as a surface plot, where the mean values of the  $H_{max}$  normalized and  $ROC_{norm}$  can be seen. The showed results will be discussed in subchapter 0.



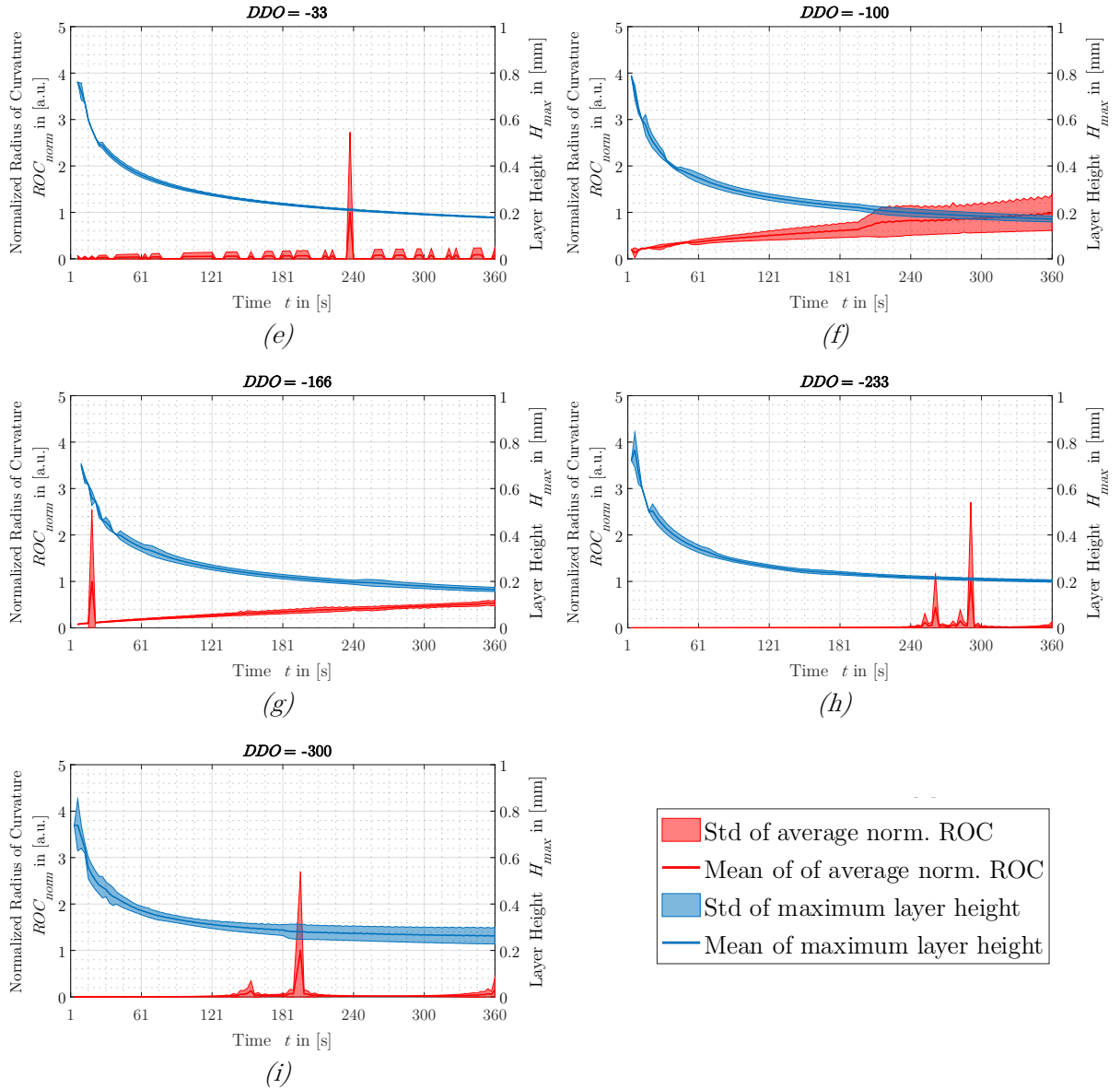
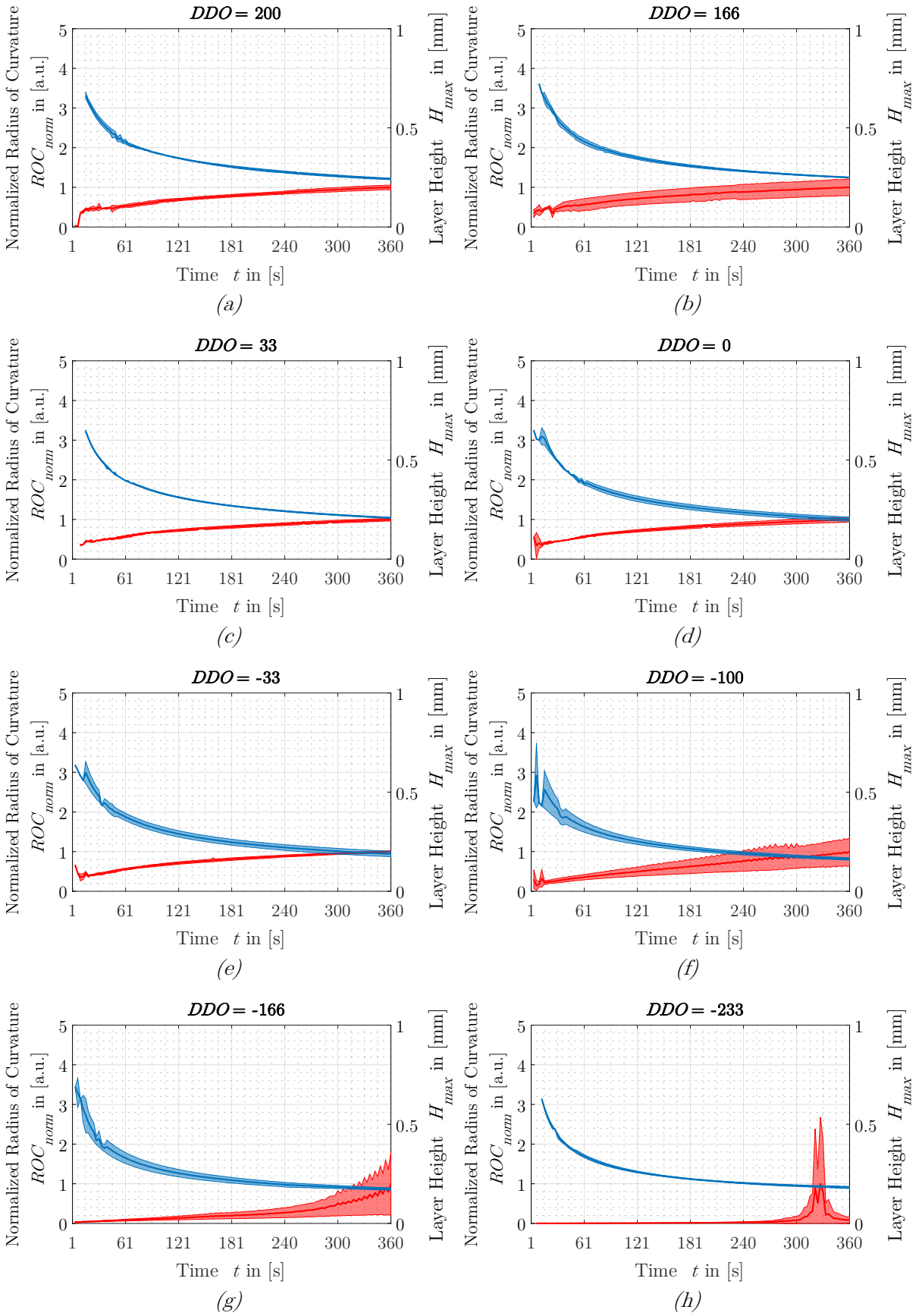


Figure 5-2: Layer measurements showing the mean and standard deviation of  $H_{max}$  (in blue) and of the normalized  $ROC_{norm}$  (in red) for the individual  $DDO$  values,  $DDD = -2000 \mu m$ , BP to  $RV$  ratio = 0.0852.

In Figure 5-2, all maximum layer heights shown an exponential decay. Furthermore, the first few scans cannot be seen in the measurements since the starting layers are outside the measurement range of the sensor. The obtained maximum layer heights start from around 0.8 mm and decrease to around 0.2 mm, where specifically the positive  $DDO$  values yield layer thicknesses over 200  $\mu m$  and the negative  $DDO$  values layer thicknesses up to 180  $\mu m$ . An exception is the  $DDO$  value, here the layer thickness is above 200  $\mu m$  again. Furthermore, the exponential decay is stopped at (h) and (i), since no further

significant decrease of the layer height can be observed, whereas in the other measurement, the decay is still goes on until the last scan. Furthermore, the standard deviation is mostly strong in the beginning of the maximum layer height but is reduced in the later stage of the scanning process, except for measurements (c), (f), (g) and (i). Here the standard deviation is high for the entire measurement.

Regarding the *ROC* for positive *DDO* values it is increasing in a logarithmic manner, but for negative *DDO* values peaks of the *DDO* values appear except for *DDO*-100  $\mu\text{m}$  meaning that flat layers were generated at those points and therefore the standard deviation gets high at those points. Furthermore, for some *DDO* values multiple peaks can be observed, meaning that flat layers can be established at multiple points, which can be seen in (h) and (i).



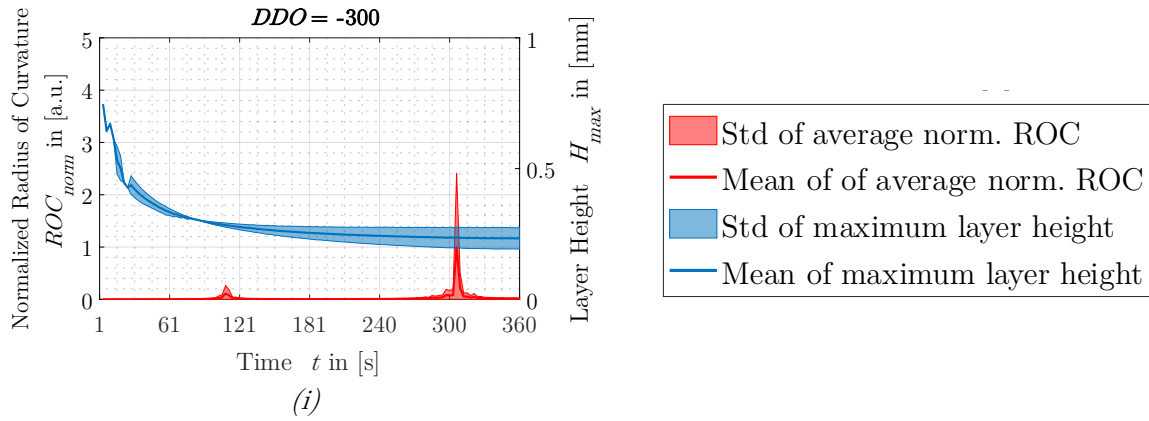
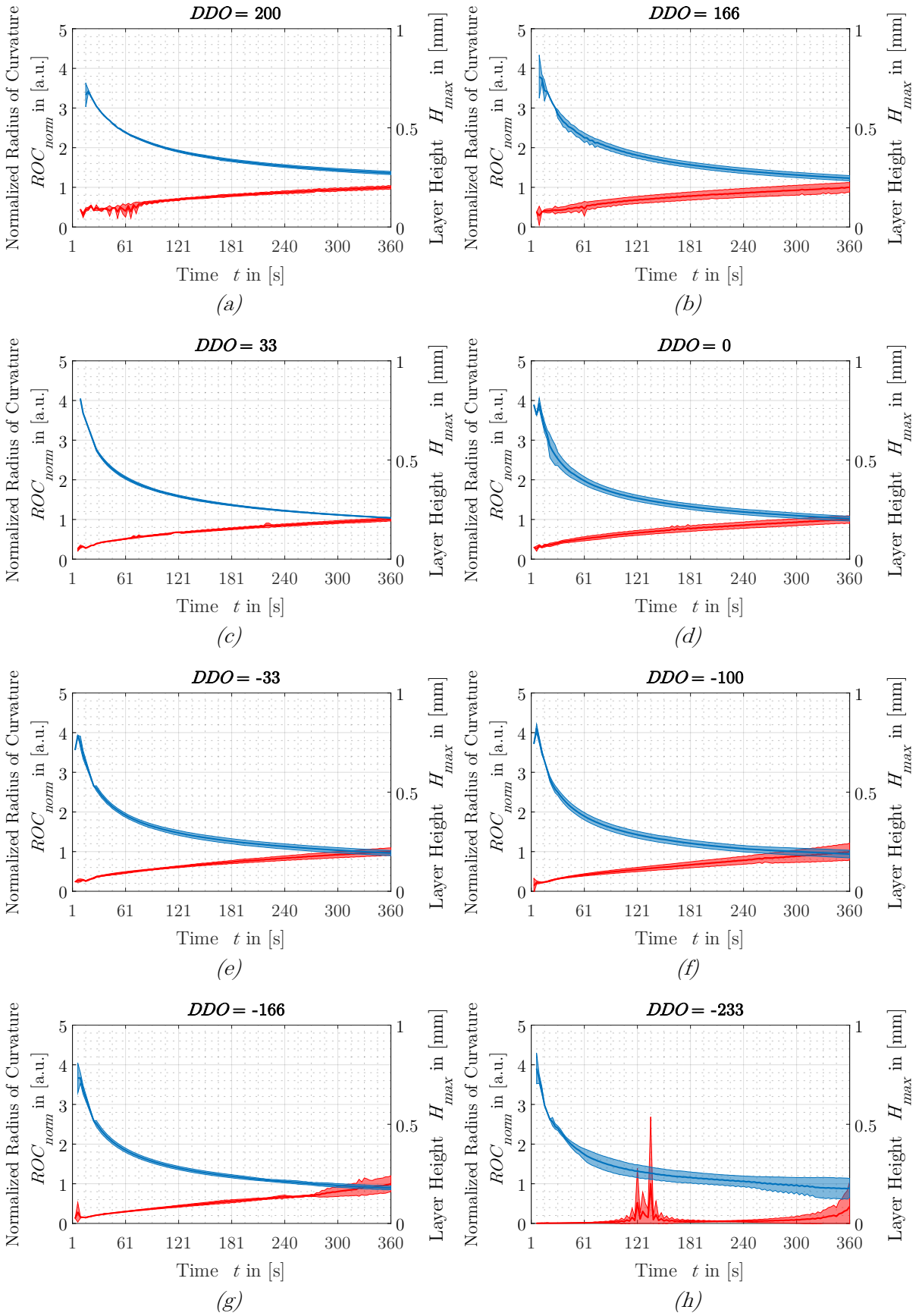


Figure 5-3: Layer measurements showing the mean and standard deviation of  $H_{max}$  (in blue) and of the normalized  $ROC_{norm}$  (in red) for the individual DDO values,  $DDD = -1500 \mu m$ , BP to RV ratio = 0.0852.

In Figure 5-3 in same exponential decay can be observed like in the measurement set before. Additionally, the standard deviation is mostly high in the beginning of a measurement but the reduces to a lower value when the data goes to an end which can be seen in (a), (b), (d), (e), (f), (g) except for (i) where the standard deviation is constantly high and in (c), (h) where the standard deviation was low through the entire measurement.

With respect to the  $ROC$ , it is increasing in a logarithmical manner like in Figure 5-2. Furthermore, only significant peak can be observed for (h) and (i). In (i) two  $ROC$  peaks can be observed. Concerning the to the standard deviation in Figure 5-3, it can be observed that it remains relatively low for (a), (c), (d) and (e), whereas it is high for (b), (f) and (g) for the entire measurement.



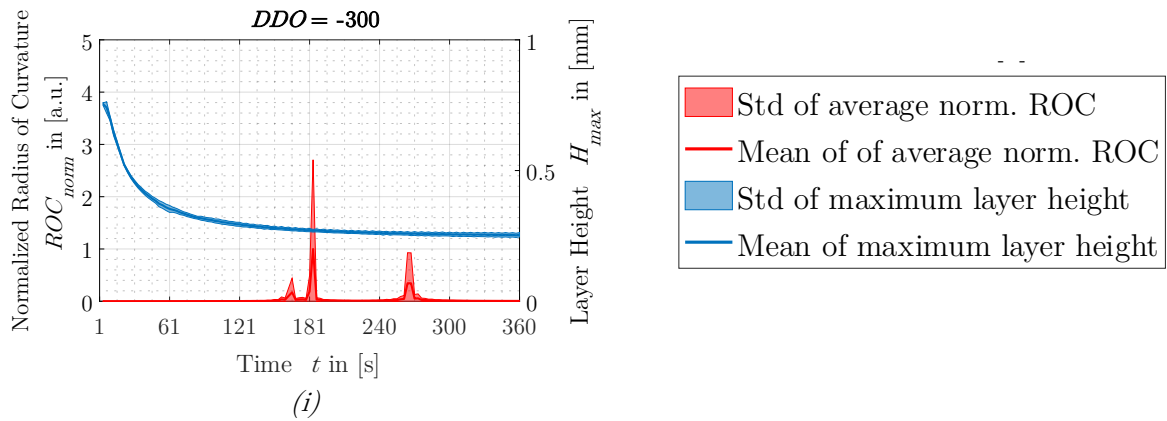


Figure 5-4: Layer measurements showing the mean and standard deviation of  $H_{max}$  (in blue) and of the normalized  $ROC_{norm}$  (in red) for the individual DDO values,  $DDD = -2500 \mu\text{m}$ , BP to RV ratio = 0.0852.

Like in Figure 5-2 and Figure 5-3 before, the characteristically exponential decay can be seen in the maximum layer height for each individual measurement. Again, the first scans of the layer height cannot be seen since the sensor is outside the measurement range. Furthermore, the standard deviation of the maximum layer height is in this dataset less prominent in the beginning of a measurement but increases slightly more throughout the end of a measurement. Like before, the exponential decay is stopped in (i), since the layer height does not change significantly after around 240 s.

About  $ROC$ , the same logarithmic increase can be observed from (a) to (g) and again only in (h) and (i) significant peaks can be seen.

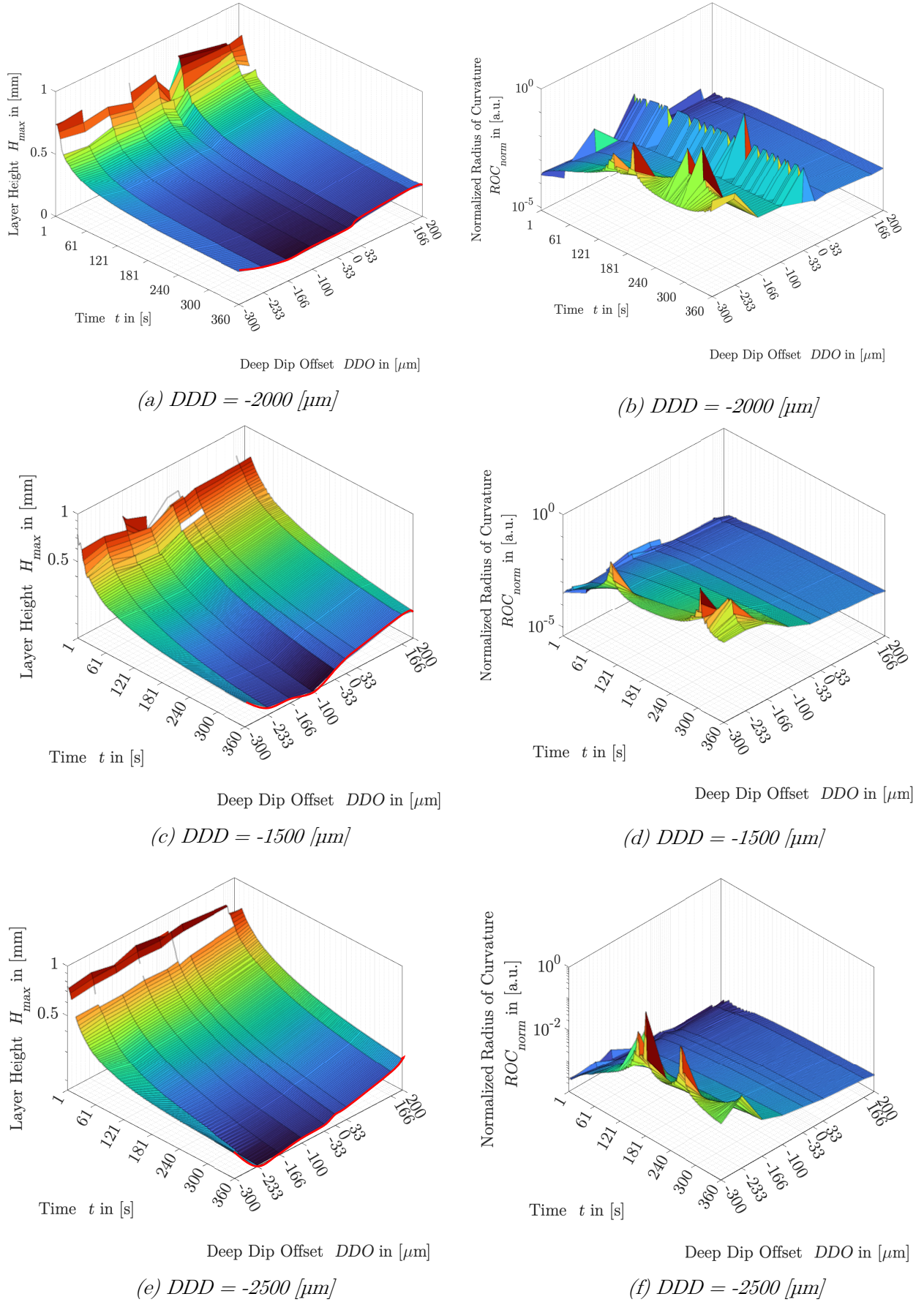


Figure 5-5: The mean values of the  $H_{max}$  on the right-hand side and the mean values for  $ROC_{norm}$  on the left-hand side for each DDO value and DDD value. BP to RV ratio was 0.0852

From Figure 5-5 is used as a direct comparison of the obtained layer height and  $ROC$  for each  $DDO$  value between the 3  $DDD$  datasets and represent the same mean values like they were described before in Figure 5-2, Figure 5-3 and Figure 5-4.

Again, it can be seen in the left-hand side regarding the maximum layer height, that each measurement has in the beginning the characteristically exponential decay. The first few measurement points are not existing because the layers were outside the actual measurement range. Furthermore, we can see, that the exponential decrease for each dataset is influenced by the used  $DDO$  parameter. Here for positive  $DDO$  values like +200  $\mu\text{m}$  and +166  $\mu\text{m}$  yield a higher maximum layer height as  $DDO$  values from 0  $\mu\text{m}$  to -233  $\mu\text{m}$ . Subsequently this trend is reversed when even lower  $DDO$  values like -300  $\mu\text{m}$  are set, here the maximum layer height is increasing again.

Furthermore, the minimal layer height obtained is different for changed  $DDD$  values. The minimal layer height for each  $DDD$  set can be seen in the following table:

*Table 5-2: Smallest obtained layer height and corresponding  $DDO$  values for all  $DDD$  datasets.*

$DDD$ in [ $\mu\text{m}$ ]	-1500	-2000	-2500
$DDO$ in [ $\mu\text{m}$ ]	-100	-166	-233
$\min(H_{max})$ mm	0.1632	0.1652	0.1786

Table 5-2 includes the minimal layer height for each  $DDD$  and  $DDO$  value. The lowest minimal layer height can be obtained with the  $DDD$  value of -1500  $\mu\text{m}$  and for a  $DDO$  value of -100  $\mu\text{m}$ . It can be stated that the minimal layer height increased with decreasing  $DDD$  values. The  $DDO$  values for the minimal layer thickness is shifted from -100  $\mu\text{m}$  to -233  $\mu\text{m}$  for decreasing  $DDD$  values. With reference to the  $ROC$  in the right-hand side of Figure 5-5, the  $ROC$  exhibits the same characteristic logarithmic curve for all 3  $DDD$  values. Furthermore, the  $ROC$  is showing clearly multiple peaks for the  $DDO$  values of -300  $\mu\text{m}$  and -200  $\mu\text{m}$  and they appear mostly in a time range from 60 s to 360 s.

Interesting here is the peak line for  $DDD = -2000 \mu\text{m}$  at  $DDO = -33 \mu\text{m}$ , which is inherited from wrong measurement data.

#### 5.4. Discussion

The results from subchapter 5.3 shall now be discussed. The individual measurements From Figure 5-2, Figure 5-3, Figure 5-4 and Figure 5-5 (left-hand) side show that the generated liquid layers decay exponentially which was expected as this was observed from W. Tan. et al. in 2.2.2. It can also be seen that the obtained layer heights in these experiments are significant higher compared to W. Tan e.t al. simulations which was expected since his simulations used lower viscous liquids. This results also in much longer settling times for the liquid layers in this experiment than in the simulations. Coming back to the layer heights, it can be shown that an exponential decay results from the drain of the liquid photopolymer from the top of the build platform to the liquid bulk below or the next the build platform. An example for this can be seen in the following Figure 5-6.

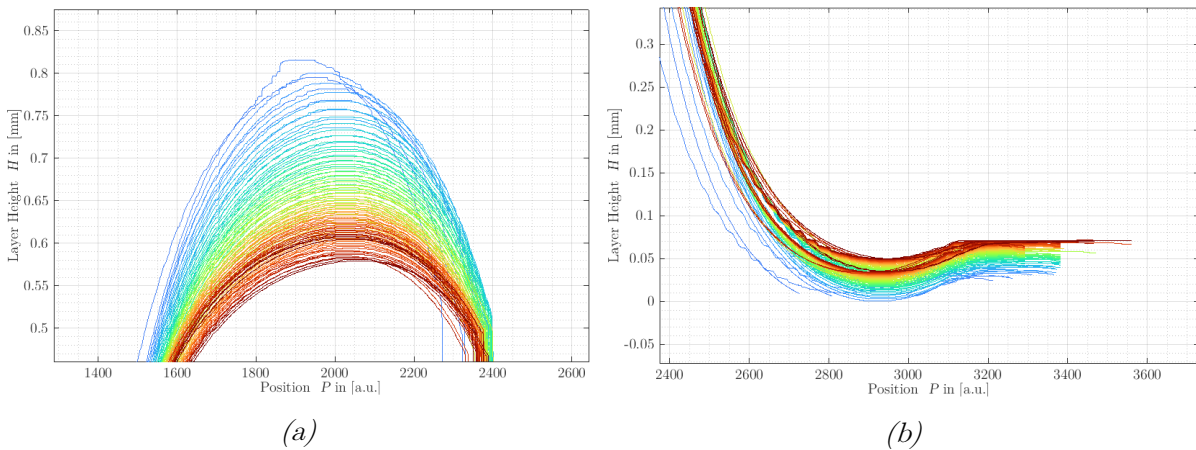
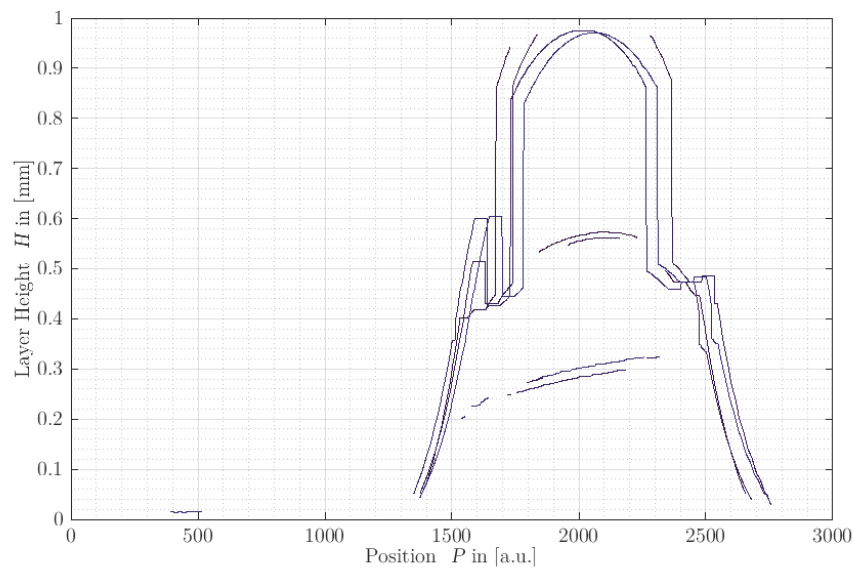


Figure 5-6: Showing the decay in layer height in the upper part of the layer measurement (a) and showing the increase in surface height in the lower part of the measurement (b).

Here in Figure 5-6 a measurement for the parameters  $DDD = -2500 \mu\text{m}$  and  $DDO = 166 \mu\text{m}$  is shown. The first scans are marked in blue colour while later scans

are marked in red colour and the top of the liquid layer is decreasing, while at the same time overall fill stand is increasing and as a result the liquid must flow away from the build platform decreasing the volume on top of it and therefore decreasing the maximum layer height.

From Figure 5-2, Figure 5-3 and Figure 5-4 it can be seen that the standard deviation is mostly in the beginning of a measurement. The reason for this is, that the first layers are out of range for the sensor and cannot be measured. Additionally, if the first layers are too thick, then the build platform cannot be measured and therefore the reshifting of the layers from the algorithm described in 4.1.2 fails. This results in partially wrong analyses data of the maximum layer height and *ROC*. An example for this can be seen in Figure 5-7 below.



*Figure 5-7: Measurements with wrong readings in the beginning regarding upper layer and lower build platform data. Here scan 1 to 4 of the measurement is shown.*

From Figure 5-7 the upper layer yields wrong sensor readings. Furthermore, the build platform data below the layer data is fragmented, which can lead to failed data shifting contributing to a wrong analysis. From figure 5-5 on the left-hand side the final scan for each *DDO* value is marked as a red line and those final scans were extracted for a direct comparison and can be seen here in

Figure 5-8 below.

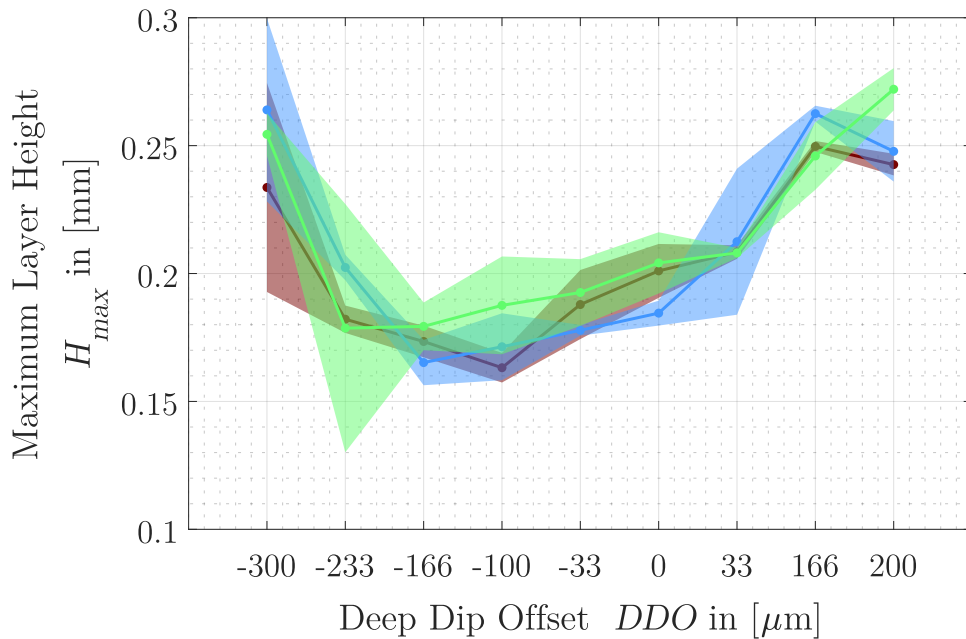


Figure 5-8: Showing the maximum layer height for the last scan for each  $DDO$  value.

Here in Figure 5-8 the final layer thicknesses can be seen for all three  $DDD$  datasets. The final layer thickness is changing depending on the used  $DDO$  values. For a  $DDD = -2500 \mu\text{m}$  the lowest layer height is at  $DDO = -233 \mu\text{m}$ , for a  $DDD = -2000 \mu\text{m}$  it is at  $DDO = -166 \mu\text{m}$  and for a  $DDD = -1500 \mu\text{m}$  it is at  $DDO = -100 \mu\text{m}$ . Therefore, the spots for a minimal layer thickness are shifted towards lower  $DDO$  values which can be seen again in the following Figure 5-9 below.

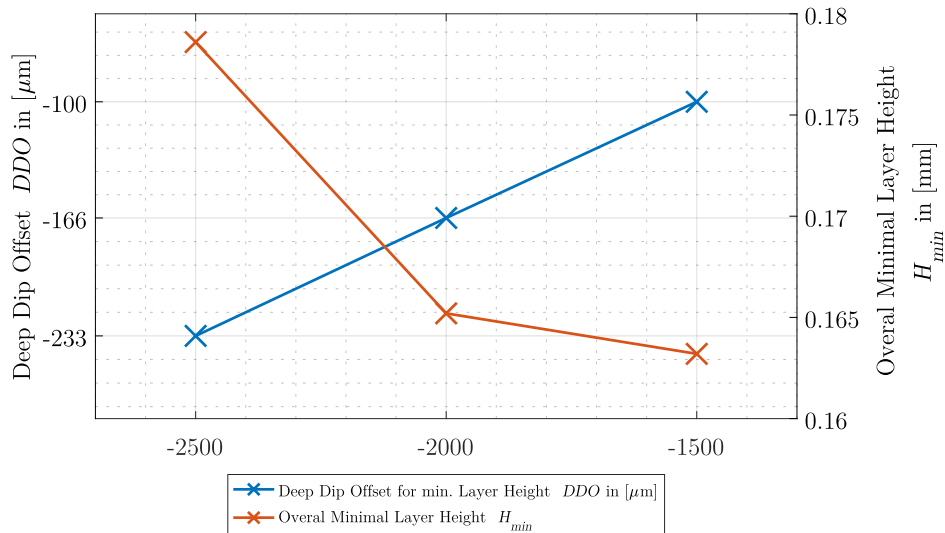


Figure 5-9: Showing the dependency of the minimal layer thickness and the corresponding DDO values in dependency on the DDD values

From Figure 5-9 a linear dependency can be seen for a change in  $DDO$  values for each minimal obtained layer height for each  $DDD$  value and that a non-linear dependency on the minimal obtained layer thickness is existing. Therefore, a change in  $DDD$  values does not change the minimal obtained layer thickness itself but rather the  $DDO$  values where those minimal obtained layer points appear.

Going back to Figure 5-8 the last line scans follow characteristic “u” shape where for higher  $DDO$  values also a higher maximum layer height was obtained and for  $DDO$  values from 0  $\mu\text{m}$  to -233  $\mu\text{m}$  much lower minimal layer height were received. A possible reason for this that different liquid flow rates must exist for each  $DDO$  value, since the  $DDO$  parameter influences the build platform position relative to the initial liquid surface. Therefore, if the build platform is above the initial surface, the liquid photopolymer will try to flow downwards back to the bulk liquid on the build platform sides but is slowed down by the build platform itself since it acts as a barrier. This will result in a decreased fluid flow rate from the build platform to the bulk liquid, decreasing the decay rate of them maximum layer height. In the case for the  $DDO$  value with 0  $\mu\text{m}$ ,

the final build platform will be equal to the initial layer height. Therefore, the liquid can spread sideways on the wetted build platform into the bulk liquid. This scenario maybe best fitted for the Lopez model. When the  $DDO$  values become more negative, the build platforms final position is beneath the initial layer height and therefore the liquid photopolymer can flow to the outside much faster. Here the liquid photopolymer flow rate is increased since the build platform does not act as a barrier that much. Furthermore it was described in Figure 5-2, Figure 5-3 and Figure 5-4 that the exponential decay at  $DDO = -300 \mu\text{m}$  (and sometimes  $-233 \mu\text{m}$ ) is not significant anymore to change the overall layer height after around 240 s. The reason for this is that the build platforms final position is  $-300 \mu\text{m}$  beneath the initial layer height and therefore at a specific point in time the layer cannot become any lower. When describing the observed measurements in chapter 7 with the mathematical model from Lopez et al. from subchapter 2.4. the above stated findings should be incorporated into the model and discussed.

Additionally, from Figure 5-8 the expected final layer thickness does not match the obtained results. For example, for negative  $DDO$  values the Deep Dip method should also yield a minimal layer height of the same values since the build platforms final position is beneath the initial layer height according to the set up  $DDO$  parameter. Therefore, a  $DDO$  of  $-100 \mu\text{m}$  should also yield a final layer thickness of  $-100 \mu\text{m}$ . A reason for this is that the build platform is skewed and not perfectly flat. Additionally, the viscosity in this experiment is high and therefore the build platforms influence in the layer will remain. This influence can be seen in the following Figure 5-10 below.

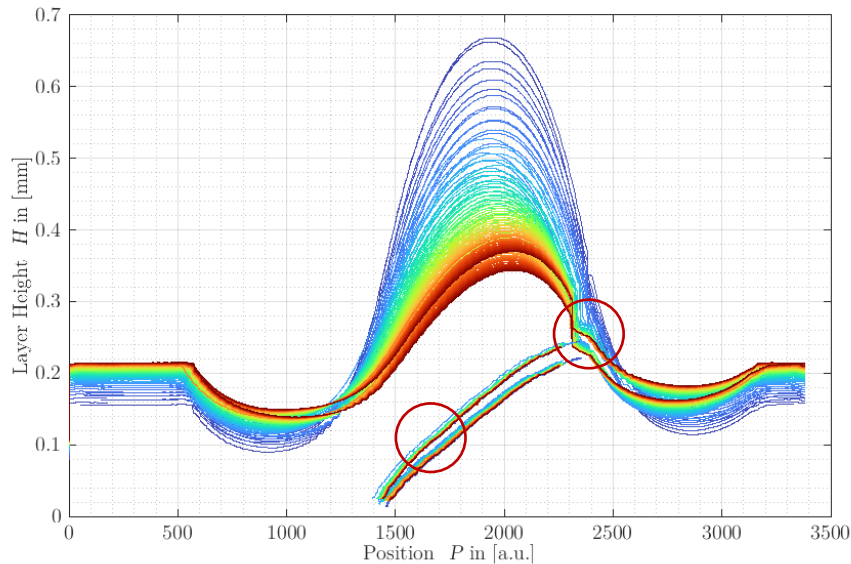


Figure 5-10: Showing a layer measurement with the parameters  $DDD = -2500 \mu\text{m}$  and  $DDO = -100 \mu\text{m}$ .

From Figure 5-10 it can be observed that the right side of the build platform is higher and closer to the actual liquid layer than its left side. This of course influences the layer formation and the layer analyses too. Additionally, as mentioned earlier, the layer decay is still ongoing on the final scan of the measurements (except for the  $DDO = -300 \mu\text{m}$  values), which also can be seen in Figure 5-10. Here for the last scans (red line colour) a convex shaped liquid layer is still existent above the build platform, resulting in a clear height difference between the upper layer and the lower layer on the sides. Therefore, a liquid layer flow to the sides is still possible but is probably restricted by the high viscosity of the liquid. Furthermore, this means that in the obtained last scans the layer heights are not final, and they are still can change, meaning that still more liquid will flow away from the build platform and therefore reducing the obtained maximum layer height. It can be stated that in this conducted experiment the equilibrium of the layers was not reached.

Another thing to point out which can be observed in Figure 5-10 and which is marked by the right circle, is that some part of the layer above the build platform could not be

accurately measured. This phenomenon was discussed before in section 3.4.2. Here the spectral peaks of the confocal sensor are too close to each other and so that only the stronger reflecting build platform distance is measured, resulting in a wrong thickness measurement at those points.

Furthermore, in the circle on the left-hand side in Figure 5-10 the build platform data is marked. Here it can clearly be seen that the position of the build platform is shifted in z-direction. This shift can also be observed in layer data. It can be stated that this shift of around  $20\ \mu\text{m}$  to  $30\ \mu\text{m}$  is caused by the movement of the confocal sensor in z-direction. The origin of this is the 3d printed sensor mount which was also described in subchapter 3.2. When the sensor is moved via the x-y-stages for the scanning process, the optical fibre cable mounted on top of the sensor (which can be seen in Figure 3-5 in subchapter 3.2) is slightly pushing down onto the sensor and sensor mount. This pushing behaviour is different depending on the movement direction and can be shown when selectively plotting measurements from each scan direction, which can be seen here in Figure 5-11:

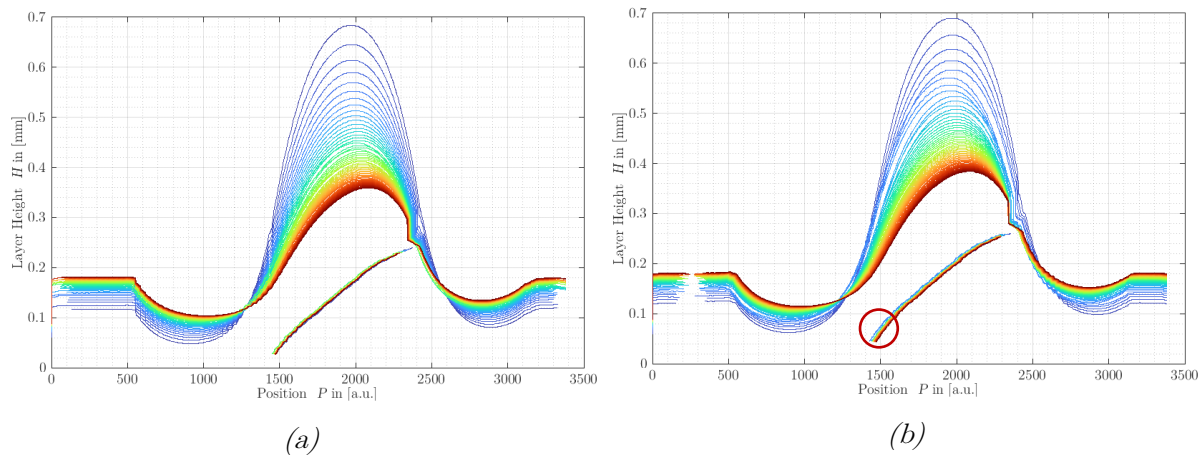


Figure 5-11: Showing the same dataset as in Figure 5-10, but with separated scan directions.

From Figure 5-11 the shift in the data like in Figure 5-10 is not visible anymore after plotting the data from the two scanning directions individually. However, there still can

a shift in the build platform be overserved which is marked with a red circle in (b). A closer inspection reveals the following shift and is shown separately here in Figure 5-12:

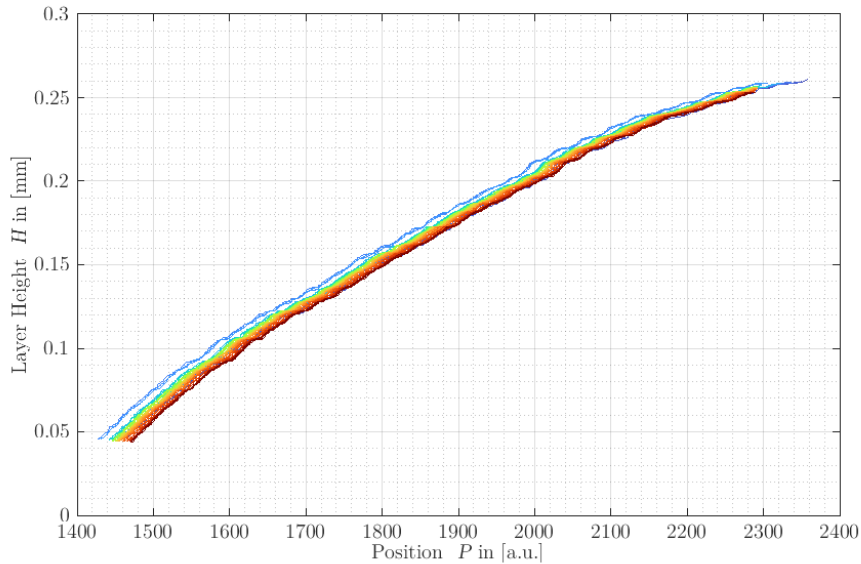


Figure 5-12: Showing the build platform data from Figure 5-11.

In Figure 5-12 the deviation of the build platform can be seen. Here a shift of the build platform surface of up to  $20\ \mu\text{m}$  can be observed. Probably this shift comes from the deviations in the z-stage that were pointed out in a previous validation measurement in section 0. Those deviations can contribute to the received standard deviations in the measurement shown in Figure 5-2, Figure 5-3 and Figure 5-4.

Since the analysis for this experiment is done via the thickness dataset which is simply the difference between the first distance to the second distance, the sensor shift from the weak sensor adapter does not affect the thickness dataset. This can be seen for example in Figure 5-13 below, where no sudden shifts can be observed.

A new observation for the Deep Dip method is the measured *ROC*. Throughout the measurements the *ROC* is increasing logarithmically in the beginning of each measurement, meaning the layers get flatter over time. This makes sense considering that the liquid volume above the build platform is shrinking through the outwards flow

of the photopolymer resulting in a reduced layer height and subsequently leading to a flatter layer. In the Figure 5-5 on the right-hand as well in Figure 5-2, Figure 5-3 and Figure 5-4 significantly high peaks can be observed in the *ROC* signal for negative *DDO* values. When those peaks arise, then the computed *ROC* gets very high meaning that at this point of time, the layer is the flattest. The reason for the peaks appearing only for lower negative *DDO* values like  $-233 \mu\text{m}$  and  $-300 \mu\text{m}$  is that the build platform must be below the initial liquid surface to become flat, since here the influence of the build platform to the upper liquid surface is lower and the liquid can drain faster to the sides and therefore levelling itself out easier. Only under these circumstances a very flat layer can form. Additionally, multiple peaks in the *ROC* measurements can be observed. This is due to the fact, that flat layers are observed at different points in time for each of the three measurements for each parameter set. This indicates that the flat layer generation is not stable regarding the time.

As previously discussed, the obtained layers are influenced by the skewness of the build platform, meaning that the curvature changes its sign and transforms from a convex shape into concave one. Unfortunately, the sign change is not recognized from the curvature algorithm, which was described in 4.1.2. It can be assumed that a sign change of the curvature appears after each peak, there reducing the overall curvature again. Therefore, a flat layer does not stay flat forever. An example for this can be seen in the following Figure 5-13 below.

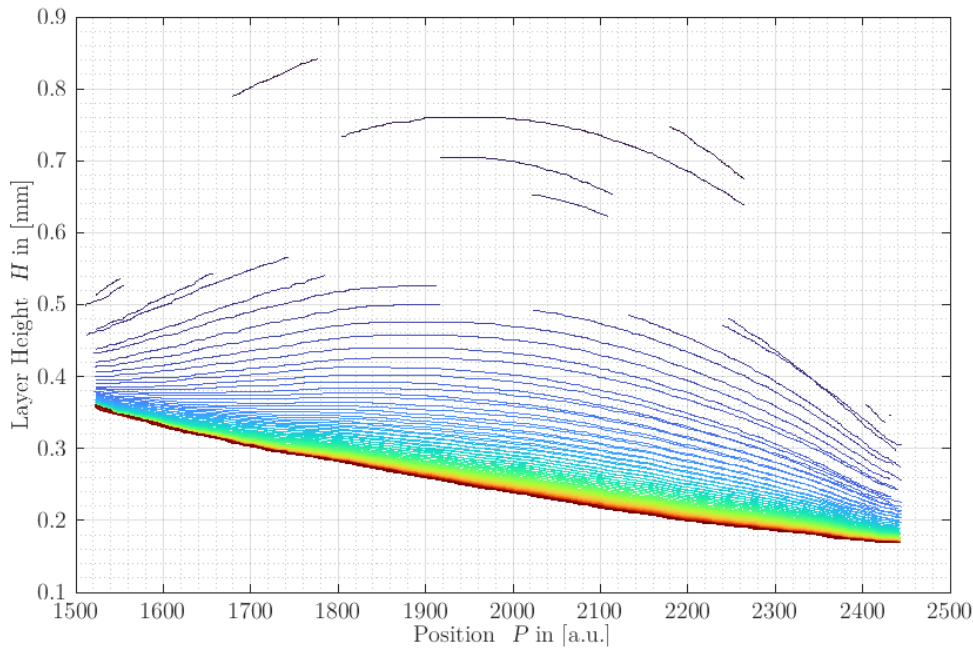


Figure 5-13: The Thickness dataset for a layer measurement is shown for a  $DDD = -2500 \mu\text{m}$  and  $DDO = -300 \mu\text{m}$ .

Here in Figure 5-13 the obtained layer thickness for each scan is shown, where the first scans are displayed in blue colour and the last scans in red colour. The curvature changes its direction through the entire measurement which is in fact caused by the curvature and skewness of the build platform which was shown before in Figure 5-10.

Regarding the  $ROC$  from Figure 5-5 on the right-hand and in Figure 5-2 in (e) for a  $DDD = -2000 \mu\text{m}$  and  $DDO = -33 \mu\text{m}$  it can be observed that the  $ROC$  is abnormally high and doesn't follow exactly the characteristically logarithmic behaviour. This is due a failure of the  $ROC$  algorithm and cannot be explained since the obtained layers are not disturbed by any means.

Again, concerning the  $DDD$  comparison in Figure 5-5 on the left-hand side it can be observed that layer height values are slightly different when comparing the 3 datasets. This can best be investigated when "slicing" through the diagrams on the left-hand side in Figure 5-5 and comparing the slices. This can be seen in the following Figure 5-14 below.

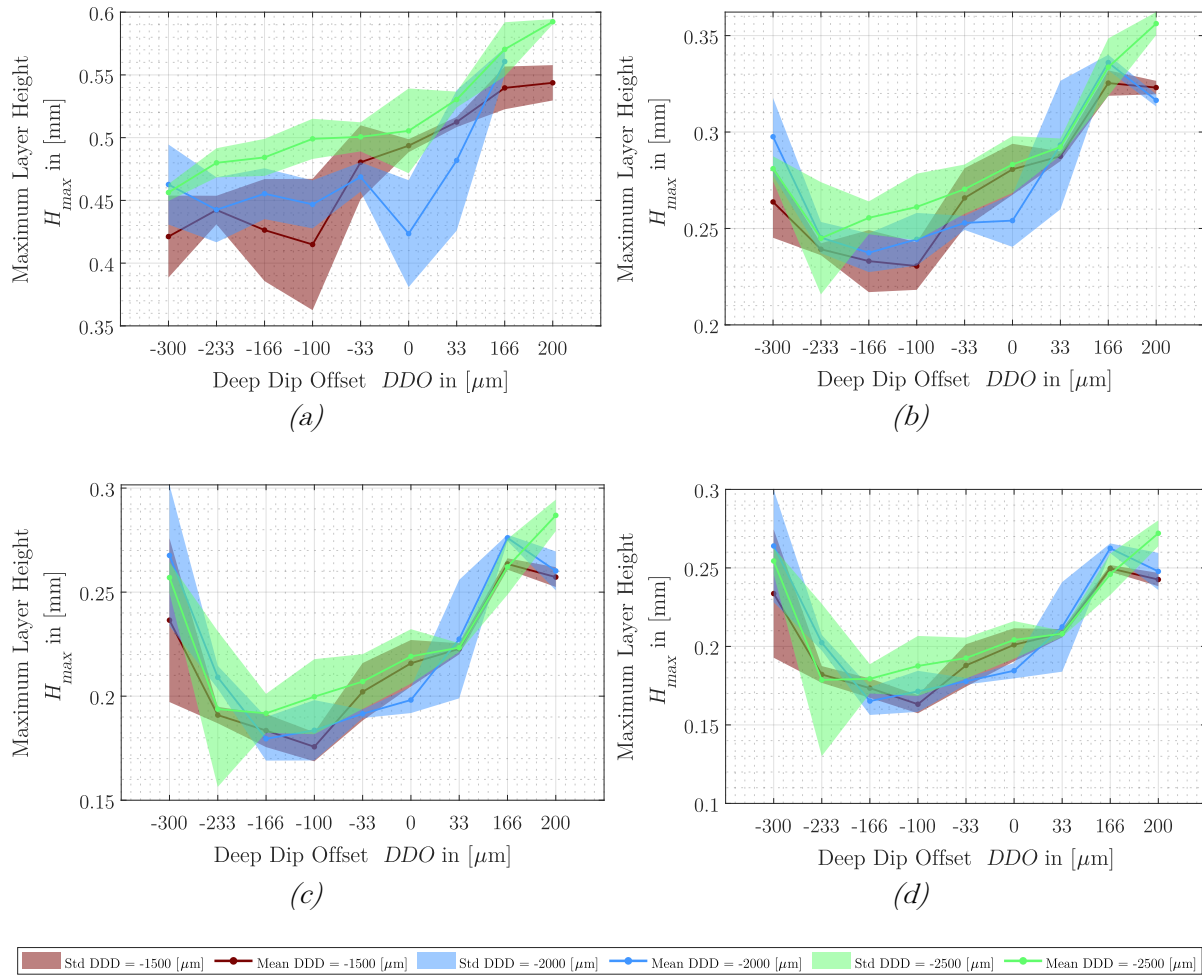


Figure 5-14: Showing the slices for four different points in time: (a) 30 s, (b) 150 s, (c) 300 s and (d) 360 s for all 3 DDD values.

In Figure 5-14 the mean (solid line) and standard deviation (shaded area) of the maximum layer height are shown for four different points in time for all 3 DDD datasets. Therefore, with this figure, the maximum layer height can be compared over time. The figure shows in (a) that 30 s after the first scan, the layer height is overall higher for the dataset with  $DDD = -2500 \mu\text{m}$ , followed by the layer heights of  $DDD = -2000 \mu\text{m}$  dataset and is overall lowest for the dataset  $DDD = -1500 \mu\text{m}$ . This can also be seen more clearly when computing the average layer thickness from all DDO values individual for each DDD dataset and plotting it over time, which can be seen in the following Figure 5-15.

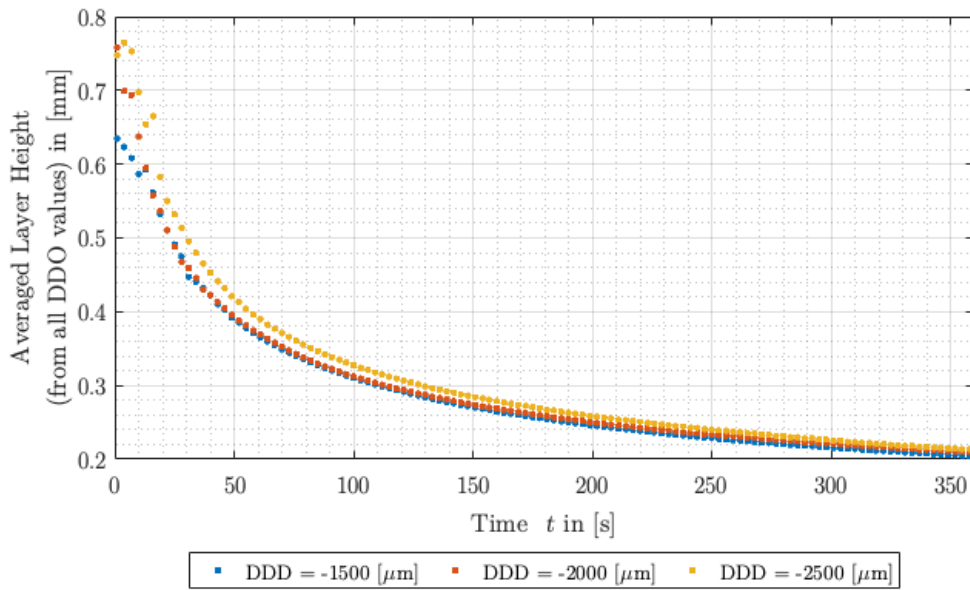


Figure 5-15: The maximum layer height averaged from all DDO values over time for each DDO dataset.

From Figure 5-15 it can be seen that the overall layer thickness is slightly higher for the  $DDD = -2500 \mu\text{m}$  dataset. Furthermore, the layer thicknesses of each  $DDD$  dataset align more for an increase time but differ mostly in the beginning. This indicates that the  $DDD$  value mostly influences the start volume, since with lower  $DDD$  values the build platform is submerged deeper into the resin vat than with higher values. This leads to a greater liquid volume above the build platform. Subsequently when driving up the build platform after submersing it in the liquid, more liquid is raised and dragged above the initial liquid surface. This can lead to a higher initial layer height as more liquid is dragged up and needs to flow away to the sides of the build platform. It should be mentioned, that the used driving up speed of the z stage was constant for all datasets with a speed of  $1 \text{ mm/s}$ . The liquid volumes above the submerged build platform can be calculated and are displayed in the following Table 2-1 and were calculated with a build platform width of  $10 \text{ mm}$  and length of  $20 \text{ mm}$  and the used  $DDD$  values.

Table 5-3: Obtained volumes above the submerged build platform.

<i>DDD</i> in [mm]	1.5	2	2.5
Volume in [m <sup>3</sup> ]	$3 \cdot 10^{-7}$	$4 \cdot 10^{-7}$	$5 \cdot 10^{-7}$

All in all, the key findings regarding the layer generation for this experiment can be summarised as the following:

- The measured maximum layer heights decay exponentially, because liquid photopolymers flow from the build platform downwards to the liquid bulk. This was shown in Figure 5-6.
- The flow of liquid photopolymer is greatly influenced by the chosen *DDO* value as the
- Figure 5-8 shows. The reason here seems to be the final position of the build platform relative to the initial layer height influencing the liquid flow strongly.
- The lowest obtained layer height can be found only for negative *DDO* values in the range of -233  $\mu\text{m}$  to -100  $\mu\text{m}$ .
- The obtained layer shape is highly influenced by the skewness of the build platform.
- It can be stated that a decrease in the *DDD* parameter, will result in an overall increase in layer height as it can be seen in
- Figure 5-15. Furthermore, it will lead to a decrease in the minimal obtained layer height with the *DDD* is increased as it was shown in Figure 5-9. Here Figure 5-9 also shows that, the *DDO* values for those minimal layer heights are since an in *DDD* values results in an increase of the *DDO* values. It seems to be caused by an increase of the start volume with lower *DDD* values.

It should be stated that the build platform used in this experiment had a rectangular shape. Therefore, the layer formation will exhibit probably two different result depending on the scan direction. In this experiment it was only scanned in y-direction and therefore

an extra investigation should be done for the x-direction. A circular shaped build platform could also be used to obtain axis-symmetrical results.

Furthermore, the environmental influences like ambient temperature, humidity and pressure related to the obtained measurements and no significant correlation to the measurement could be observed. However due to a lack of time it will not be discussed in this work.

This experiment and its previously stated findings will be now expanded in the upcoming experiment 2 in chapter 6 and here the influence of the viscosity shall be investigated in more detail.

## 6. Extension of the Setup with a Heated Resin Vat

From the findings of experiment 1 in the previous chapter 5, the found dependencies shall now be extended with an investigation of the viscosity. Therefore, the motivation and goal for this experiment shall be outlined in subchapter 6.1. The used methodology will be explained in 6.6., followed by the obtained results in 6.7. which will be discussed in 6.8.

### 6.1. Motivation and Goal

From the results obtained in experiment which can be seen in figure 5-5, on the right-hand side the obtained minimal layer height can be seen. As expected, the obtained layer height is significantly higher than the obtained layer heights from W. Tan. et al. resulting from the high viscosity of PR48 at room temperature. Therefore, to improve the overall printing process for the conceptual P $\mu$ SL system which was shown in 3.1 the overall settling time for the final layer height should be reduced as well as the actual layer thickness, since layer thickness also partially determines the printing resolution in z-direction which was also mentioned in section 2.3.3. A way for decreasing the temperature of the used photopolymer is to heat it up, which was discussed previously in 2.3.4. For this reason, the measurement setup will be extended with a heated resin vat.

### 6.2. Heated Resin Vat Setup

As stated, before a heated resin vat will be employed in order to increase the resin temperature. Therefore, a metal resin vat was designed consisting of a metal container and it can be seen in the following Figure 6-1.

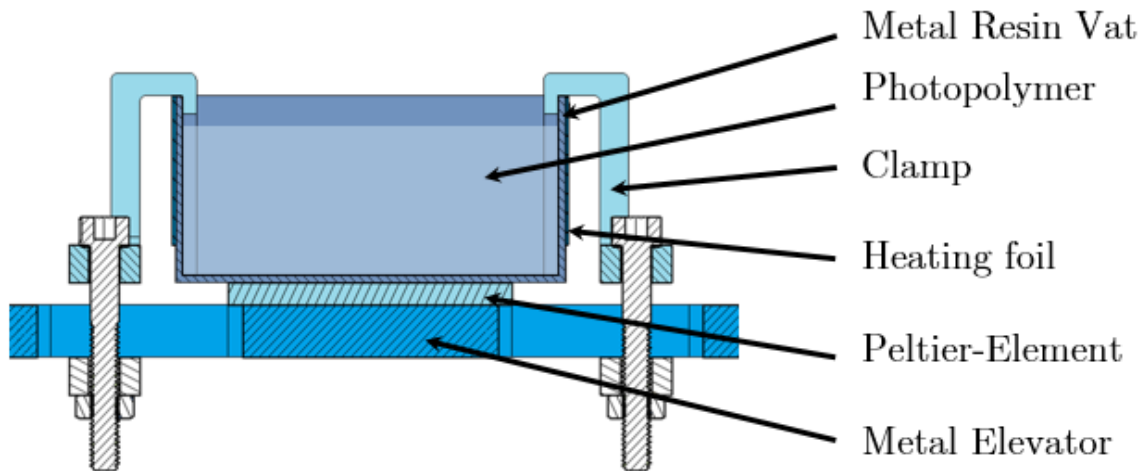


*Figure 6-1: A slice through the heated resin vat showing its components*

Figure 6-1 shows the metal container is placed on top of a peltier-element and on the sides of the metal container heating foils where placed. A peltier-element is a thermo electric element consisting of multiple semiconductor elements which are placed in series and are alternated between n-conducting elements and p-conducting elements. If a current is flowing through those semiconductor elements, the peltier effect starts to receive energy in form of heat on those semiconductor elements, creating a heat flow. Subsequently, the peltier-element is receiving a heat flow at one side (cooling) and must return this heat flow on another side (heating). To increase the heat flow, the peltier-element is connected to two metal surfaces with an additional thermal interface material in between. Therefore, the new metal resin vat and the peltier-element is placed, on top of an new elevator build out of metal which is like before connected to the manual OWIS z-stage. As a result, the peltier-element is placed between two metal objects acting as radiators resulting in a better heat transfer. Additionally, clamps with screws where employed to generate enough contact pressure between the peltier-element and the metal surfaces. Additional heating foils placed on the sides of the resin vat to additionally heat the sides of the resin vat to generate a more homogenous thermal distribution in the heated photopolymer. Furthermore 3 temperature sensors were employed to the heated resin vat to monitor the temperature of the photopolymer. The peltier-element, heating

foils and temperature sensors were connected to a control circuit, which can be seen in a electrical schematic in Figure 6-2.

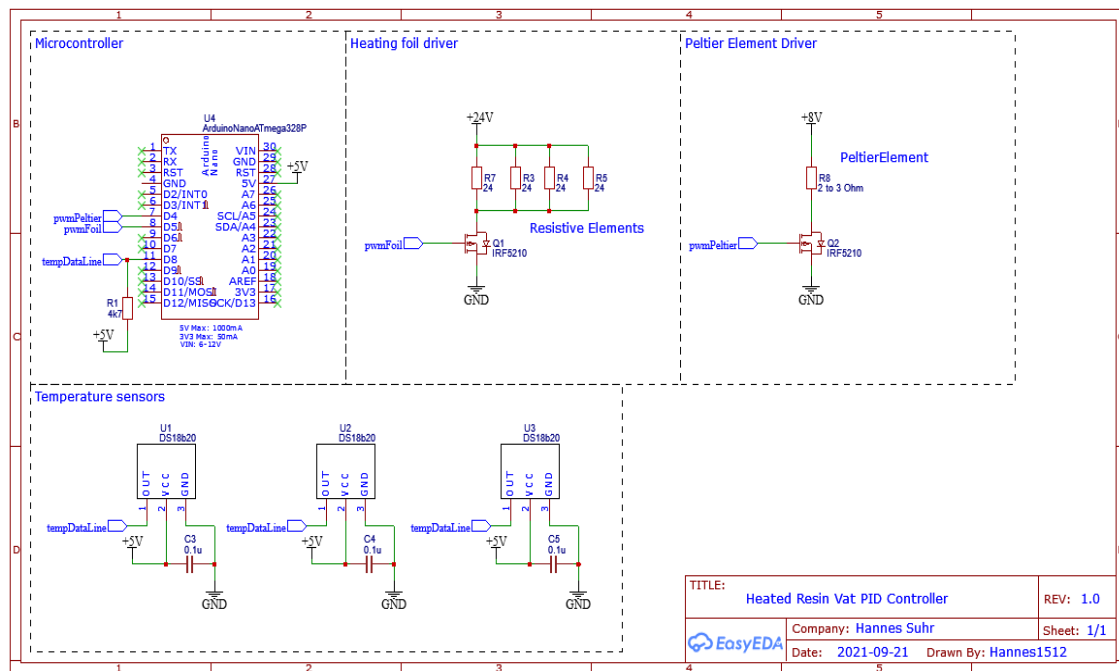


Figure 6-2: The control circuit for the heated resin vat.

As it can be seen in Figure 6-2, the control circuit consists of a Arduino nano microcontroller, three DS18B20 temperature sensors four heating foils as mentioned earlier and a peltier-element. The temperature sensors are connected to the microcontroller via a single data line. The four heating foils which are resistive elements, where controlled with a MOSFET IRF5210 low-side switch turned on and off through a pulse width modulation (PWM) signal. Furthermore, the peltier-element is also driven by a low-side switch and a PWM signal. The PWM signal is generated by the microcontroller, which runs a software system incorporating a digital PID controller. Where PID stands for proportional-integral-derivative meaning that a signal from the temperature sensors is analysed regarding the present (proportional), future (derivative) and past (integral). With these analyses, a control signal which is the PWM for the heating and peltier-element is created. As a result, a control loop is employed constantly analysing the temperature signal and therefore adjusting the power above the heating

elements to maintain a consistent temperature. An example for a PID control systems can be seen in the following block diagram in Figure 6-3.

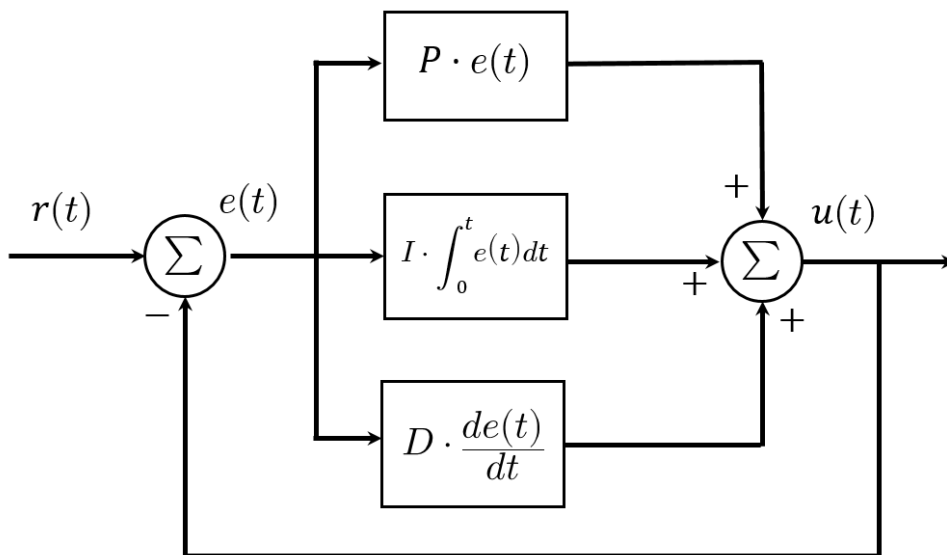


Figure 6-3: The block diagram of a PID system.

From Figure 6-3 it can be seen that in a PID system an input time signal  $e(t)$  which is the difference between a measured signal  $r(t)$  and a set value is fed into the P, I and D blocks where different functions are applied to the difference signal  $e(t)$  and later summed up to the control signal  $u(t)$ . This control signal is then used to control the overall system.

Coming back to the power supply, the 24V for the heating foils is generated via a boost converter, stepping up the 8V input voltage delivered by a lab bench power supply. This Power supply also delivers the 5V for the microcontroller and temperature sensors.

### 6.3. Heated Resin Vat Software

A software system was developed in MATLAB to control the heated resin vat. Additionally, a microcontroller was written in C. Both software systems communicate to each other via serial communication. Here the MATALB program connects to the microcontroller and sends commands to it, including the current set temperature of the

resin vat. Additionally, the Arduino sends back the current temperature data from all three sensors and the current PWM values for the heating foils and peltier-element to the MATLAB program. The obtained data is then displayed to the user via a GUI. Furthermore, the MATLAB software logs the data and saves it in a .xlsx file containing the set temperature, current temperature and PWM values from the controller and therefore can be used for later analysis.

#### 6.4. Changes to the Experimental Setup

According to the findings from experiment 1 in chapter 3, it was found that the scan distance of the build platform was changing during the Deep Dip measurements. Therefore, for this experiment, the confocal sensor mount which was previously 3d printed, was redesigned, and build out of metal to withstand the force of the optical fibre cable acting on the sensor. This should result in more accurate measurements. Additionally, the new heated resin vat was installed into the existing setup and therefore the entire measurement setup can be seen in the following Figure 6-4.

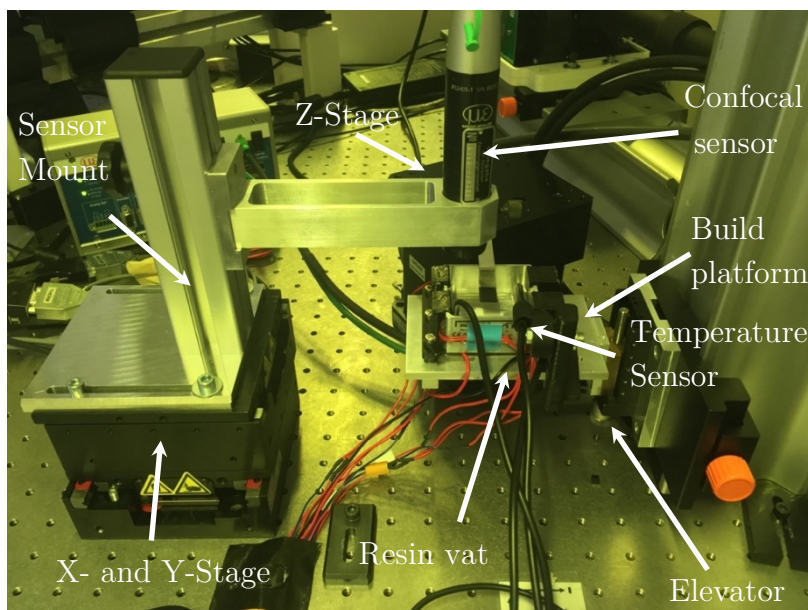


Figure 6-4: The measurement setup with the metal sensor holder and heated resin vat.

From Figure 6-4 it can be seen that the measurement setup remains mostly the same to the previous one from experiment 1. The elevator which can be in the middle with the resin vat was simplified since it is now made out metal which does not need the lino guiding rail as before. The new sensor mount can be seen in Figure 6-4 on the left-hand side.

## 6.5. Validation Measurements

Before any more experiments were conducted, the resin vat was tested if it can generate stable photopolymer temperatures. Therefore, the PID values must be tuned. Here the PID values mean that in a PID control system the proportional, integral, and derivative computation of the temperature is multiplied with the according P, I and D scaling factor to weight each PID component, which was shown in 6.2. Therefore, depending on the different P, I and D values, the behaviour regarding control system can be altered. For example, if the D component is increased the PID system will look more into the future behaviour of the measurement signal, and sudden changes in the signal will be anticipated. Otherwise, if such a value is set too high, then the PID controller can oscillate regarding the control signal. Therefore, the PID values must be tuned carefully. As a result, the PID tuning measurement will be shown in 6.5.4. After successful tuning of the PID parameters, the resin surface temperature was measured at different points to measure the resin vat temperature homogeneity which will be shown in 6.5.5.

### 6.5.1. PR48 Viscosity Measurement

To verify the viscosity dependence on the temperature, a pre-test was conducted in the laboratory before starting this thesis. In this test, the viscosity was measured for different temperature values, which can be seen in the following Figure 6-5.

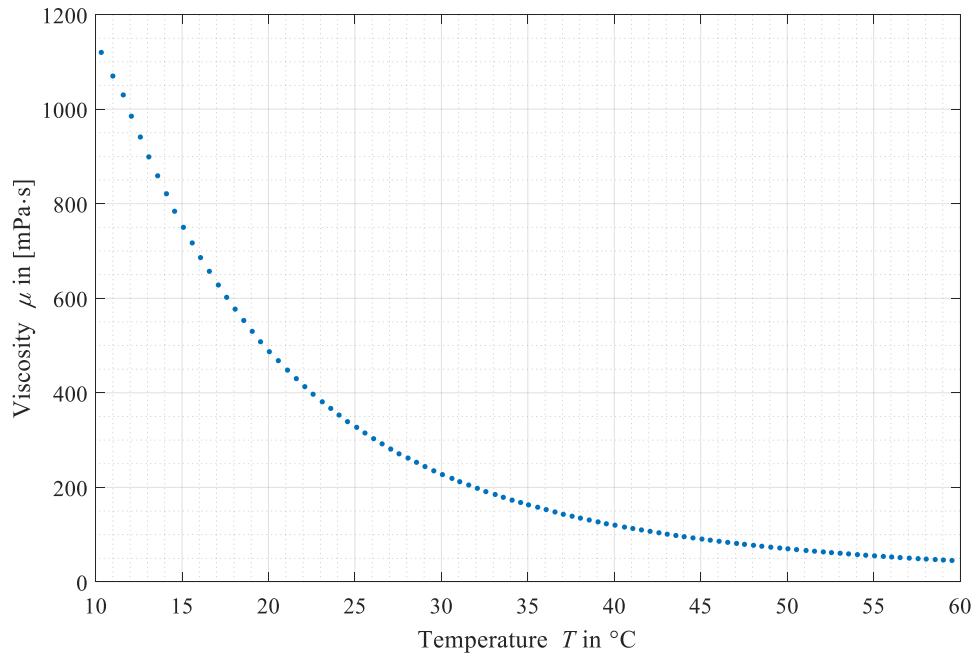


Figure 6-5: Showing the decrease of the Viscosity of PR48 depending on the temperature.

As it can be seen from Figure 6-5, the viscosity is displayed in dependency to the temperature and the viscosity follows an exponential decay as it was discussed earlier in 2.3.4 and shown in equation (2-3). Temperature values for 21  $^{\circ}\text{C}$  and 60  $^{\circ}\text{C}$  can be seen in the following Table 6-1.

Table 6-1: Viscosity values for 21 $^{\circ}\text{C}$  and 60  $^{\circ}\text{C}$

Temperature in [ $^{\circ}\text{C}$ ]	21	60
Viscosity in [ $\text{mPa}\cdot\text{s}$ ]	450	100

From Table 6-1 and Figure 6-5 the viscosity from 21  $^{\circ}\text{C}$  to 60  $^{\circ}\text{C}$  degrees can be reduced to factor 4.5. Furthermore, due to the exponential decay the viscosity slope for higher temperature compared to lower temperature is much lower, meaning, that a change in temperature at about 60  $^{\circ}\text{C}$  will not yield high viscosity changes compared to 21  $^{\circ}\text{C}$ , which overall could improve the Deep Dip process stability. Therefore, throughout the following experiment in 6.7, a temperature value of 60  $^{\circ}\text{C}$  at the liquid photopolymer surface was targeted.

### 6.5.2. Refractometer Measurements PR48

Since this experiment deals with layer thickness measurements of a heated liquid photopolymer with a confocal sensor, the change in dispersion of the liquid must be considered as it was pointed out in subchapter 2.2.4, where dispersion means that the refractive index is depended on the wavelength. Therefore, the refractive index  $n_d$  at a wavelength of 587.56 nm at different temperatures was measured, with a DR 6000 from Dr. Krüss. Specifications to this device can be seen in the appendices on page 165. To receive the Abbe number, which is needed for the confocal sensor and is a metric for describing a materials dispersion, the other two refractive indices namely  $n_F$  and  $n_c$  were measured with an SFRIM setup, which was developed in the lab. From there it was assumed that the refractive indices  $n_F$  and  $n_c$  behave the same as  $n_d$  over different temperature value. Therefore, all three refractive indices can be known for different temperature values. Consequently, Abbe number was computed from the refractive indices by using the following equation (6-1 [43]).

$$V_D = \frac{n_d - 1}{n_F - n_c} \quad (6-1)$$

The results of the measurements and computations regarding the refractive indices and Abbe number can be seen in the following Figure 6-6.

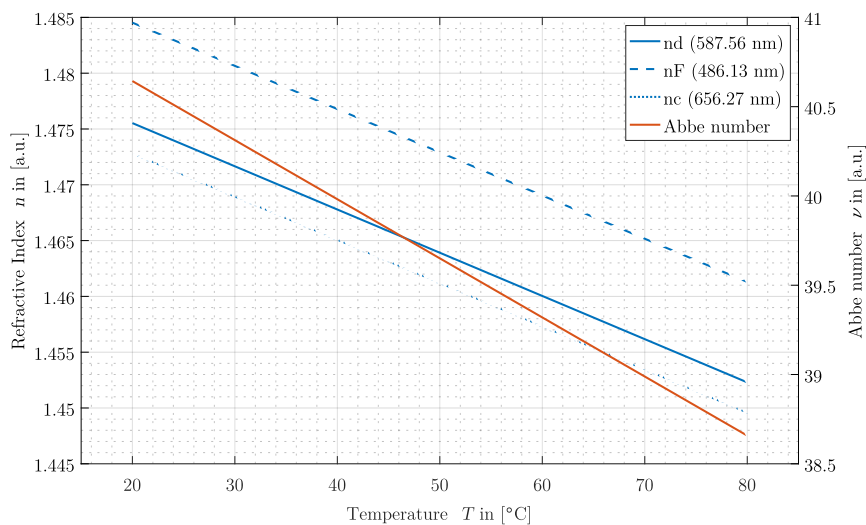


Figure 6-6: The refractive indices for three different wavelengths and the computed Abbe number

From Figure 6-6 the refractive index is declining for an increase in temperature. Since it is assumed, that the refractive indices  $n_F$  and  $n_c$  behave the same as  $n_d$ . The Abbe number declines too for an increase in temperature and as a result the obtained values for a temperature of 60 °C where fed into the sensor measuring layer thickness.

### 6.5.3. Temperature Sensor Calibration

Before any measurements with the new resin vat where performed, a temperature sensor test was performed, to compare the temperature sensors used in the heated resin vat with other sensors from the lab. The used sensors where two BME280 sensors called “LabLogger” 1 and 2, the three DS18B20 temperature sensors called T1, T2 and T3 as well as an Trotec T210 Thermo-Gyrometer. The specifications for the DS18B20 and Trotec Thermometer can be found in the Appendices. Since not all sensors can be used for high temperatures like 60 °C and be submerged in a liquid, this comparison was only conducted at room temperature at ambient air. All sensors where packed together onto a single spot of approx. 5 cm diameter in a climate box to protect the measurement from environmental air flow. The measurements were conducted over a time interval of 30 min and before that, the sensors were turned on 15 min prior to the measurement, so that self-heating from the electrical circuits of the sensors do not influence the measurements that much. The standard deviation and mean values for each sensor where computed and are displayed for each temperature sensors can be seen in the following Figure 6-7.

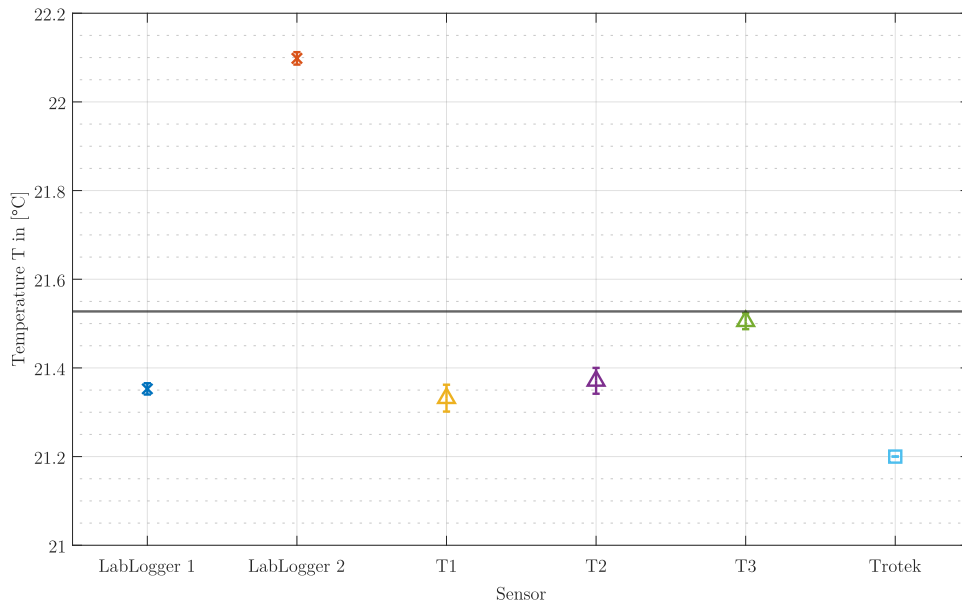


Figure 6-7: The measured temperature values for the 6 used temperature sensors.

From Figure 6-7 the mean and standard deviation of the measured temperatures for each sensor can be seen. All measured temperatures were in the range of 21.2 °C to 22.1 °C. The global average was computed and can be seen as a black line with a value of 21.53 °C. From this measurement, the difference from the three resin vat sensor to the global average was computed.

The computed difference values were incorporated into the sensor output of the microcontroller software, so that the obtained sensor results are calibrated. However, it should be mentioned, that the three sensors from the resin vat will be used in the later experiment at a much higher temperatures ranging from 60 °C to 80 °C and therefore the accuracy of the sensors can deviate there much more. An additionally study about the temperature behaviour was not conducted because of a lack of time. Further conclusions about the sensor deviations forth resin vat sensors can be seen in the following Figure 6-8, showing the error curves for the DS18B20 sensors.

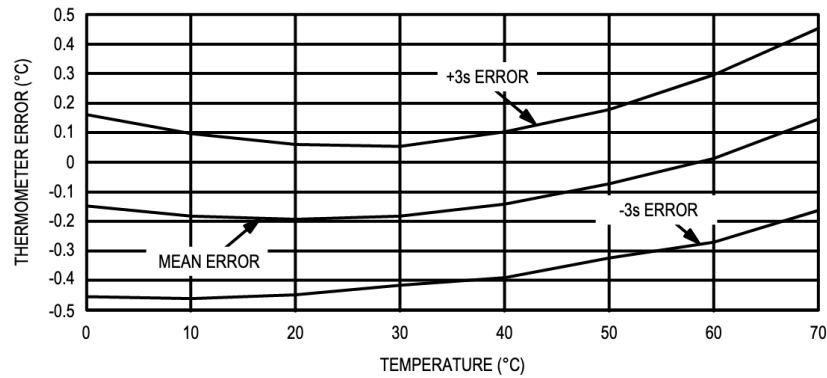


Figure 6-8: The measurement errors in dependency of the temperature for the used DS18B20 sensors which will be placed in the liquid resin vat [44].

From this Figure 6-8 it can be seen that the error of the sensors will increase with an temperature increase, which can negatively affect the accuracy of the temperature measurement later when heating the liquid photopolymer.

#### 6.5.4. PID tuning Measurements

The PID parameters were tuned with the Ziegler-Nichols method, meaning that first the I and D gain are set to 0 and only the P gain is increased until stable oscillations can be observed. First the resin vat and new elevator were connected to the experimental setup. Then the resin vat was filled with 50 ml of PR48. A target temperature of 60 °C as set up. The temperature sensor for this experiment was placed on the ground of the resin vat. As mentioned before first the P Values was increased until oscillations around the target temperature could be observed. This happened at an P value of 16. Following the D gain was increased, and a more stable behaviour could be observed at a value of 16. Finally, the I gain was increased and to a value of 3. Above these values, the PID system started to oscillate. Therefore, the final PID values where  $P = 16$ ,  $I = 3$  and  $D = 16$ .

A final measurement with the above stated values was conducted for a target temperature of 60°C and it can be seen in the following Figure 6-9.

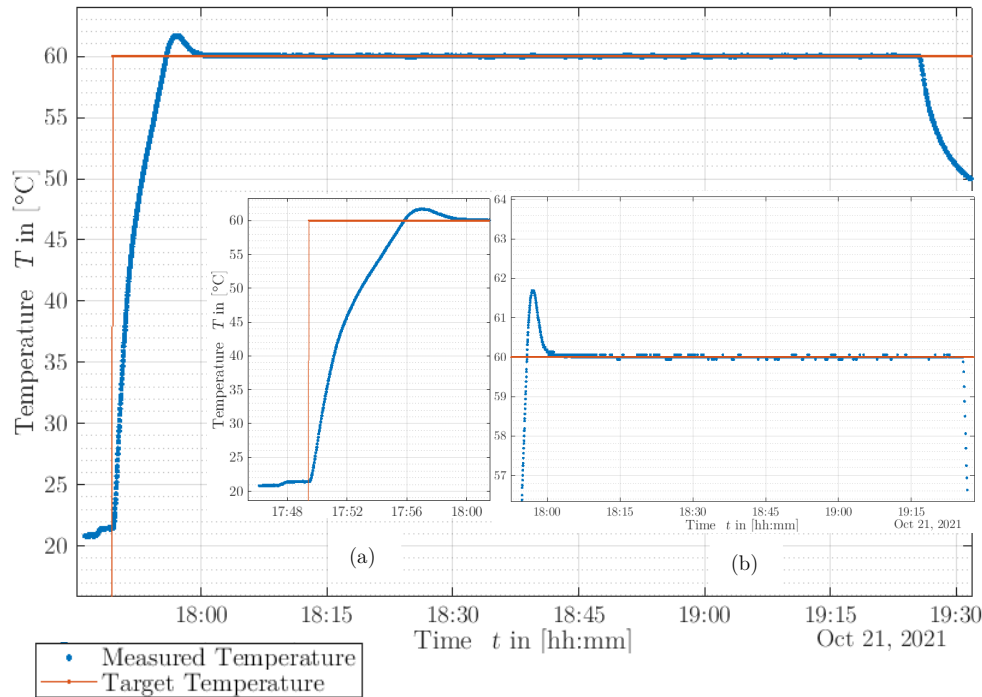


Figure 6-9: Sowing the final temperature test with a set temperature of 60°C (orange) and the measured temperature in blue.

From Figure 6-9, the measured temperature and the set temperature can be seen. The beginning of the heating process is magnified with diagram (a) and the deviations of the measurement to the set value can be seen in (b) in more detail. In the beginning the resin vat heats up the bottom liquid photopolymer up to 60 °C in around 8 minutes which can be seen in (a). Additionally, an overshoot of the measured temperature is observable however two minutes after the overshoot, the measured temperature is in fact equal to the target of 60 °C. After the target temperature was reached, the controller was able to hold the temperature stable which is visible in (b). Here a standard deviation of 0.028 °C observed with a mean value of 60.012 °C. This proves that the developed system can regulate the temperature according to a measured temperature value. Nonetheless the temperature homogeneity must be measured before the actual experiment can be started. This validation test will be shown in the following section 6.5.5.

### 6.5.5. Resin Vat point temperature measurement

When performing the upcoming experiments with the heated resin vat, the build platform will dive into the photopolymer surface. In the middle of the resin vat. Additionally, the temperature of the heated resin vat should be measured as close as possible to the build platform, but without disturbing the Deep Dip process. One method to achieve this is to first map the liquid photopolymer temperature at the point where the build platform is later positioned for the Deep Dip process and at a point where the temperature sensor can be safely positioned when the Deep Dip process is executed. Therefore, a temperature gradient can calculate and therefore a statement about the photopolymer temperature at the build platform position can be made without the need to measure directly at the build platforms position and disturbing the Deep Dip process. Therefore, at different positions in the resin vat the photopolymer temperature was measured at a constant fill height. Additionally, it should be mentioned that for this test three different temperature sensors where used. One was placed on a fixed position on the bottom of the resin vat, another one fixed approx. 1 cm above the first one with a 90 degree angle and the third sensor was immersed partially into the liquid photopolymer surface and was placed at different points. The sensor configuration can be seen in the following Figure 6-10:

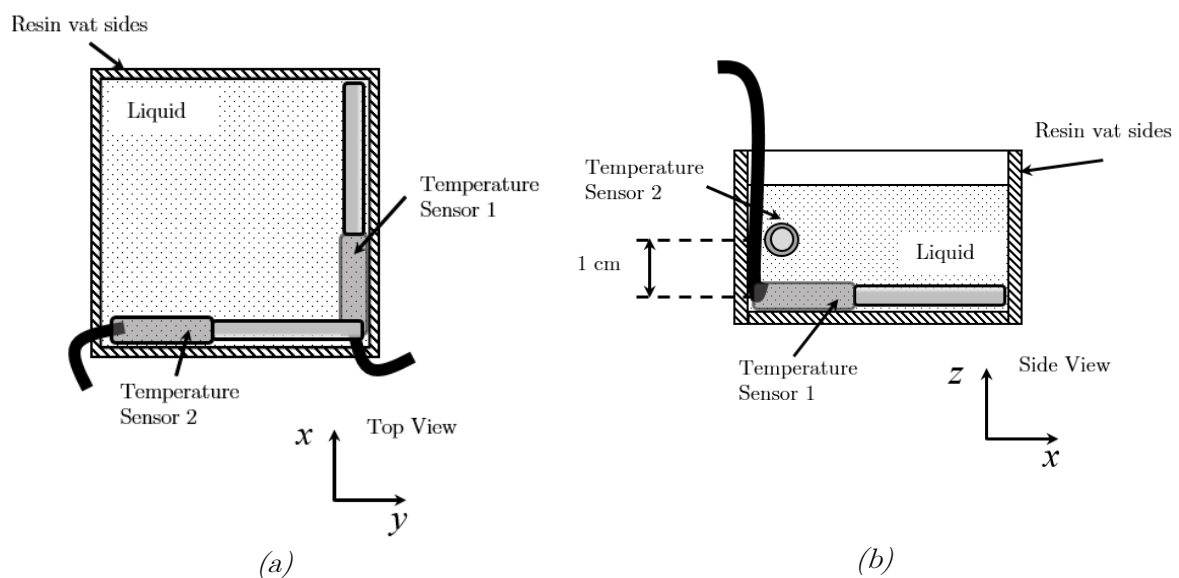


Figure 6-10: Showing the Sensor configuration of temperatures Sensor 1 and 2 from the top in (a) and from the side in (b)

Furthermore, the third temperature sensor was immersed at a fixed depth into the liquid photopolymer for each point. Three different positions of interest were selected and it can be seen in the following Figure 6-11.

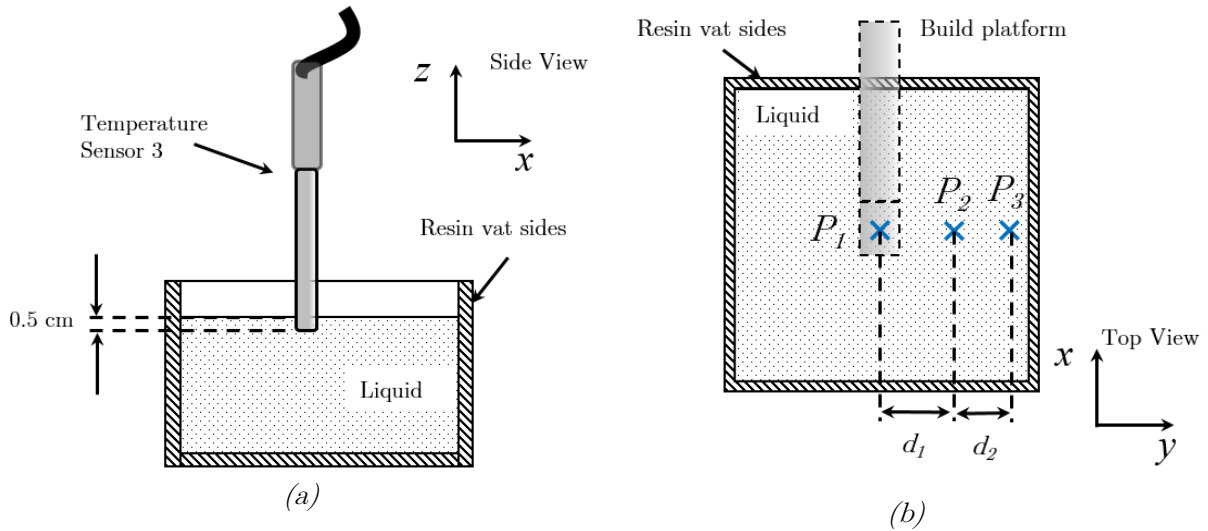


Figure 6-11: Showing the Configuration of the sensor 1 and the 3 measurements positions.

The obtained temperature measurements can be seen in the following Figure 6-12.

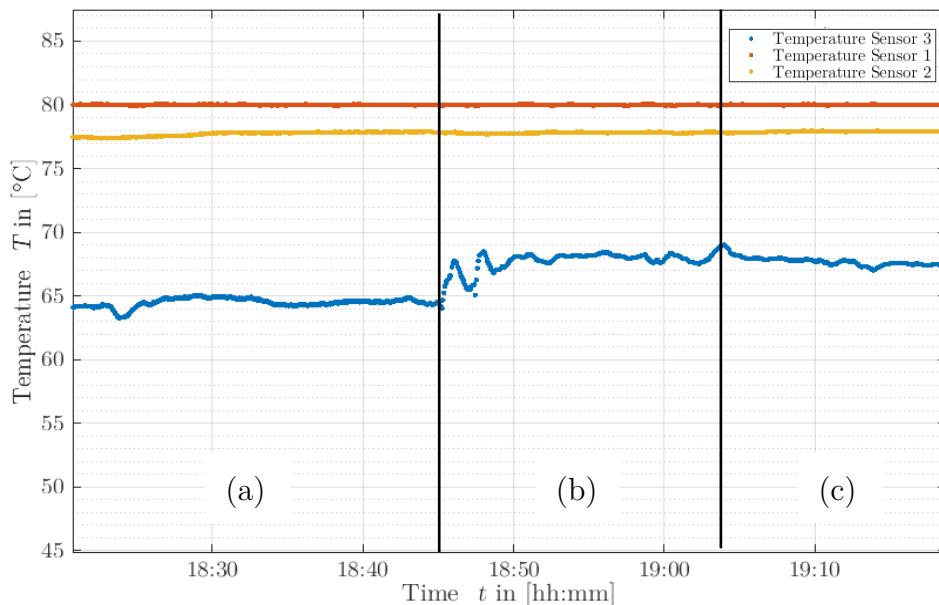


Figure 6-12: Temperature measurements at three different points in the heated resin vats measurement, where (a) is for  $P_1$ , (b) for  $P_2$  and (c) for  $P_3$ .

From Figure 6-12 the temperature over time can be seen for all three sensors positions. Furthermore, the set temperature was 80 °C and was measured with sensor 1 on the bottom. In (a) the temperature from sensor 3 is lower at position 1 compared to position 2 and position 3, which can be seen in (b) and (c). A temperature difference from position 2 (b) and position 3 (c) can be seen but is not as significant as before. Furthermore, the temperature in sensor 2 is lower compared to sensor 1 with a value of 78 °C since it was positioned around 1 cm above the sensor 1 on a different side. The obtained mean values and standard deviation values for Sensor 3 for all three positions can be seen in the following Table 6-2.

*Table 6-2: Mean and standard deviations for the Temperature measurement for 3 positions.*

Position	$P_1$	$P_2$	$P_3$
Mean Temperature in [°C]	64.481	67.780	67.701
Std Temperature in [°C]	0.3603	0.6473	0.4192

From this test, it can be stated, that the temperature in centre of the resin vat is lowest compared to the right-hand side in y-direction of the resin vat. Therefore, if the build platform is placed in the centre at point P1 and the temperature sensor on point P2 or P3, then the photopolymer temperature at point P1 can be estimated from the sensor reading at P2 or P3. Additionally, a temperature gradient can be observed from sensor 1 to sensor 3 in z-direction with a difference of 15 °C. Therefore, the set temperature for the bottom sensor should be set 15 °C above the desired surface in the actual experiment, since the bottom sensor reading is used as the control signal.

It should be mentioned, that the obtained temperatures were influenced by certain parameters, which can be seen in the following Figure 6-13.

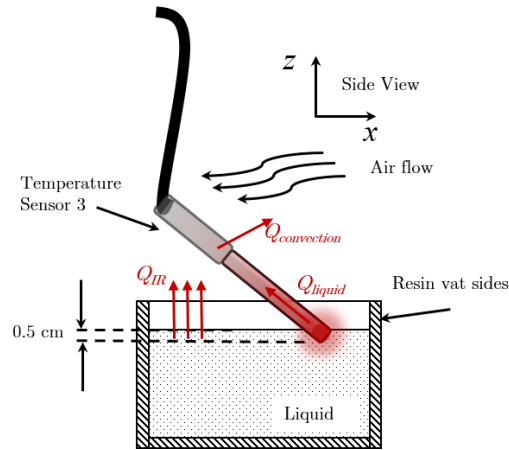


Figure 6-13: Showing various influences on the temperature measurements.

For example, from Figure 6-13 the sensor 3 was only immersed for 0.5 cm into the photopolymer. Therefore, heat conductivity to the surrounding air could have influenced the measurements since the temperature sensor metal shell can pass heat through convection to the air and therefore the sensor is subsequently cooled. Additionally heat in form of infrared radiation can additionally heat the sensor, but since the sensor shell is made from metal IR radiation can be reflected. Furthermore, the heat flow from the sensor tip creates a temperature gradient across the sensor frame and depending on how the actual semiconductor sensor is positioned inside the shell, the surface temperature may not be measured correctly. A better alternative would be to use smaller temperature sensors to measure a thin layer more precise.

## 6.6. Methodology

The sensor configuration for the experiments conducted are the same as shown in section 6.5.5, where the temperature sensor one was placed on the bottom and temperature sensor 2 was placed 1 cm above and the sensor 3 was immersed into the liquid next to the build platform positions for a depth of 5 mm. The readings from sensor 1 were used as the control signal as before in 6.5.5.

Before any measurement was done, the resin vat was pre-heated without the photopolymer and the set temperature was set to 75 °C for around 5 minutes. As shown before a temperature gradient from the bottom sensor to the liquid surface is around 15 °C which should result in a surface temperature of 60°C.

After this the photopolymer was filled into the resin vat a waiting time of 20 minutes set for the photopolymer to heat up and reach a stable temperature. Since the new resin vat has a new since, the resin vat was now filled with 50 ml of PR48 before any measurements so that the conditions stay the same like in the previous validation measurement in 6.5.5.

The methodology of measuring layers with the Deep Dip systems remains the same as described before in experiment 1 in subchapter 5.2 from this point on. Furthermore, the setup of the optimal scan distance to the build platform remained the same, as well as the fill stand measurements which were also described in 5.2.

From the findings in experiment 1 it was shown that a minimal layer height was observed for negative *DDO* values. Since a future printing process wants to obtain layer thickness as low as possible, the conducted measurements were executed for negative *DDO* values from -233 µm to -33 µm. Since only the viscosity shall be investigated a fixed *DDD* value of -2000 µm was chosen and the BP to RV ratio remained constant at 0.0852.

Also, from the findings in experiment 1 it was observed that the liquid layer did not reach an equilibrium and therefore were still moving the final layer scans. Therefore, for this experiment, the overall measurement time was double, from 360 s to 720 s.

## 6.7. Results

The experimental results from the second experiment can be seen in the following graphs in Figure 6-14, showing the  $H_{max}$  and the  $ROC_{norm}$  for each  $DDO$  values, with a  $DDD$  value of  $-2000 \mu\text{m}$  and an BP to RV ratio of 0.0852 and a photopolymer viscosity of  $100 \text{ mPa} \cdot \text{s}$ .

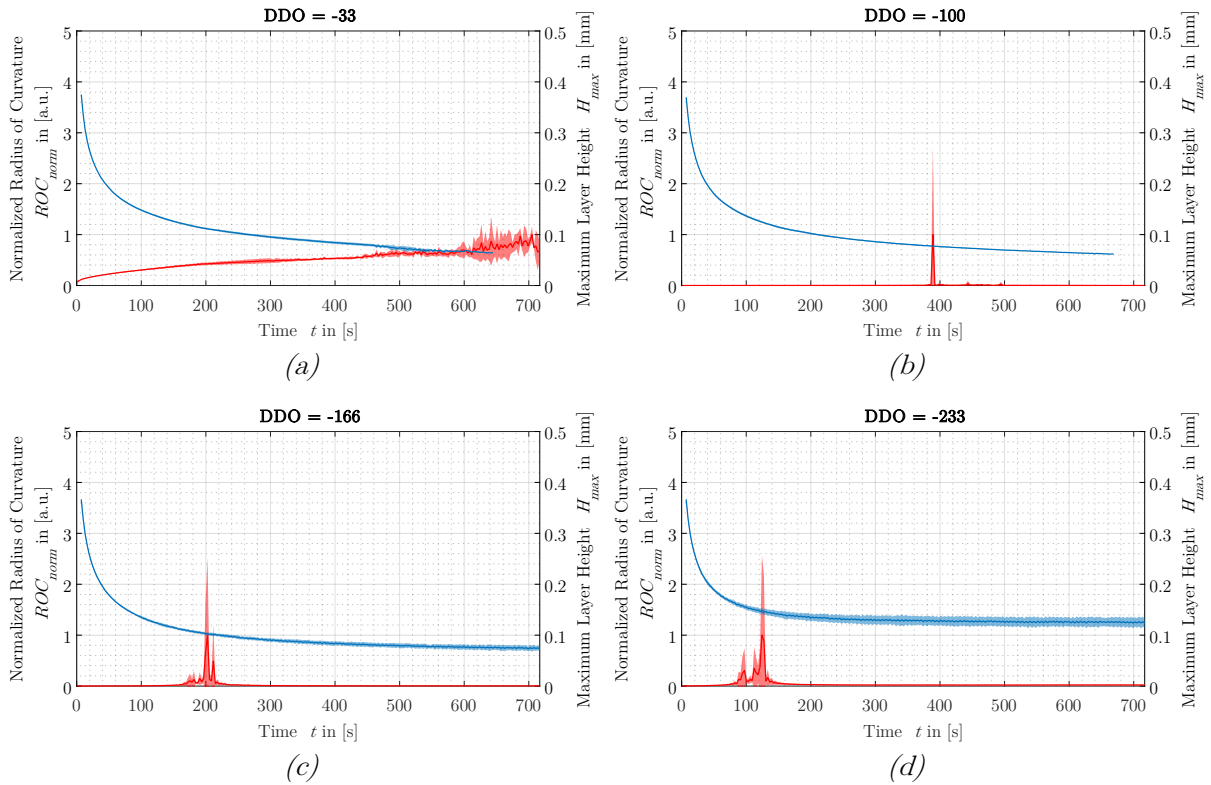


Figure 6-14: The layer measurements showing the  $H_{max}$  and the  $ROC_{norm}$  for each  $DDO$  values, with a  $DDD$  value of  $-2000 \mu\text{m}$  and an BP to RV ratio of 0.0852.

## 6.8. Discussion

The results from subchapter Figure 6-14 shall now be discussed. Figure 6-14 shows the individual measurements for each  $DDO$  value for a viscosity of  $100 \text{ mPa} \cdot \text{s}$ . The exponential decay of the measured maximum layer height is still existing like in experiment 1. Furthermore, it can be observed that the starting layer height is much lower compared to the measurements with a viscosity of  $480 \text{ mPa} \cdot \text{s}$  and was measured at below  $0.4 \text{ mm}$  for each  $DDO$  value. The settling time was decreased significantly. For example in experiment 1 at Figure 5-2 at (e) it can be seen that a maximum layer height was obtained of around  $200 \text{ }\mu\text{m}$  after  $270 \text{ s}$ , whereas here in Figure 6-14 (a), a maximum layer height of around  $100 \text{ }\mu\text{m}$  was obtained after the same amount of time. Overall, it can be said that the final layer height exhibits much lower values than in experiment 1. Furthermore, in (a) and (b) the measurements of the layer thickness could not be completed, stopping in each measurement at a layer thickness of  $65 \text{ }\mu\text{m}$  suggesting that the minimal measurable layer thickness of the confocal sensor was reached, which was earlier described in 3.4.2. This can be also displayed in the following Figure 6-15 below.

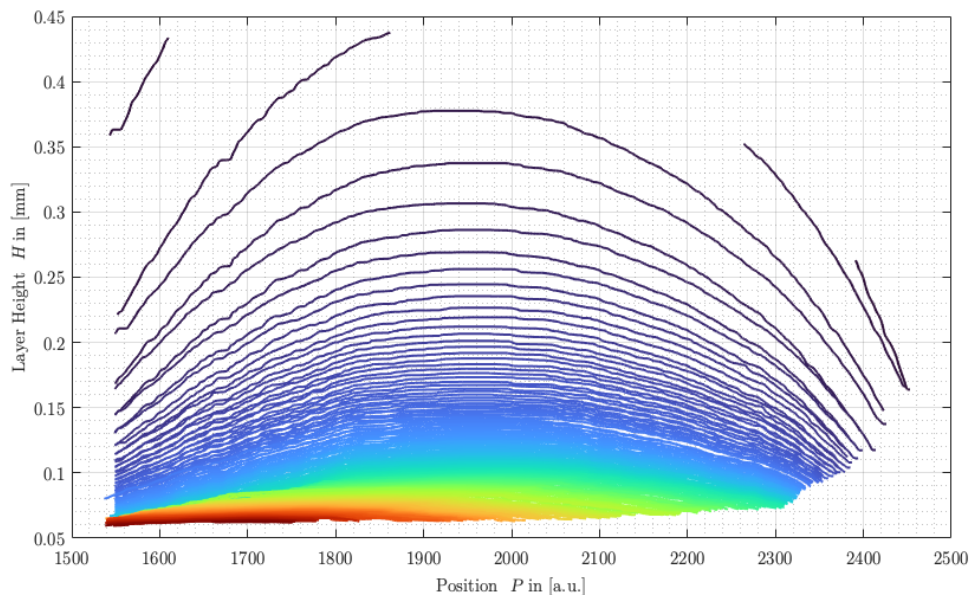
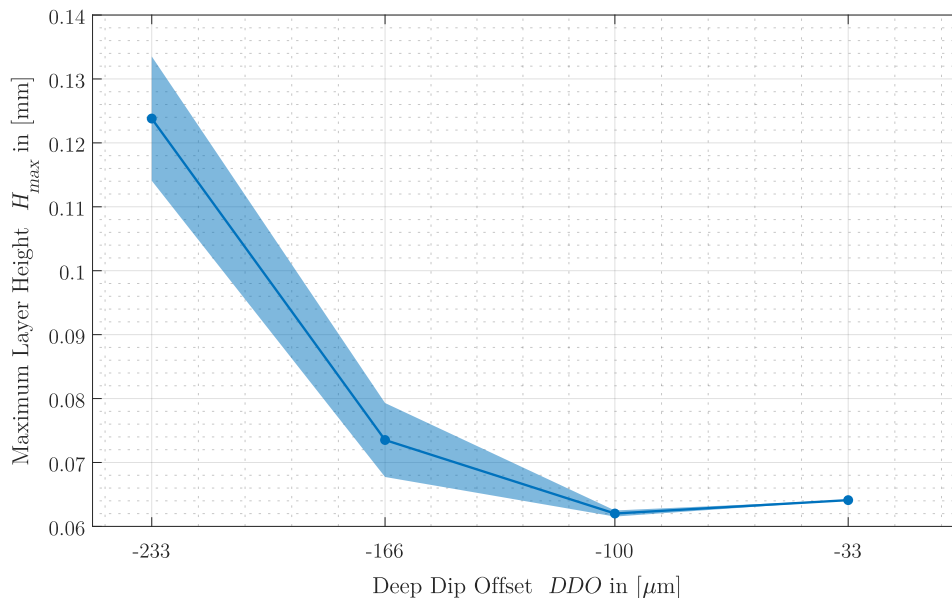


Figure 6-15: Showing the thickness dataset for a measurement with  $DDO = -33 \text{ }\mu\text{m}$  and  $DDD = -2000 \text{ }\mu\text{m}$ .

In Figure 6-15 the last layer measurements which should exhibit a red colour were not taken (or only partially) and therefore no layer below  $63 \text{ }\mu\text{m}$  was measured. This

behaviour was also observed for the measurements from (b). As a result, to obtain the full layer thickness, one should employ a new measurement method, where only a distance measurement is done and are reference measurement of the build platform beforehand. Subsequently with a reference measurement and layer measurement the layer thickness could be computed. With this it should be possible to measure even thinner liquid layers. Even though the liquid layers from (a) and (b) could not be measured till the last scan, we shall compare the last obtained layer heights for each  $DDO$  value, to see if the layer height is still influenced by this parameter and this comparison can be seen in the following Figure 6-16.



*Figure 6-16: The last obtained maximum layer heights are shown with the mean values as a dot and solid line and the standard deviation as a shaded area for each  $DDO$  value.*

From Figure 6-16 the maximum layer height is still influenced by the  $DDO$  parameter and potentially exhibits the typical “u” shape, that could also be observed in the experiment 1 in subchapter 5.4. The standard deviation for the shown scans, seem to be lower for  $DDO = -100 \mu\text{m}$  and  $DDO = -33 \mu\text{m}$ , however at those two measurement sets, the final last observable layer thickness do only have 2 or 1 measurement points compared to  $DDO = -233 \mu\text{m}$  and  $DDO = -166 \mu\text{m}$  measurement sets, which have all

three measurement points, and therefore the standard deviation seems to be lower for higher *DDO* values. Additionally, it should be stated, that the minimal observable layer thickness with the 100 mPa · s viscosity has a value of 63 µm for a *DDO* value of -100 µm and it can be seen in Figure 6-16, that the lowest layer heights appear again for lower *DDO* values, like it was shown before in experiment 1. Regarding the standard deviation of the obtained layers and comparing them to experiment 1, then the standard deviation is much lower in this experiment utilizing a much lower viscosity, indicating that a lower viscosity yields a more stable Deep Dip process. Coming to the *ROC*, the *ROC* exhibits a similar behaviour like before in experiment 1, where in the first part of a *ROC* measurement has an almost logarithmic behaviour and if the measured layer became flat, then a peak occurs like in experiment 1.

All in all, the key findings regarding the layer generation for this experiment with a lower viscosity can be summarised as the following:

- It shall be mentioned that the measured maximum layer heights decay exponentially, but much faster since the viscosity is lower compared to experiment 1.
- There seems to be that an influence of the *DDO* value to the final (or last) obtained layer heights is still existent and follows the same “u” curve
- The lowest obtained layer height can be found only for negative *DDO* values in the range of -100 µm.
- Only a reduced viscosity of around 100 mPa · s and lower can obtain low layer heights below 100 µm and therefore such a viscosity or even lower should be used for a future PµSL system.

Furthermore, for additional investigations regarding a lower viscosity, the thickness measurement problem must be addressed as discussed before. Additionally, because of a lack of time, a discussion about the temperature stability of the liquid photopolymer while performing the experiment was not conducted. Additionally, more measurements

with different viscosity values for the PR48 photopolymer should be conducted to obtain a more detailed investigation on the viscosity effect.

## 7. Mathematical Model

In this chapter, the findings from experiment 1 in chapter 5, which were summarized in subchapter 5.4 and the findings from experiment 2, which were summarized in 6.8 delivered new insights to the Deep Dip method. Therefore, at this point a mathematical model shall be built, which can describe the obtained results from experiment 1 and 2, which will be discussed in this chapter. The following subchapter will point out the motivation to build such a model in 7.1. as well show the methodology in 7.2. The results will be shown in 7.3 and will be discussed in 7.4.

### 7.1. Motivation and Goal

As mentioned in experiment 1, the *DDO* and *DDD* parameters were found to have an influence onto the obtained final layer thickness as well as the *ROC*. Furthermore, it was pointed out in subchapter 1.2, that no mathematical models exist to describe the Deep Dip method. Therefore, it would be suited to develop a model to describe the Deep Dip process and as a result be able to forecast the layer generation for a given set of parameters. This would make the layer generation process with the Deep Dip method more reliable and effective since no extra measurements and analyses for each different photopolymer used with this method must be executed. Therefore, a mathematical model will be employed using the extracted data from experiment 1 and 2.

### 7.2. Methodology

In 2.2.2 and in 2.4 it was described that the process of deriving a model for the Deep Dip method analytically is not trivial. Therefore, the approach here is that an existing model which comes close to the Deep Dip scenario will be used and modified to accurately describe the observed measurements. The mathematical model of drop spreading from Lopez et al. was introduced in subchapter 2.4. Additionally, the derivation of the model

was described and explained. Furthermore, the derived model from Chen et al. which is equation (2-30) was also introduced and will primarily be used as the starting model, to describe the maximum layer height measurements. This model describes the actual height of a drop while spreading solely through gravitational forces. This can be assumed to be the case for the observed measurements since Chen et al. delivers equation (2-31) for confirming this. A computation of the formula with the given parameters yields:

$$\lambda_l = \sqrt{\frac{\gamma_{LV}}{\rho g}} = \sqrt{\frac{0.030 \text{ N/m}}{1169 \frac{\text{kg}}{\text{m}^3} \cdot 9.81 \frac{\text{m}}{\text{s}^2}}} = 0.001617 \text{ m}$$

Where  $\gamma_{LV}$  is only an assumption since to this point no values are known. With an assumed drop radius  $R$  of 5 mm, which is half length of the build platform in y-direction, we can state that:

$$\lambda_l < R$$

Therefore, the capillary length  $\lambda_l$  is smaller than the drop radius of  $R$  and the formula (2-30) can be used.

Additionally, the more general model from Lopez et al. could be used to also describe the shape of the obtained layers and therefore try to also model the *ROC* that was measured through experiment 1 and 2, but through a lack of time, this model will not be used in this work. This more general model was described through equations (2-26 to (2-29).

Since the model from Lopez et al. and subsequently Chen et al. doesn't represent the actual physical Deep Dip scenario, the used model from Chen et al. will therefore empirically be modified to make the model fit for the measured data.

Furthermore, the experimental data which will be used, is the following dataset, where *DDD* is -2000  $\mu\text{m}$  and the BP to RV ratio is 0.0852. Here the averaged maximum layer height will be used as it was shown in subchapter 5.3 in Figure 5-2. The reason to choose this dataset was that viscosity in the Chen model shall be held constant firstly and for

a viscosity of  $448 \text{ mPa} \cdot \text{s}$  three similar datasets exist which were also complete unlike the dataset from experiment 2 where some part the data could not be measured.

As it can be seen in equation (2-30) the formula incorporates the viscosity of the liquid, the density, the gravitational acceleration as well as the volume  $V$ . Here the volume  $V$  represents the start volume of the drop. It is assumed that the start volume of the drops corresponds to the start volume of the liquid, after the build platform was drove up in the Deep Dip method. Since the start volume from the measurements are unknown, the volume must be estimated. Therefore, a analyses algorithm was iterated through each individual measurement of the dataset and for each scan the volume above the build platform was computed. An example for this can be seen in the following Figure 7-1.

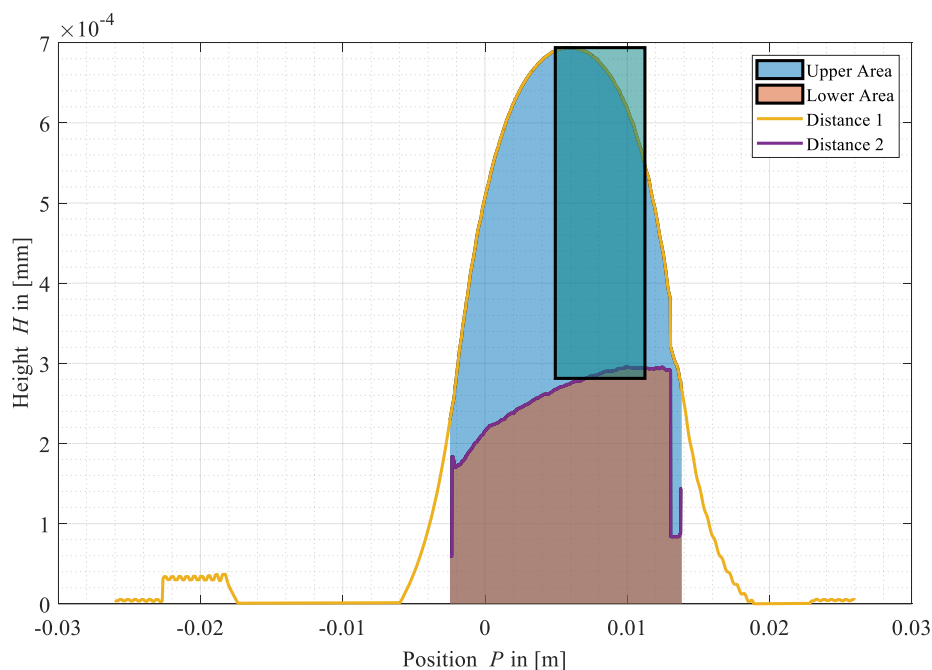


Figure 7-1: Showing an example for a volume data extraction.

In Figure 7-1, an example of the volume extraction can be seen. Here it firstly numerical integrate the area below build platform (red shaded) and then secondly numerical integrate the entire measurement above the build platform (light blue shaded). Then the lower area below the build platform was subtracted upper area to yield only the area above the build platform. To obtain the volume above the build platform, the beforehand computed area must be integrated. Here, it was assumed, that the drop above the build

platform is rotational symmetric. Additionally, the liquid drop above the build platform must be described with a mathematical formula to be integrated. As an shortcut for this integration, a new area was determined which has a rectangular shape and contains half of the same area as it was computed before which can be seen in Figure 7-1 as the dark blue shaded area. The new area can now be integrated around the y axis (dark line) with the following formula [45, p. 515]:

$$V_y = \pi \cdot \int_c^d g(y)^2 dy \quad (7-1)$$

Where  $g(y)$  is a function describing the values in the x-axis. When describing a rectangle, then the function  $g(y)$  describes a constant value  $x$  describing the rectangle width  $x_{width}$  and then the integration formula becomes:

$$V_y = \pi \cdot \int_c^d x_{width}^2 dy = \pi \cdot x_{width}^2 \int_c^d dy = \pi \cdot x_{width}^2 (d - c) \quad (7-2)$$

Where  $(d - c)$  is the actual height of the drop. It should be stated, that the found start volumes in this case are just estimations because of the simplified integration scheme but also since experiment 1 in 5.4 has showed, that especially in the beginning of a measurement the upper layer data is partially wrong or incomplete. Therefore, it is suspected, that the computed start volumes are probably underestimated.

With a known start volume, the model from Chen et. al, can now be fitted onto the used dataset. Here for the fitting process, the equation 2-30 was modified, where the exponential above the time variable  $t$  was made variable and a function of the Deep Dip Offset. Since the fitted volumes are just an estimation and an underestimation of those volumes is suspected, an additional correction factor  $k$  was added to the start volume. Therefore, the equation 2-30 becomes equation 7-3, which can be seen below.

$$h = \frac{1}{\pi} \left( \frac{\mu V \cdot k}{0.136 \rho g} \right)^{\frac{1}{4}} \cdot t^{-\alpha(DDO)} \tag{7-3}$$

Finally, the new formula will be fitted according to the chosen dataset. The extracted volume data from the dataset as well as the fitted data will be shown in the following subchapter 7.3.

### 7.3. Results

The results from the fitted mathematical model can be seen in the following figures. In Figure 7-2 the computed volumes for each scan can be found with an additional fit function, to interpolate the starting volume values. With the obtained volumes, the modified function was fitted to the experimental measured data for three different  $k$  values. The fit results for a  $k = 1$  value can be seen in Figure 7-3, for  $k = 2$  can be seen in Figure 7-4 and for a  $k = 3$  value in Figure 7-5. A comparison of the fitted alpha values as well as the rms difference between fit and measured data for all 3  $k$  values can be seen in the discussion of this chapter in subchapter 7.4.

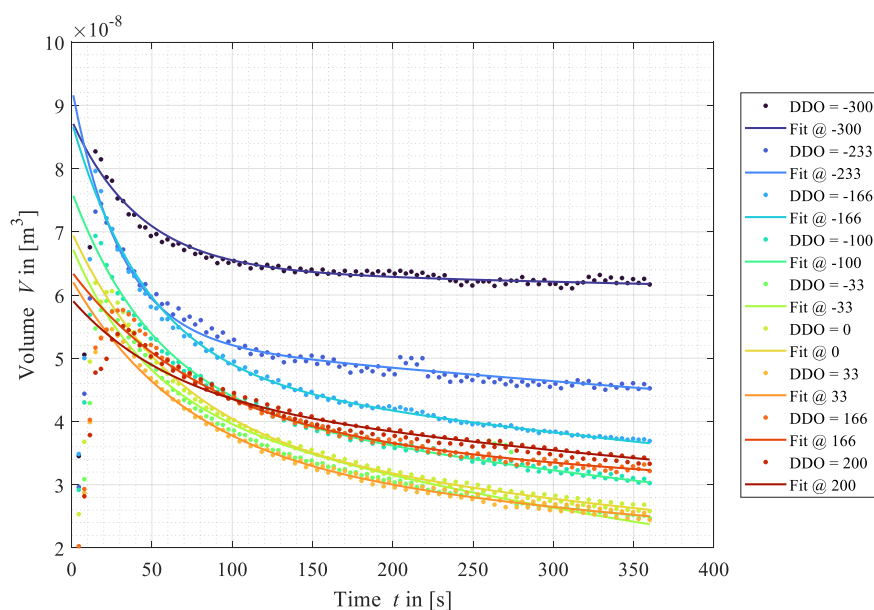
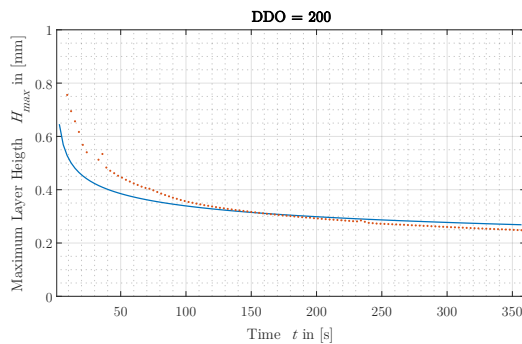
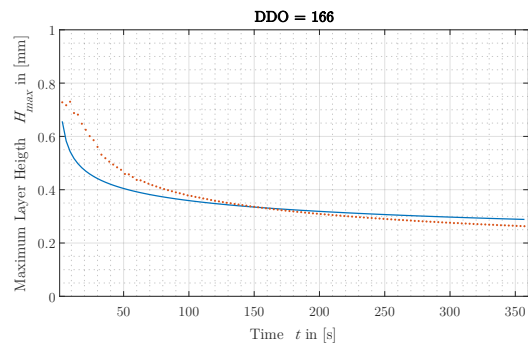


Figure 7-2 The computed volume values for each scan and for each DDO value.

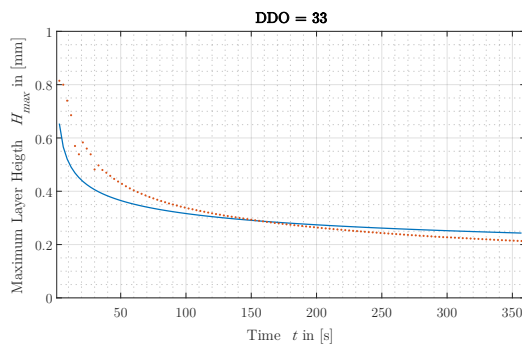
In Figure 7-2, the volume data over time for each  $DDO$  values from the  $DDD = -2000 \mu\text{m}$  and BP to RV ratio of 0.0852 is plotted. An exponential decay is decreasing the volume above the build platform. This is caused due to the downwards flow of the liquid above the build platform to the bulk liquid. This was also shown in experiment 1 in subchapter 5.3. It can be seen from the fit data that higher  $DDO$  values lead to lower initial starting volume and lower  $DDO$  values lead to a higher initial starting volume. Additionally, the exponential decay for lower  $DDO$  values is also lower compared to measurements with positive  $DDO$  values. It should be stated that again the initial volumes until 20 s measurement time are wrong since the initial layer height cannot be measured or is fragmented, since they are outside the confocal measurement range.



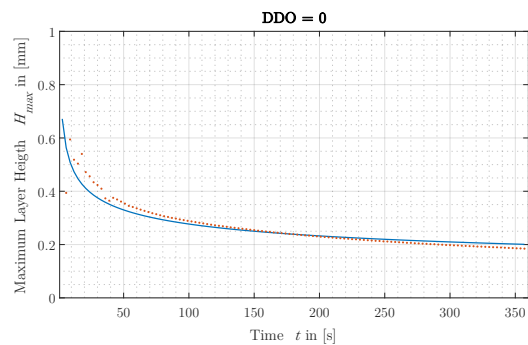
(a)



(b)



(c)



(d)

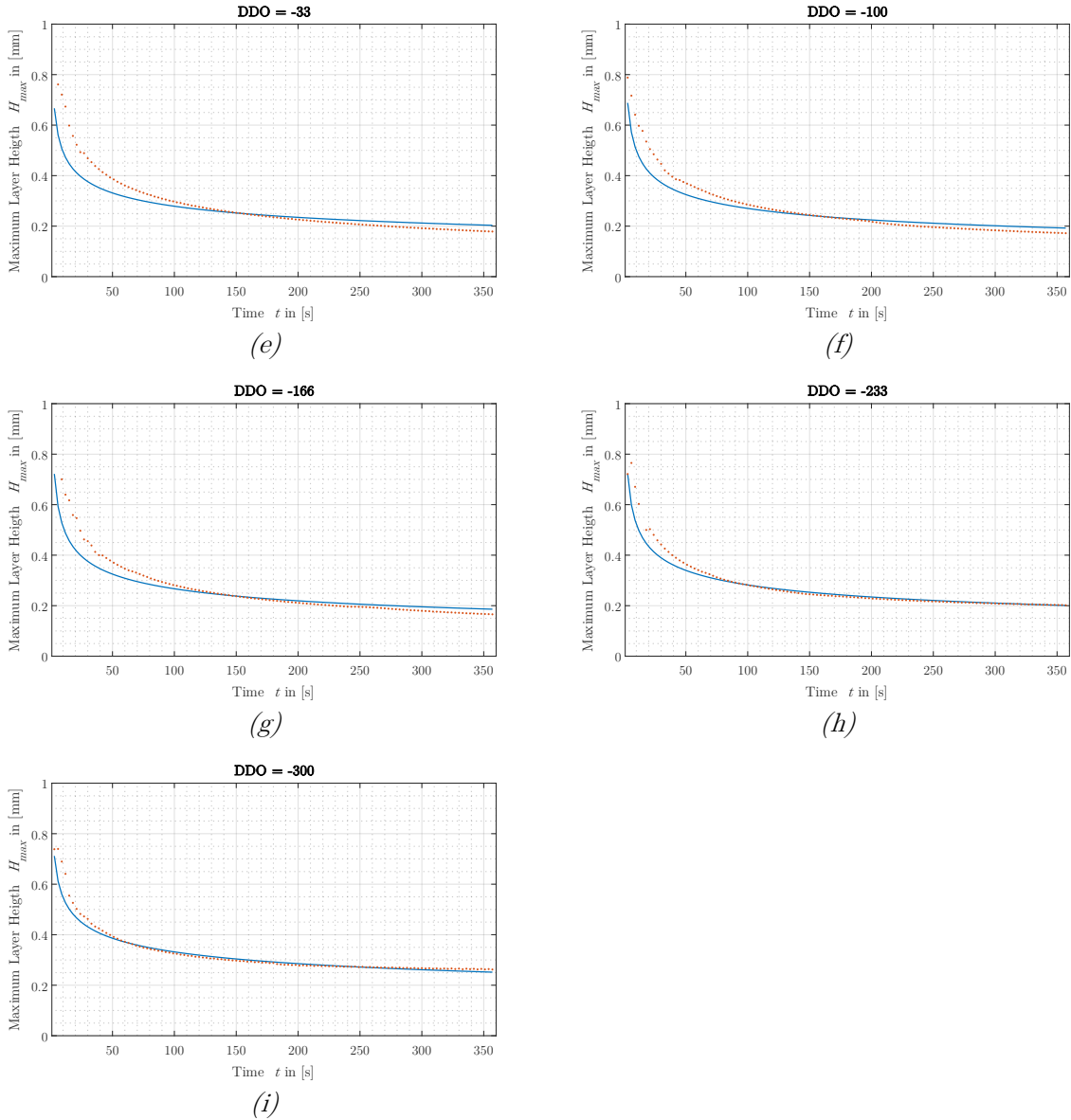
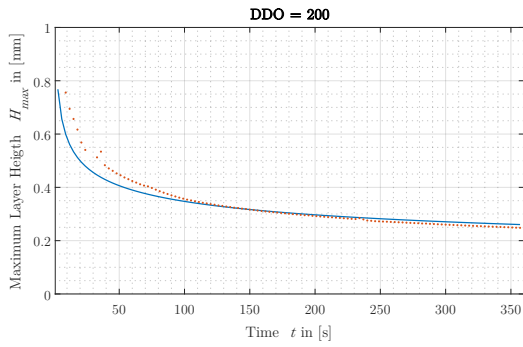
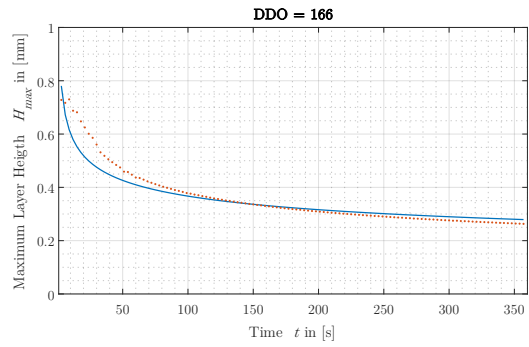


Figure 7-3: The fitted data and the measured data compared from the dataset  
 $DDD = -2000 \mu\text{m}$ , BP to RV ratio = 0.0852 and an volume correction factor  $k = 1$ .

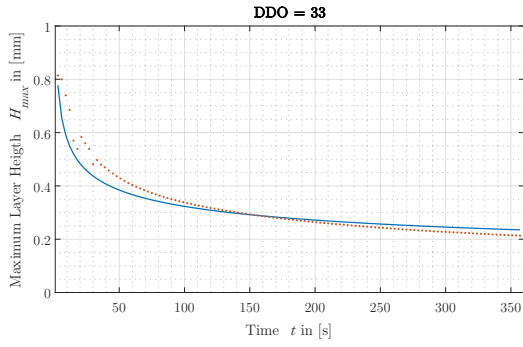
From Figure 7-3, in graphs (a) till (h) the fitted data deviates the most from the measurement data. Furthermore, more deviations can be observed in the end part. An exception is the measurement with a  $DDO$  of  $-300 \mu\text{m}$  in (i), where the fitted data fits the measured data the best. Furthermore, the fit data is in the beginning significantly smaller than the measurement data and the exponential decay is in the fit data higher than in the measured data.



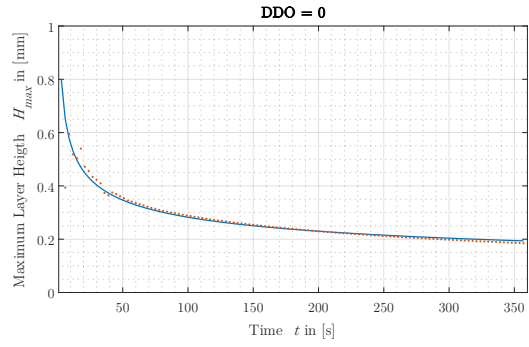
(a)



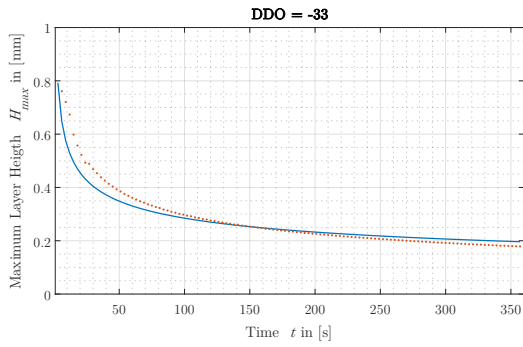
(b)



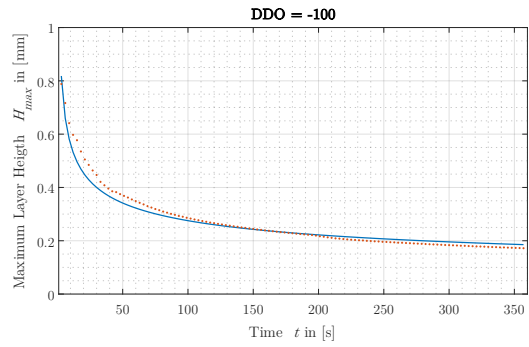
(c)



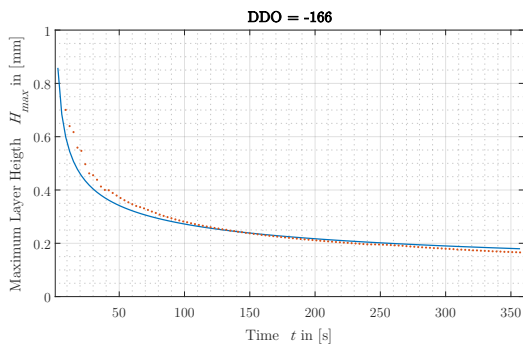
(d)



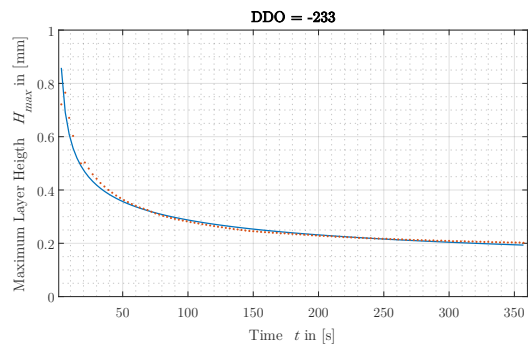
(e)



(f)



(g)



(h)

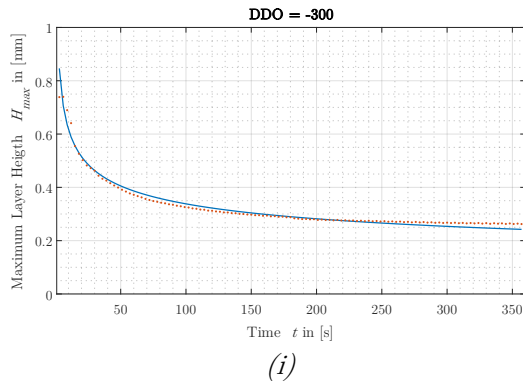
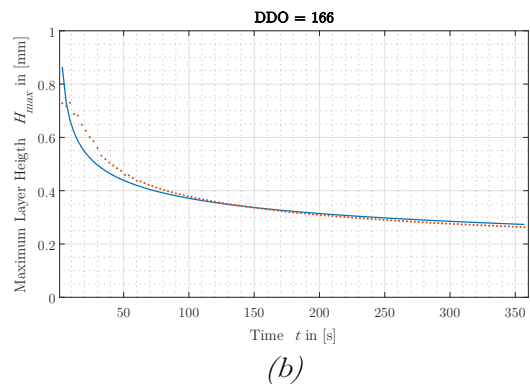
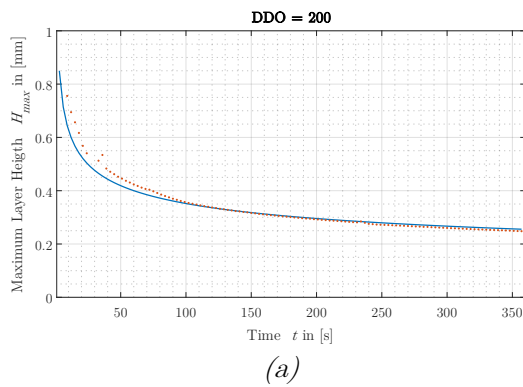
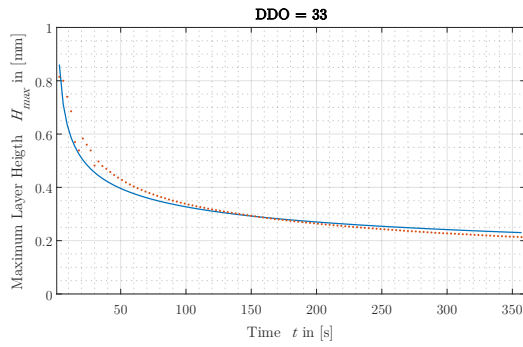


Figure 7-4: The fitted data and the measured data compared from the dataset

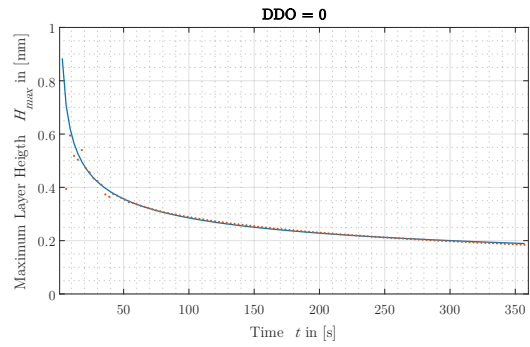
$DDD = -2000 \mu\text{m}$ , BP to RV ratio = 0.0852 and an volume correction factor  $k = 2$ .

In Figure 7-4, in graphs (a), (b), (c), (e) and (f) the fitted data deviates the most from the measurement data, especially in the beginning of the fit. Furthermore, more deviations can be observed in the end part. An exception are the measurements (d), (h) and (i) where the fitted data fits the measured data the best. Furthermore, the fit data is in the beginning significantly smaller than the measurement data and the exponential decay is in the fit data higher than in the measured data for graphs (a), (b), (c), (e) and (f).

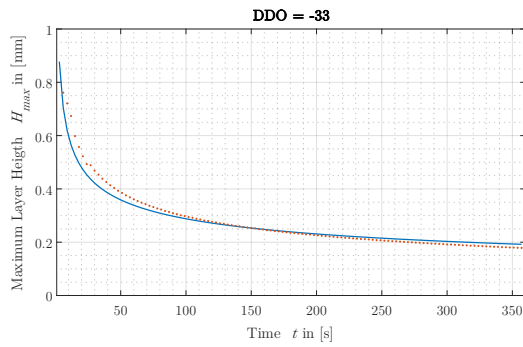




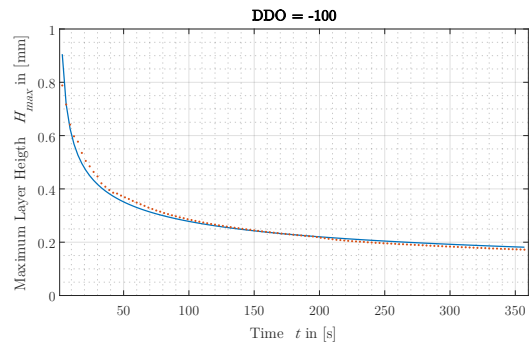
(c)



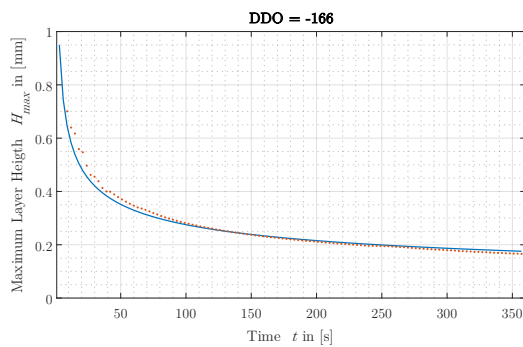
(d)



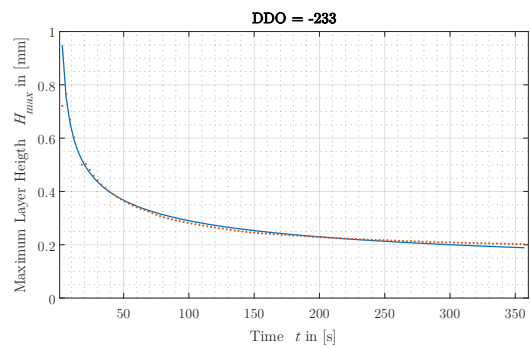
(e)



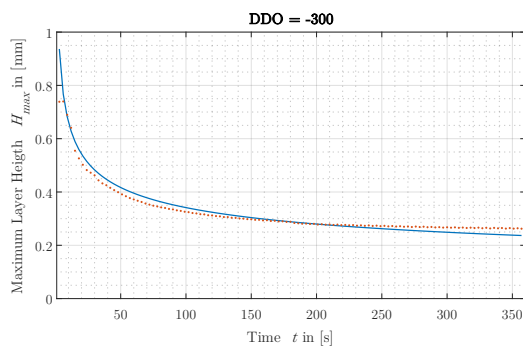
(f)



(g)



(h)



(i)

Figure 7-5: The Fitted data and the measured data compared from the dataset  
 $DDD = -2000 \mu\text{m}$ , BP to RV ratio = 0.0852 and an volume correction factor  $k = 3$ .

In Figure 7-5, like before, in graphs (a), (b), (c), (e) and (f) the fitted data deviates the most from the measurement data, especially in the beginning of the fit like before in Figure 7-4. Furthermore, smaller deviations can be observed in the end part. For the other measurement, the fit data seems to match the experimental data better. Furthermore, the fit data is in the beginning higher than the measurement data and the exponential decay in the fit data is mostly higher than in the measured data. An exception here is the graph (i), where the exponential decay of the experimental data is lower than the fit data.

#### 7.4. Discussion

The results from subchapter 7.3 shall now be discussed. The measured and computed volume data in Figure 7-2, show an exponential decay. Furthermore, the beginning of the computed volume data exhibits a not typical behaviour for an exponential decay. This was partially compensated through the established fit function through the  $k$  value. As described earlier in 7.2, the first readings into are liquid layer measurement are probably false since the first liquid layers cannot be measured without wrong confocal sensor data. Therefore, an estimation of the initial start volume may be difficult, which is the reason since for the model equation an extra factor  $k$  was incorporated. To analyse the fit data with the different  $k$  factors the alpha values from the fits were extracted and the root-mean-square of the difference between the fit data and the measured data was computed. Therefore, a comparison shall be given for the fits for each  $k$  value. The individual alpha values as well as the rms error are displayed in the following graphs from Figure 7-6 below.

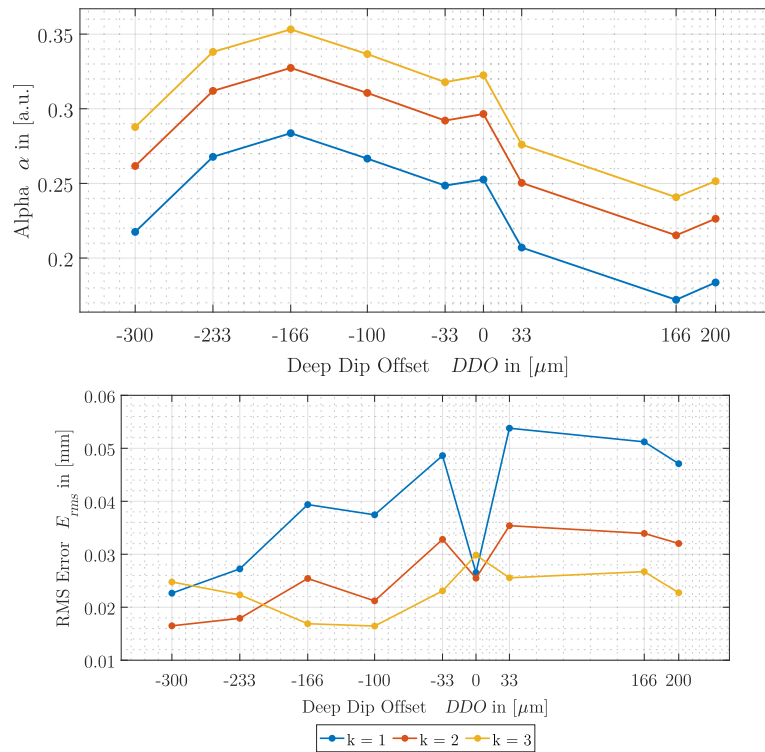


Figure 7-6: The alpha values resulting from the conducted fits in the upper graph as well as the RMS error between measurements and fit data, for each  $k$ -value.

From Figure 7-6 in the upper graph, the alpha values for each  $k$  value and for each  $DDO$  values can be seen. It can be observed that the same behavior of the alpha values can be observed, where only a scaling of the alpha values depended on the  $k$  value. This can be explained, by coming back to the presumption that was made in 7.2 where a underestimation of the initial starting volumes was suspected and confirmed with the measurements in Figure 7-2. Here an underestimation of the initial starting volumes will be compensated through the alpha variable, to match the fit closer to the measurement values. This is of course done by decreasing the alpha value which subsequently scales up the entire fit data. Therefore, when increasing the  $k$  values, then the first term of the equation (7-3 is increased and as a result the alpha value must not be decreased that much in order to match the fit data with the measurement data.

Coming to the actual behavior of the alpha curves, it can be seen that for negative  $DDO$  values from  $-300 \mu\text{m}$  to  $-166 \mu\text{m}$  the alpha values increase and subsequently decrease just to be increased again for higher positive  $DDO$  values like  $200 \mu\text{m}$ . Additionally,

it can be seen that the alpha value exhibits a bump at the curves turning point for the  $DDO$  of 0  $\mu\text{m}$ . When looking at the RMS error for the  $DDO = 0 \mu\text{m}$ , then it can be observed that for all three  $k$  values, the  $DDO$  of 0  $\mu\text{m}$  is fitted equally good. This could mean that the model can be applied good to this  $DDO$  value, which would make sense, since this is the scenario, which comes closest to the used model from Lopez et al. When comparing the overall RMS errors for the three different  $k$  values than it can be observed that the deviation is lowest for the  $k$  value of three, further indicating that the start volume was too low from the previous analysis. Furthermore, it can be stated, that the higher  $DDO$  values exhibit a higher RMS error than the lower  $DDO$  values.

All in all, the key findings regarding the mathematical model employed to the measured data shall be summarised.

- It could be observed that the initially volume values were extracted and underestimated.
- Additionally, the underestimation can be corrected with  $k$  factor which was incorporated into the model and the estimated volume was lower by a factor of 3, since here the RMS error was the lowest.
- Furthermore, if a correct starting volume can be inserted into the model, then the fitting of the alpha values yields results that match the measured layers and therefore the alpha value model can in fact be used to describe the obtained measurements.
- Also, the alpha value shows a dependency on the  $DDO$  values. From here it can be possibly differentiated between 3 different scenarios where in the first the scenario with a  $DDO$  value of 0  $\mu\text{m}$ , the used model yields independent of the  $k$  value good results (low RMS value) and therefore possibly matches the Lopez model the best. In scenario two, the  $DDO$  values are negative, meaning that this scenario differs more from the Lopez model, resulting in higher alpha values which means that the exponential decay is increased in speed. This would make sense in

a way that the liquid layer flow away from the build platform is increased since the build platform does not block the liquid layer flow as with higher  $DDO$  values. Additionally, it can be stated that in the case for positive  $DDO$  values, the exponential decay is decreased, by decreasing the alpha fit value. This fits with the observations made in experiment 1 where for higher build platform positions lower liquid flow was assumed. Furthermore, those three scenarios were already discussed before modelling the measurements when the results of experiment 1 were discussed in 5.4., indicating that adjusting the exponential from the Chen model can lead model describing the measurements from experiment one.

- The model was not tested for different  $DDD$  values and with different measurements from experiment 1 because of a lack of time.
- The model was not tested for different viscosities values and with the measurements from experiment 2 because of a lack of time.
- The model can only be called valid if it fits also experimental data with different viscosity values.

## 8. Summary and Discussion

In this work, the Deep Dip method for P $\mu$ SL printing systems was investigated. The emerging technology of P $\mu$ SL was introduced in the state of the art in 1.2 regarding the additive manufacturing of micro lenses and miniaturized SMA actuators. Here the need for research for the Deep Dip method in P $\mu$ SL systems was pointed out. Therefore, the research goals were formulated for this thesis in subchapter 1.3, including a parameter analysis in experiment 1, an investigation to the viscosity parameter in experiment 2 and the layer generation on already cured layer layers in experiment 3.

As a result, the P $\mu$ SL technology and its underlying technologies were explained in section 2.1.1 and the Deep Dip method was described in section 2.2.2 together with other recoating techniques. Here the numerical simulation of the Deep Dip Method from W. Tan et al. was discussed in more detail building the basis of this work. In the discussion it was pointed out that W. Tans simulations showed a logarithmic dependency of the average layer thickness on the viscosity as well as linear dependency of the average layer height from the build platform to resin vat ratio. Furthermore, the viscosity of the liquid photopolymers determines the layer thickness, and thinner layer thicknesses can be attained via gravity levelling with lower viscosity photopolymers

For the Deep Dip method, the rheological properties of liquids were investigated in more detail paving the way for a description of the fluid flow in this method. Especially of interest in the rheological properties is the possibility of reducing liquid viscosity by heating them up, which was utilized in the second experiment. A possible usable model for the fluid flow in the Deep Dip process from Lopez et al. was derived and explained in the subchapter 2.4. and connected to the simplified Chen model, which was used to describe the observed measurements conducted in experiment 1. Furthermore, it was shown in section 2.2.4 that the chromatic confocal measurement technique is suited for liquid photopolymer measurements. Therefore, it was chosen as the measurement tool for the conducted experiments.

In chapter 3 the concept of an P $\mu$ SL system was shown and the building of a mostly automated measurement setup, which was derived from the P $\mu$ SL concept was discussed. Here validation measurements were executed and analysed to verify the system performance on measuring liquid photopolymer layers of PR48. Besides the construction of a setup, the software system controlling the setup was explained too. With an established measurement system, the measurement methodology was explained in the chapter 4, discussing the various particulars of extracting and post processing measurement data. Therefore, a MATLAB toolbox was developed including libraries for post processing and analysing layer measurements. In chapter 5 the first experiment was conducted by generating liquid photopolymer layer under ambient conditions. Here the measurement setup was used to scan the obtained layers over time for different parameter, including the Deep Dip Offset (*DDO*), the Deep Drive Down (*DDD*) and a build platform to resin vat ratio (BP to RV) ratio. From the measurements it could be seen that an exponential decay due to liquid flow from build platform down to bulk liquid was observed. Additionally, the measurements showed a high degree of dependence on the *DDO* parameter to the obtained layer heights. Here three scenarios were concluded to describe the *DDO* influence on the exponential decay and fluid flow, where a less strong but still significant dependency on the layer height was observed from the *DDD* parameter. The relationship between the (BP to RV) ratio and the layer height was tried to be measured but ultimately failed, leaving only an unconfirmed dependency, and was finally discarded due to time restrictions. Regarding the printing process for the conceptual P $\mu$ SL system, parameter combinations for a minimal layer height under ambient conditions were found. Here the *DDO* values of -100  $\mu\text{m}$ , -233  $\mu\text{m}$  and -300  $\mu\text{m}$  yielded the smallest obtained layer heights, which was also dependent on the used *DDD* value. All in all, the smallest obtained layer height under ambient condition with PR48 were measured at 163.2  $\mu\text{m}$  for a *DDO* value of -100  $\mu\text{m}$  and a *DDD* value for -1500  $\mu\text{m}$ . Parameters for high radii of curvature, meaning the formation of flat layer, were encircled for negative *DDO* values of -233  $\mu\text{m}$  and -300  $\mu\text{m}$ . It should be mentioned that

the investigations conducted used only a scanning in y-direction, and therefore the other x-direction was not considered. Furthermore, the used build platform strongly influenced the obtained layer height. Additionally, the build platform exhibited a rectangular shape, which in fact should yield different results for the liquid layers for a scanning direction in x. Here it should be made clear, that a circular build platform would probably work best.

With experiment 2 in chapter 5 the parameter analysis was extended by an investigation with higher temperatures and therefore a lower viscosity. Therefore, the experimental setup was expanded with a heated resin vat to decrease the liquid photopolymer viscosity to  $100 \text{ mPa} \cdot \text{s}$  at  $60 \text{ }^\circ\text{C}$ . Again, validation measurements were conducted to prove the functionality of the new setup. The methodology remained mostly the same like in experiment 1 and new layers were generated and measured. The viscosity of the PR48 photopolymer was effectively reduced by a factor of four resulting measured maximum layer heights decaying exponentially, but much faster as in the previous experiment and therefore increasing steeling time. However, the obtained measured layers could not be investigated completely since the obtained minimal layer height did fall below the thickness minimal possible thickness measurement at around  $63 \text{ }\mu\text{m}$ . Nonetheless, it could be demonstrated that layer with a thickness of at least  $60 \text{ }\mu\text{m}$  can be obtained with the reduced viscosity. Additionally, the *DDO* parameters influence could be observed even at this viscosity of  $100 \text{ mPa} \cdot \text{s}$ . The layer measurement of other viscosities for different temperature was discarded because of a lack of time but could reveal more detail on the viscosity effect onto the obtained layer heights with the Deep Dip method.

Unfortunately, the planned experiment 3 where fifth layers shall be cured, and new layers should be generated on top of it was not conducted due to time issues. However, new measurement techniques were already tested, to mitigate the limit for minimal measurable layer thickness from the confocal sensor, which were observed in experiment 2. Additionally, a first setup for this was constructed, incorporating the projection system

In chapter 7, the mathematical model from Lopez et al. and Chen et al. was used and empirically modified to fit the obtained measurements from experiment 1. Here unknown metric of the initial start volume was estimated via a simplified integration scheme, which was shown in 7.2. An underestimation of the initial volumes was suspected and incorporated into the Chen Model via a correction factor  $k$ . Additionally, the exponential of the model was set as variable and therefore used for fitting the equation onto the observed experimental data for each *DDO* parameter. This revealed an exponential alpha value depending on the *DDO* value and showed the same behaviour for three different  $k$  values. For increasing  $k$  values better fit were observed confirming the initial underestimation of the start volume. The exponential alpha values showed a behaviour they could be put in context with the fluid flow and layer height decay, which was observed in experiment 1, which was shown in 7.4. Therefore, a first indication was established showing a modified Chen model can be used to describe the Deep Dip model. However, the found model should be tested independently with other datasets, to reveal if the model can predict the layer behaviour for the Deep Dip Process. It should be mentioned that the modified model was used for experimental data obtained with a rectangular shaped build platform. Here, if a circular build platform would have been used in experiment 1, then the initial start volume could maybe have been determined in a more precise way. Furthermore, with a rectangular shaped build platform and 2<sup>nd</sup> model must be employed for predicting layer height in x-direct, since another direction will probably exhibit different results.

In the following chapter 9 will discuss the upcoming strategies for further investigating the Deep Dip method for PµSL.

## 9. Outlook

Regarding the printing process for the conceptual P $\mu$ SL system, the layer generation on freshly new cured layers should be investigated. This type of layer generation can be even considered as more important, than the layer generation on a metal build platform since the printing process done layer-by-layer. Therefore, it is important to know the layer formation with the Deep Dip method in this new scenario. As a result, the planned experiment 3 should be finished.

However, it can also be seen as important to increase the effort to investigate the Deep Dip method further with the used Chen model. Here especially the effects of the viscosity in the model should be investigated in more detail.

Following, the study of the layer printing process and the investigation of the Deep Dip process, the actual P $\mu$ SL system should be build which was previously shown in 3.1. If the layer generation can be precisely controlled, then in combination with the high resolution of the projection system, a high-resolution printing system for microscale optics and actuator can be build.

## 10. References

- [1] P. J. Bártolo, *Stereolithography*. Boston, MA: Springer US, 2011.
- [2] L. Manfredi and A. Cuschieri, “Design of a 2 DOFs Mini Hollow Joint Actuated with SMA Wires,” *Materials*, vol. 11, no. 10, p. 2014, 2018, doi: 10.3390/ma11102014.
- [3] Q. Ge *et al.*, “Projection micro stereolithography based 3D printing and its applications,” *Int. J. Extrem. Manuf.*, vol. 2, no. 2, p. 22004, 2020, doi: 10.1088/2631-7990/ab8d9a.
- [4] X. Chen *et al.*, “High-Speed 3D Printing of Millimeter-Size Customized Aspheric Imaging Lenses with Sub 7 nm Surface Roughness,” *Adv. Mater.*, vol. 30, no. 18, p. 1705683, 2018, doi: 10.1002/adma.201705683.
- [5] BMF Boston Micro Fabrication, *10 μ m 3D-Druckerserie*. [Online]. Available: <https://bmf3d.com/de/10%CE%BCm-series-printers/> (accessed: Jan. 30 2022).
- [6] Y. Lu and S. Chen, “Direct write of microlens array using digital projection photopolymerization,” *Appl. Phys. Lett.*, vol. 92, no. 4, p. 41109, 2008, doi: 10.1063/1.2838751.
- [7] A. Gebhardt, “Additive Fertigungsverfahren – Additive Manufacturing und 3D-Drucken für Prototyping – Tooling – Produktion,”
- [8] Samuel Clark Ligon, Robert Liska, Jürgen Stampfl, Matthias Gurr, Rolf Mülhaupt, “Polymers for 3D printing and customized additive manufacturing,”
- [9] I. G. W. Tan, *Numerical Study On The Recoating Process In Microstereolithography*.

- 
- [10] Hari P. N. Nagarajan, Harsha A. Malshe, Karl R. Haapala, and Yayue Pan, *Environmental Performance Evaluation of a Fast Mask Image Projection Stereolithography Process Through Time and Energy Modeling*.
- [11] K. V. Wong and A. Hernandez, *A Review of Additive Manufacturing*, 2012.
- [12] K.-Y. Lee *et al.*, “Accuracy of three-dimensional printing for manufacturing replica teeth,” *Korean journal of orthodontics*, vol. 45, no. 5, pp. 217–225, 2015, doi: 10.4041/kjod.2015.45.5.217.
- [13] X. Zhou, Y. Hou, and J. Lin, “A review on the processing accuracy of two-photon polymerization,” *AIP Advances*, vol. 5, no. 3, p. 30701, 2015, doi: 10.1063/1.4916886.
- [14] E. Behroodi, H. Latifi, and F. Najafi, *A compact LED-based projection microstereolithography for producing 3D microstructures*, 2019.
- [15] R. Raman *et al.*, “High-Resolution Projection Microstereolithography for Patterning of Neovasculature,” *Advanced healthcare materials*, vol. 5, no. 5, pp. 610–619, 2016, doi: 10.1002/adhm.201500721.
- [16] J.-W. Choi, H.-C. Kim, and R. Wicker, *Multi-material stereolithography*, 2011.
- [17] Matthew Paul Alonso, *Optimization of a Light Emitting Diode Based Projection Stereolithography System and Its Applications - Thesis*. Accessed: Sep. 21 2020.
- [18] R. Holtrup, “XZEED DLP: A multi-material 3D printer using DLPT technology,”
- [19] Y.-X. Ren, R.-D. Lu, and L. Gong, *Tailoring light with a digital micromirror device*, 2015.
- [20] Dana Dudley, Walter Duncan, John Slaughter, *Emerging Digital Micromirror Device (DMD) Application*.
- [21] Thomas Hafkamp, Gregor van Baarsy, Bram de Jager, and Pascal Etman, “A trade-off analysis of recoating methods for vat photopolymerization of ceramics,”

- [22] Jaime Lopez, Clarence A. Miller, “Spreading Kinetics of Liquid Drops on Solids,”
- [23] H. Narahara, H. Suzuki and M. Suga, *Detection of uneven flatness on Liquid Surface*.
- [24] A. K. Ruprecht *et al.*, “Confocal micro-optical distance sensor: principle and design,” in *Optical Measurement Systems for Industrial Inspection IV*, Munich, Germany, 2005, p. 128.
- [25] G. Cox, “Biological confocal microscopy,” *Materials Today*, vol. 5, no. 3, pp. 34–41, 2002, doi: 10.1016/S1369-7021(02)05329-4.
- [26] Antonin Miks, Jiri Novak, Pavel Novak, *Analysis of method for measuring thickness of Analysis of method for measuring thickness plane-parallel plates and lenses using chromatic confocal sensor*, 2010.
- [27] A. Heinrich and M. Rank, “3D Printing of Optics,” in *3D Printing of Optics*, A. Heinrich and M. Rank, Eds.: SPIE, 2018.
- [28] T. J. Trout, J. J. Schmiege, W. J. Gambogi, and A. M. Weber, “Optical Photopolymers: Design and Applications,” *Adv. Mater.*, vol. 10, no. 15, pp. 1219–1224, 1998, doi: 10.1002/(SICI)1521-4095(199810)10:15<1219::AID-ADMA1219>3.0.CO;2-D.
- [29] Ameya Shankar Limaye, “Multi-Objective Process Planning Method For Mask Projection Stereolithography - PhD dissertation,” Dec. 2007.
- [30] P. F. Jacobs, “Fundamentals of Stereolithography,”
- [31] A. K. O'Brien and C. N. Bowman, *Modeling the Effect of Oxygen on Photopolymerization Kinetics*, 2006.
- [32] K. Studer, C. Decker, E. Beck, and R. Schwalm, *Overcoming oxygen inhibition in UV-curing of acrylate coatings by carbon dioxide inerting, Part I*, 2003.
- [33] V. Kumaran, *Fundamentals of Rheology: Lecture notes (04 Jan)*. [Online]. Available: <https://physics.iitm.ac.in/~compflu/school.html>

- [34] *Reynolds Number*. [Online]. Available: <https://www.grc.nasa.gov/www/BGH/reynolds.html> (accessed: Jan. 20 2022).
- [35] Wikipedia and Dr. Gary Settles, *Turbulence*. [Online]. Available: <https://en.wikipedia.org/w/index.php?title=Turbulence&oldid=1062734404> (accessed: Sep. 1 2022).
- [36] Prof. Dick K. P. Yue, *Marine Hydrodynamics (13.021) Lecture 3*, 2005. [Online]. Available: <https://ocw.mit.edu/courses/mechanical-engineering/2-20-marine-hydrodynamics-13-021-spring-2005/>
- [37] R. B. Bird, W. E. Stewart, and E. N. Lightfoot, *Transport phenomena*. New York: John Wiley & sons inc, 2007.
- [38] tec-science, *Herleitung der Navier-Stokes-Gleichungen - tec-science*. [Online]. Available: <https://www.tec-science.com/de/mechanik/gase-und-fluessigkeiten/navier-stokes-gleichungen/> (accessed: Jan. 21 2022).
- [39] M. Bourne, *9. Average Value of a Function by Integration*. [Online]. Available: <https://www.intmath.com/applications-integration/9-average-value-function.php> (accessed: Jan. 21 2022).
- [40] C.A. Miller and E. Ruckenstein, “The origin of flow during wetting of solids,” *Journal of Colloid and Interface Science*, vol. 48, no. 3, pp. 368–373, 1974, doi: 10.1016/0021-9797(74)90179-9.
- [41] *Gamma Function -- from Wolfram MathWorld*. [Online]. Available: <https://mathworld.wolfram.com/GammaFunction.html> (accessed: Jan. 16 2022).
- [42] Are Mjaavatten, *Curvature of a 1D curve in a 2D or 3D space*. [Online]. Available: <https://www.mathworks.com/matlabcentral/fileexchange/69452-curvature-of-a-1d-curve-in-a-2d-or-3d-space> (accessed: Jan. 28 2022).

- 
- [43] R. Paschotta, *Abbe Number*. [Online]. Available: [https://www.rp-photonics.com/abbe\\_number.html](https://www.rp-photonics.com/abbe_number.html) (accessed: Feb. 1 2022.026Z).
- [44] False, *DS18B20 Programmable Resolution 1-Wire Digital Thermometer / Maxim Integrated*. [Online]. Available: <https://www.maximintegrated.com/en/products/sensors/DS18B20.html> (accessed: Feb. 1 2022.412Z).
- [45] L. Papula, *Mathematik für Ingenieure und Naturwissenschaftler Band 1*. Wiesbaden: Springer Fachmedien Wiesbaden, 2014.

## 11. Table of Figures

- Figure 1-1: The increasing number of publications to a search in Web of Science platform for the keywords "projection micro stereolithography,", "PμSL", "P μ SL", "projection microsterolithography" and "Stereolithography DLP". 9
- Figure 1-2: A miniaturized actuator using wires made out of shape memory alloys (SMA) [1, p. 6]. 11
- Figure 1-3: The 3D printed aspheric lens with a diameter of 5 mm on top of a quartz substrate [2, p. 4]. 13
- Figure 1-4: A micro-lens array printed with a PμSL system. All lenses here were manufactured parallel [6, p. 92]. 14
- Figure 1-5: A micropump made with PμSL combined with traditional microsystem fabrication systems [4, p. 105]. 14
- Figure 1-6: The simulation scenario as described in W. Tan's numerical study. A curved layer can be seen on top of the build platform. The red area represents air and the yellow area environment the liquid [9]. 16
- Figure 1-7: The three planned consecutive experiments, formulating the goal for this work. 16
- Figure 2-1: Principle of the FDM technique. An extruder moves above a build platform, melting and extruding a thermoplastic on top of the previous layer. As support, dissolvable thermoplastics can be used and extruded through a second nozzle. The build material is stored in spools[12]. 18
- Figure 2-2: The principle of an SLA system, where a UV-Laser source is deflected by 2 galvanometers. The galvanometers are mirrors, which will be rotated to reflect the laser beam into any 2D point into the liquid

photopolymer surface. Additionally, scan lenses are usually employed to correct the length difference of the laser beam for different lateral positions.	19
Figure 2-3: Components of a P $\mu$ SL system include a UV-LED, Digital Mirror Device (DMD), Optical System, Beam Splitter, Camera System, and Photopolymer.	20
Figure 2-4: The working principle of a single DMD mirror element.	22
Figure 2-5: Two DMD mirror units are shown in more detail, sitting on top of the CMOS substrate [19].	23
Figure 2-6: Showing different self-metered, free surface recoating systems and their working principles [21].	25
Figure 2-7: The states of the deep dip procedure generate new layers on top of a freshly cured structure inside of a photopolymer reservoir. The movement is created by attaching the build platform to a stage.	27
Figure 2-8: The BP's final position can be either above (left-hand-side) or below (right-hand-side) to the initial liquid surface height (blue dashed line) leading to different flow behaviour of the liquid.	28
Figure 2-9: The obtained results from the simulation with four different viscosities each for two BP to RV ratios. The average layer height is plotted over time for a maximum settling time of 30s.	29
Figure 2-10: Dependency of the numerical obtained average layer thickness on the liquid viscosity [9].	30
Figure 2-11: Dependency of the numerical average layer thickness from the ratio between the build platform and resin vat sizes for a viscosity of 0.1 mPas [9].	31
Figure 2-12: Dependency of the settling time from the ratio between the build platform and resin vat sizes for a viscosity of 0.1 mPas [9].	31

- Figure 2-13: The working principle of the confocal measurement principle. A light source is focused onto an object within the focal plane and is reflected from it. Only the light that is reflected precisely at the focal plane will not be blocked by the pinhole and reaches the detector [24]. 33
- Figure 2-14: Showing on the left how mechanical depth scanning can be achieved by moving the focus position up and down compared to the chromatic approach where the depth information is already encoded into the chromatic aberration from a lens. 34
- Figure 2-15: Showing the full spectrum of a typical white light led, which can be used in a chromatic confocal sensor. The spectrum here can range from 380 nm to 780 nm. When a chromatic confocal sensor measures a single transparent layer, two peaks will appear on the spectrometer. Their intensity will be within the intensity range of the white light source. Since peak 1 appears at a shorter wavelength than peak 2, peak one must be closer to the sensor than peak 2. Applying this principle and compensating for the dispersion of the transparent layer, one can calculate the geometric thickness of the layer. 35
- Figure 2-16: IFC2461 control unit (right-hand-side) and IFS2405 optical head (left-hand-side). 36
- Figure 2-17: The working curve for the resin HS6603, showing  $Cd$  in relationship to the critical energy dose [24, p. 21]. 38
- Figure 2-18: The Schlieren imaging technique shows the airflow generated by the heat of a candle and the transition from laminar to turbulent airflow [34]. 41
- Figure 2-19: Showing the scenario described by Lopez. et al. were a drop in an initial wetted state and spreading across an infinite horizontal surface. 44

Figure 2-20: Showing the scenario for the Deep Dip method where a drop of liquid is created on top of a horizontal build platform but, the liquid on the top is still connected to the bulk liquid of the resin vat.	44
Figure 3-1: The influence of specific parameters on the layer height and the layer radius of curvature (ROC) for the Deep Dip procedure.	54
Figure 3-2: The conceptual P $\mu$ SL system.	55
Figure 3-3: Complete assembly of the experimental setup, with the confocal chromatic sensor pointing next to the build platform.	57
Figure 3-4: Aluminium metal strip BP attached to the GTS30V functioning as the z-axis.	57
Figure 3-5: IFS2405 optical head attached to the XMS50S stages for the x-y-axis via an FDM 3D printed adapter.	57
Figure 3-6: (a) Showing the 3D printed RV. (b) The platform. (c) Assembly of resin vat, build platform and adaptor for the linos rails.	59
Figure 3-7: Complete real assembly of the experimental setup.	60
Figure 3-8: Software system programmed in previous work which is comprised of different classes to control the measurement setup.	61
Figure 3-9: Setup for the z-stage validation.	62
Figure 3-10: Showing the position differences for 1 $\mu$ m, 10 $\mu$ m and 100 $\mu$ m set values for 3 different velocities.	63
Figure 3-11: Measurement Setup for the confocal test where the confocal sensor in black is above the bluish PR48 liquid. The white dot is the measurement spot	64
Figure 3-12: Spectral signal for a PR48 drop on an aluminium surface.	64
Figure 3-13: Showing the spectral signal for three different layer heights, where in the last spectral signal, the 2 Peaks are not distinguishable.	65
Figure 4-1: The definition of the DDD and the DDO parameters.	67

Figure 4-2: The BP to RV ratio is simply the ration between the BP length and RV length in y-direction	67
Figure 4-3: RV filled with liquid polymer and the BP with the confocal sensor on top. On the left-hand side the dot scan is shown, in the centre the line scan is show and on the right-hand side the mapping procedure is shown. A green dot is the start point of a movement path and a red dot is the end point. The blue lines correspond to the path.	69
Figure 4-4: Showing the first scans of a line measurement where the layer surface is shown. The Y-axis displays the layer height and the x-axis the scan position.	71
Figure 4-5: Showing a layer measurement where the layers appear flipped horizontally.	71
Figure 4-6: Showing the flipped data, which exhibits a undefined shit in the data.	72
Figure 4-7: The final dataset after filtering, flipping, and shifting the layer surface and build platform data.	73
Figure 4-8: Showing the saved coordinates, raw data and post processed data.	73
Figure 4-9: Overview of the data post-processing.	74
Figure 4-10: Showing the post processed layer measurement, where the middle point of the build platform is marked with a black line and its outer edges are marked with the dshed lines.	75
Figure 4-11: Showing the final layer height obtained from the sensor for different positions. The solid black line represents the build platform centre and the dashed lines the margin relative to the centre line defining the grey shaded analysis area.	75
Figure 4-12: Showing the obtained maximum layer height form the analyses algorithm over time.	76
Figure 4-13: The principle of the circle fitting for the radius of curvature analysis.	77

- Figure 4-14: The radius of curvature vector of a single measured layer. **Fehler!**  
**Textmarke nicht definiert.**
- Figure 4-15: Showing the average radius of curvature for each scan. (btw this graphic is wrong and I will change it. ROC Should be increasing) 78
- Figure 5-1: A levelling measurement, where the peak-to-peak value of 200  $\mu\text{m}$  is set ignoring artifacts in the measurement. 81
- Figure 5-2: Layer measurements showing the mean and standard deviation of  $Hmax$ (in blue) and of the normalized  $ROCnorm$ (in red) for the individual DDO values, DDD = -2000  $\mu\text{m}$ , BP to RV ratio = 0.0852. 84
- Figure 5-3: Layer measurements showing the mean and standard deviation of  $Hmax$ (in blue) and of the normalized  $ROCnorm$ (in red) for the individual DDO values, DDD = -1500  $\mu\text{m}$ , BP to RV ratio = 0.0852. 87
- Figure 5-4: Layer measurements showing the mean and standard deviation of  $Hmax$ (in blue) and of the normalized  $ROCnorm$ (in red) for the individual DDO values, DDD = -2500  $\mu\text{m}$ , BP to RV ratio = 0.0852. 89
- Figure 5-5: The mean values of the  $Hmax$  on the right-hand side and the mean values for  $ROCnorm$  on the left-hand side for each DDO value and DDD value. BP to RV ratio was 0.0852 90
- Figure 5-6: Showing the decay in layer height in the upper part of the layer measurement (a) and showing the increase in surface height in the lower part of the measurement (b). 92
- Figure 5-7: Measurements with wrong readings in the beginning regarding upper layer and lower build platform data. Here scan 1 to 4 are shown. 93
- Figure 5-8: Showing the maximum layer height for the last scan for each DDO value. 94

Figure 5-9: Showing the dependency of the minimal layer thickness and the corresponding DDO values in dependency on the DDD values	95
Figure 5-10: Showing a layer measurement with the parameters DDD = -2500, DDO = -100 um	97
Figure 5-11: Showing the same dataset as in Figure 5-10, but with separated scan directions.	98
Figure 5-12: Showing the build platform data from Figure 5-11.	99
Figure 5-13: The Thickness dataset for a layer measurement is shown for a DDD = -2500 and DDO = -300.	101
Figure 5-14: Showing the slices for four different points in time: (a) 30 s, (b) 150 s, (c) 300 s and (d) 360 s for all 3 DDD values.	102
Figure 5-15: The maximum layer height averaged from all DDO values over time for each DDO dataset.	103
Figure 6-1: A slice through the heated resin vat showing its components	107
Figure 6-2: The control circuit for the heated resin vat.	108
Figure 6-3: The block diagram of a PID system.	109
Figure 6-4: Showing the decrease of the Viscosity of PR48 depending on the temperature.	112
Figure 6-5: The refractive indices for three different wavelengths and the computed Abbe number	113
Figure 6-6: The measured temperature values for the 6 used temperature sensors.	115
Figure 6-7: The measurement errors in dependency of the temperature for the used DS18B20 sensors which will be placed in the liquid resin vat.	116
Figure 6-8: Showing the final temperature test with a set temperature of 60°C (orange) and the measured temperature in blue.	117
Figure 6-9: Showing the Sensor configuration of temperatures Sensor 1 and 2 from the top in (a) and from the side in (b)	118

Figure 6-10: Showing the Configuration of the sensor 1 and the 3 measurements positions.	119
Figure 6-11: Temperature measurements at three different points in the heated resin vats measurement, where (a) is for $P_1$ , (b) for $P_2$ and (c) for $P_3$ .	119
Figure 6-12: Showing various influences on the temperature measurements.	121
Figure 6-13: The layer measurements showing the Maximum Layer height $H_{..}$ and the normalized radius of curvature for each DDO values, with a DDD value of $-2000 \text{ um}$ and an BP to RV ratio of..	123
Figure 6-14: Showing the thickness dataset for a measurement with $DDO = -33 \text{ um}$ and $DDD = -2000 \text{ um}$ .	124
Figure 6-15: The last obtained maximum layer heights are shown with the mean values as a dot and solid line and the standard deviation as a shaded area for each DDO value.	125
Figure 7-1 The computed volume values for each scan and for each DDO value.	132
Figure 7-2: The Fitted data and the measured data compared from the dataset $DDD = -2000 \text{ um}$ , BP to RV ratio = 0.0852 and an volume correction factor $k = 1$ .	134
Figure 7-3: The Fitted data and the measured data compared from the dataset $DDD = -2000 \text{ um}$ , BP to RV ratio = 0.0852 and an volume correction factor $k = 2$ .	136
Figure 7-4: The Fitted data and the measured data compared from the dataset $DDD = -2000 \text{ um}$ , BP to RV ratio = 0.0852 and an volume correction factor $k = 3$ .	137
Figure 7-5: The alpha values resulting from the conducted fits in the upper graph as well as the RMS error between measurements and fit data, for each k-value.	139

# Appendices

## Specifications - Confocal Sensor - ICF2461

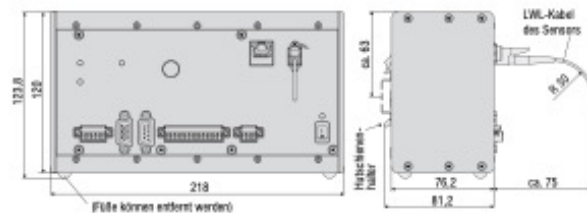
Modell		ICF2461	ICF2461MP
	Ethernet / EtherCAT		1 nm
Auflösung	RS422		18 bit
	Analog		16 bit leschbar
Messrate		stufenlos einstellbar von 100 Hz bis 25 kHz	
Linearität		typ. < ±0,025 % d.M. (Sensorabhängig)	
Mehrschichtmessung		1 Schicht	5 Schichten
Lichtquelle		interne weiße LED	
Anzahl Kennlinien		Ablage von bis zu 20 Kennlinien verschiedener Sensoren pro Kanal. Auswahl über Tabelle im Menü	
Zulässiges Fremdlicht <sup>1)</sup>		30.000 lx	
Synchronisation		ja	
Versorgungsspannung		24 VDC ± 15 %	
Leistungsaufnahme		ca. 10 W	
Signaleingang		Sync-In / Trig-In; 3 x Encoder (A, B, Index)	
Digitale Schnittstelle		Ethernet; EtherCAT; RS422; PROFINET <sup>2)</sup> ; EtherNet/IP <sup>2)</sup>	
Analogausgang		Strom: 4 ... 20 mA; Spannung: 0 ... 10 V / -10 ... +10 V (16 bit D/A Wandler)	
Schaltausgang		Fehler1-Out, Fehler2-Out	
Digitalausgang		Sync-Out	
Anschluss	optisch	steckbarer Lichtwellenleiter über E2000-Buchse, Länge 2 m ... 50 m, min. Biegeradius 30 mm	
	elektrisch	3-polige Versorgungsklemmleiste; Encoderanschluss (15-polig, HD-Sub-Buchse, max. Kabellänge 3 m); RS422-Anschlussbuchse (8-polig, Sub-D, max. Kabellänge 30 m); 3-polige Ausgangsklemmleiste (max. Kabellänge 30 m); 12-polige I/O Klemmleiste (max. Kabellänge 30 m); RJ45-Buchse für Ethernet / EtherCAT (max. Kabellänge 100 m)	
Montage		frei stehend, Hutschienenmontage	
Temperaturbereich	Lagerung	-20 ... +70 °C	
	Betrieb	+5 ... +50 °C	
Schock (DIN EN 60068-2-27)		15g / 6 ms in XYZ-Achse, je 1000 Schocks	
Vibration (DIN EN 60068-2-6)		2 g / 20 ... 500 Hz in XYZ-Achse, je 10 Zyklen	
Schutzart (DIN EN 60529)		IP40	
Material		Aluminium	
Gewicht		ca. 2,2 kg	
Kompatibilität		kompatibel mit allen confocal/DT-Sensoren	
Anzahl Messkanäle		1	
Bedien- und Anzeigeelemente		Ein/Aus-Wippschalter; Multifunktionstaste (Dunkelabgleich sowie Reset auf Werkseinstellung nach 10 s); 4x LED für Intensity, Range, Status und Versorgungsspannung	
Besondere Merkmale		besonders lichtstark	

d.M. = des Messbereichs

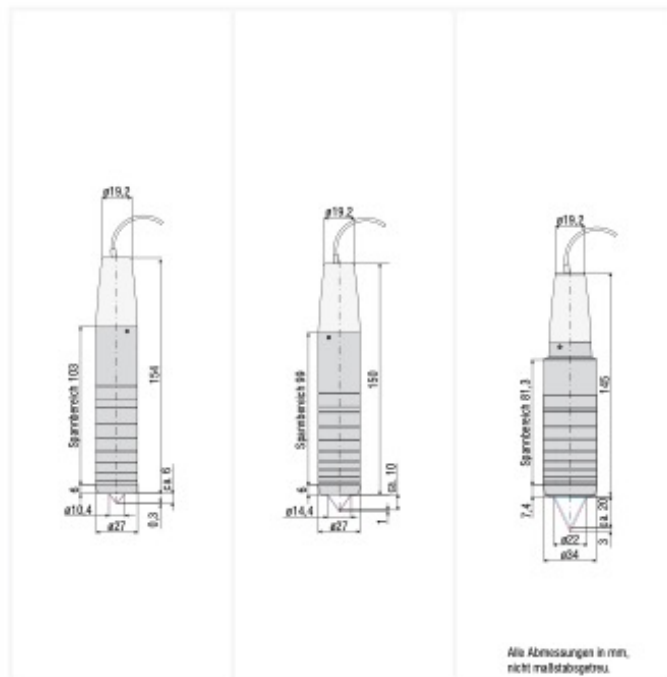
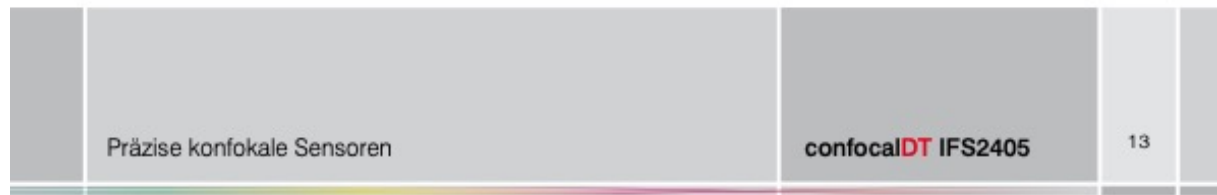
<sup>1)</sup> Lichtart: G4Hlampe

<sup>2)</sup> Anbindung über Schnittstellenmodul (siehe Zubehör)

Controller ICF2461



# Specifications - Confocal Optical Head – IFS2405-1



Modell		IFS2405-0,3	IFS2405-1	IFS2405-3
Messbereich		0,3 mm	1 mm	3 mm
Messbereichsanfang	ca.	6 mm	10 mm	20 mm
Auflösung	statisch <sup>1)</sup>	4 nm	28 nm	60 nm
	dynamisch <sup>2)</sup>	20 nm	52 nm	126 nm
Linearität <sup>3)</sup>	bei Weg- und Abstandsmessung	< ±0,15 µm	< ±0,25 µm	< ±0,75 µm
	bei Dickenmessung	< ±0,3 µm	< ±0,5 µm	< ±1,5 µm
Lichtpunktdurchmesser		6 µm	8 µm	9 µm
Max. Verkipfung <sup>4)</sup>		±34°	±30°	±24°
Numerische Apertur (NA)		0,60	0,55	0,45
Mindestdicke Messobjekt <sup>5)</sup>		0,015 mm	0,05 mm	0,15 mm
Anschluss		Steckbarer Lichtwellenleiter über FC Buchse; Standardlänge 3 m; Verlängerung bis 50 m; Biegeradius: statisch 30 mm, dynamisch 40 mm		
Montage		Radialklemmung, Montageadapter (siehe Zubehör)		
Temperaturbereich	Lagerung	-20 ... +70°C		
	Betrieb	+5 ... +70°C		
Schock (DIN EN 60068-2-27)		15 g / 6 ms in XY-Achse, je 1000 Schocks		
Vibration (DIN EN 60068-2-6)		2 g / 20 ... 500 Hz in XY-Achse, je 10 Zyklen		
Schutzart (DIN EN 60529)		IP64 (frontseitig)		
Material		Aluminiumgehäuse, Glaslinsen		
Gewicht		ca. 140 g	ca. 125 g	ca. 225 g

<sup>1)</sup> Gemittelt über 512 Werte, bei 1 kHz, in Messbereichsmitte auf Prüfglas

<sup>2)</sup> RMS Rauschen bezogen auf Messbereichsmitte (1 kHz)

<sup>3)</sup> Alle Daten ausgehend von konstanter Raumtemperatur (25 ± 1 °C) bei Messung auf planparalleles Prüfglas; bei anderen Messobjekten können die Daten abweichen

<sup>4)</sup> Maximale Verkipfung des Sensors, bis zu der auf spiegelnden Oberflächen ein verwertbares Signal erzielt werden kann, wobei die Genauigkeit zu den Grenzwerten abnimmt

<sup>5)</sup> Glasscheibe mit Brechungsindex n = 1,5 über den gesamten Messbereich. In der Messbereichsmitte können auch dünnere Schichten gemessen werden.

# Specifications – Stage - XMS-50S

## XM-S Series

## Ultra-Precision Linear Motor Stages

### 3.2 Mechanical Specifications



	XMS-S	XML-S
Travel range (mm)	50, 100, 160	210, 350
Minimum Incremental Motion, linear <sup>(1)</sup> ( <sup>2)</sup> (with XPS-DRV02 Drive)	0.01	0.01
Minimum Incremental Motion, linear <sup>(1)</sup> ( <sup>2)</sup> (with XPS-DRV02P Drive Module)	0.003	0.003
Minimum Incremental Motion, linear <sup>(1)</sup> ( <sup>2)</sup> (with XPS-DRV02L Drive Module)	0.001	0.001
Uni-directional repeatability, guaranteed <sup>(1)</sup> ( <sup>4)</sup> (μm)	0.05	0.05
Bi-directional repeatability, guaranteed <sup>(1)</sup> ( <sup>4)</sup> (μm)	0.08 or ±0.04	0.08 or ±0.04
On-axis accuracy, guaranteed <sup>(1)</sup> ( <sup>4)</sup> (μm)	1.5 or ±0.75	3 or ±1.5
Maximum speed <sup>(5)</sup> (mm/s)	300	300
Maximum acceleration <sup>(5)</sup> (m/s <sup>2</sup> )	5	5
Max. force (cont.) <sup>(5)</sup> (N)	16	37
Load capacity, horizontal (N)	100	300
Straightness, flatness, guaranteed <sup>(1)</sup> ( <sup>2)</sup> (μm)	1.5 or ±0.75	3 or ±1.5
Pitch, guaranteed <sup>(1)</sup> ( <sup>2)</sup> ( <sup>4)</sup> (μrad) <sup>(3)</sup>	50 or ±25	100 or ±50
Yaw, guaranteed <sup>(1)</sup> ( <sup>2)</sup> ( <sup>4)</sup> (μrad) <sup>(3)</sup>	50 or ±25	100 or ±50
MTBF (h)	20,000	20,000

<sup>1)</sup> For the definition of Typical and Guaranteed specifications see "Motion Basics Terminology & Standards" Tutorial at [www.newport.com](http://www.newport.com)

<sup>2)</sup> Middle 80% of travel.

<sup>3)</sup> To obtain arcsec units, divide μrad value by 4.8.

<sup>4)</sup> Requires operation in a controlled environment to achieve specification.

<sup>5)</sup> Maximum value is driver dependent. Contact Newport for additional information.

### CAUTION

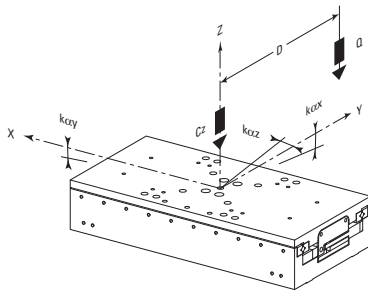


To reach specifications stated, stages must be fixed on a plane surface with a flatness of 5 μm.

### 3.3 Load Characteristics and Stiffness

#### Normal Load Capacity (Cz)

Maximum load a stage can move while maintaining specifications.



	XMS50	XMS100	XMS160	XML210	XML350
Cz, Normal centered load capacity (N)	100	100	100	300	300
kcx, Compliance in roll (μrad/Nm)	3.5	2.0	1.5	0.5	0.1
kcy, Compliance in pitch (μrad/Nm)	6.0	2.5	2.0	2.0	0.7
kcz, Compliance in yaw (μrad/Nm)	8.0	3.5	2.0	1.0	0.2
a, Construction parameter (mm)	109	109	109	155	155
Q, Off-center load	$Q \leq Cz \div (1 + D/a)$				
where D = Cantilever distance in mm					

### 3.4 Stage Weights

The stage weights indicated below do not include the cables.

	Mass [lb (kg)]	
	Stage	Carriage Mcar
XMS50-S	5.5 (2.5)	2.6 (1.2)
XMS100-S	7.7 (3.5)	4.0 (1.8)
XMS160-S	9.9 (4.5)	5.1 (2.3)
XML210-S	28.7 (13.0)	16.8 (7.6)
XML350-S	48.5 (22.0)	26.0 (11.8)

# Specifications – Stage- GTS30V



## GTS-V High-Precision Vertical Linear Stages

### Design Details

- **Base Material** High-strength Anodized Aluminum
- **Bearings** Anti-creep crossed roller bearings/recirculating ball bearing
- **Drive Mechanism** Precision ground lead screw, gravity preloaded nut
- **Drive Screw Pitch** 1 mm
- **Feedback** Linear steel scale, 20  $\mu\text{m}$  signal period, 0.05  $\mu\text{m}$  resolution, RS-422 differential output or motor mounted rotary encoder in the CC version
- **Limit Switches** Optical
- **Origin** Optical, located 5 mm from lower position travel limit
- **Drive Type** DC Servo
- **Cable Length** 3 m (included)



### Specifications

	GTS30V	GTS70VCC Rotary Encoder	GTS70V Linear Encoder
Travel Range (mm) <sup>1)</sup>	30	70	70
Minimum Incremental Motion ( $\mu\text{m}$ )	0.1	0.25	0.1
Bi-directional Repeatability ( $\mu\text{m}$ )	$\pm 0.1$	$\pm 0.5$	$\pm 0.2$
Accuracy ( $\mu\text{m}$ )	$\pm 0.75$	$\pm 1.75$	$\pm 1$
Maximum Speed (mm/s)	10	5 <sup>2)</sup>	10
Centered Load Capacity (N)	40	70	40
Straightness, Flatness ( $\mu\text{m}$ )	$\pm 0.75$	$\pm 5$	$\pm 5$
Pitch/Roll ( $\mu\text{rad}$ ) <sup>3)</sup>	$\pm 25$	$\pm 80$	$\pm 80$
MTBF (h)	20,000 hours at 25% load and with a 30% duty cycle		

<sup>1)</sup> GTS30V: -5 to +25mm

GTS70V: 0 to +70mm, when driven by ESP302 and XPS and -5 to +65 mm, when driven by SMC100CC

GTS70VCC: 0 to +70mm

<sup>2)</sup> 10 mm/s, if used with 40 N payload

<sup>3)</sup> To obtain arcsec units, divide grad value by 4.8.

# Specifications – Controller – XPS D4



## Specifications

Number of Axes	<ul style="list-style-type: none"> <li>• 1 to 8 axes of stepper, DC brush, DC brushless or linear motors using internal drives: XPS-D2: 2-axis; XPS-D4: 4-axis; XPS-D6: 6-axis; XPS-D8: 8-axis.</li> </ul>
Communication Interfaces	<ul style="list-style-type: none"> <li>• Internet protocol TCP/IP</li> <li>• One Ethernet 10/100/1000 Base-T (RJ45 connector) with fixed IP address and DHCP server for local communication</li> <li>• One Ethernet 10/100/1000 Base-T (RJ45 connector) for networking, dynamic addressing with DHCP and DNS</li> </ul>
Firmware Features	<ul style="list-style-type: none"> <li>• Powerful and intuitive, object-oriented command language</li> <li>• Native user-defined units (no need to program in encoder counts)</li> <li>• Real-time execution of custom tasks using TCL scripts</li> <li>• Multi-user capability</li> <li>• Concept of sockets for parallel processes</li> <li>• Time &amp; position spaced trigger output pulses, 0.05 Hz to 20 MHz, 5 ns accuracy</li> <li>• Data gathering at servo rate, up to 1,000,000 data entries (depending on servo rate)</li> <li>• Auto-configuration, auto-tuning and auto-scaling</li> </ul>
Motion	<ul style="list-style-type: none"> <li>• Jogging mode including on-the-fly changes of speed and acceleration</li> <li>• Synchronized point-to-point</li> <li>• Spindle motion (continuous motion with periodic position reset)</li> <li>• Line-arc mode (linear and circular interpolation incl. continuous path contouring)</li> <li>• Splines (Catmull-Rom type)</li> <li>• PT trajectories (continuous, multidimensional motion path)</li> <li>• PVT trajectories (complex trajectory based on position, velocity and time coordinates)</li> <li>• Analog tracking (using analog input as position or velocity command)</li> <li>• Master-slave including single master-multiple slaves and custom gear ratio</li> </ul>
Compensation	<ul style="list-style-type: none"> <li>• Linear error, Backlash, positioner error mapping</li> <li>• XY and XYZ error mapping</li> <li>• All corrections are taken into account on the servo loop</li> </ul>
Servo Rate	<ul style="list-style-type: none"> <li>• Adjustable up to 20 kHz</li> </ul>
I/O	<ul style="list-style-type: none"> <li>• 40 TTL inputs and 40 TTL outputs (open collector)</li> <li>• 8 synch. analog inputs <math>\pm 10</math> V, 16 bits</li> <li>• 8 synch. analog outputs <math>\pm 5</math> V, <math>\pm 10</math> V or <math>\pm 12.288</math> V (configurable), 16 bits</li> </ul>
Control Loop	<ul style="list-style-type: none"> <li>• Open loop, PI position, PIDFF velocity, PIDFF acceleration, PIDDualFF voltage</li> <li>• Variable PID's (PID values depending on distance to target position)</li> <li>• Derivative cut-off filter; 2 user-defined notch filters</li> </ul>
Trigger In	<ul style="list-style-type: none"> <li>• Hardware latch of all positions and all analog I/O's (on servo rate)</li> <li>• &lt;50 ns latency on positions</li> <li>• &lt;125 <math>\mu</math>s time jitter on analog I/O's</li> </ul>
Trigger Out	<ul style="list-style-type: none"> <li>• One high-speed position compare output only for axes 1, 2, 5 and 6 that can be either configured for position synchronized pulses or for time synchronized pulses: 5 ns accuracy, &lt;700 ns latency (from real stage position to pulse generation), 5 MHz max frequency</li> <li>• Position Compare Output (PCO):                         <ul style="list-style-type: none"> <li>– interpolation <math>\times 65536</math></li> <li>– compensated</li> </ul> </li> </ul>
Dedicated Inputs Per Axis	<ul style="list-style-type: none"> <li>• RS-422 differential inputs for A, B and I, Max. 25 MHz, over-velocity and quadrature error detection</li> <li>• 1 Vpp analog encoder input up to <math>\times 65536</math> interpolation used for servo; amplitude, phase and offset correction and synchronization</li> <li>• Low noise encoder interpolator board for nanometer MIM</li> <li>• Forward and reverse limit, home, error input</li> </ul>
Dedicated Outputs Per Axis (when using external drives)	<ul style="list-style-type: none"> <li>• 2 channel 16-bit, <math>\pm 10</math> V D/A</li> <li>• Drive enable, error output</li> </ul>
Drive Capability	<ul style="list-style-type: none"> <li>• 750 W (@ 230 VAC) total available power</li> </ul>
AC Power Requirements	<ul style="list-style-type: none"> <li>• 100–240 VAC 60/50 Hz 10 A– 6.9 A</li> </ul>

# Specifications - Refractometer DR 6000

## TECHNISCHE DATEN – DIGITALE REFRAKTOMETER

	DR6000	DR6100	DR6200	DR6300	DR6000-T
SKALEN	Brechungsindex (nD) Konzentration von Saccharose, Glukose, Fructose und Invertzucker [%Brix] Benutzerdefiniert				
MESSBEREICH	nD 1,3200–1,5800 0–95 %Brix	nD 1,3200–1,7000 0–95 %Brix	nD 1,32000–1,58000 0–95 %Brix	nD 1,32000–1,70000 0–95 %Brix	nD 1,3200–1,5800 0–95 %Brix
MESSGENAUIGKEIT	nD ±0,0001 ±0,1 %Brix		nD ±0,00002 ±0,02 %Brix		nD ±0,0001 ±0,1 %Brix
AUFLÖSUNG	nD 0,0001 0,1 %Brix		nD 0,00001 0,01 %Brix		nD 0,0001 0,1 %Brix
MESSZEIT	ca. 4 s				
MESSPRISMA	Saphir				
LICHTQUELLE	LED				
WELLENLÄNGE	589 nm				
TEMPERIERUNG	Ohne integrierte Probentemperaturung Ein Thermostat kann zur Temperaturung angeschlossen werden				
TEMPERIERBEREICH					
TEMPERIERGENAUIGKEIT					
TEMPERATURKOMPENSATION	Aktivierbar (ICUMSA oder frei definierbar)				
TEMPERATURMESSUNG	Mit integriertem Temperatursensor Pt100				
TEMPERATURMESSBEREICH	10–80 °C				
TEMPERATURMESSGENAUIGKEIT	±0,1 °C				
TEMPERATURMESSAUFLÖSUNG	0,1 °C				
METHODEN	Praktisch unbegrenzte Anzahl von Methoden einstellbar				
JUSTIERUNG	Automatisch (menügeführt)				
BEDIENUNG	5,7"-TFT-Touchscreen, 640 x 480 Pixel				
GEHÄUSE	Aluminiumguss, pulverbeschichtet				
SCHNITTSTELLEN	USB, RS-232, Ethernet				
BETRIEBSSPANNUNG	90–240 V, 47–63 Hz				
LEISTUNGS-AUFNAHME (MESSBETRIEB)	25 W				
LEISTUNGS-AUFNAHME (MAX.)	75 W				
MABE (B X H X T)	215 mm x 150 mm x 345 mm				
GEWICHT	5 kg				

A.KRÜSS Optronic GmbH  
Alsterdorfer Straße 276–278  
22297 Hamburg | Germany

Tel +49 40 514317-0  
+49 40 514317-60

E-Mail info@kruess.com  
Web www.kruess.com

# Specifications – Temperature Sensor - DS18B20

Click [here](#) for production status of specific part numbers.

## DS18B20

## Programmable Resolution 1-Wire Digital Thermometer

### General Description

The DS18B20 digital thermometer provides 9-bit to 12-bit Celsius temperature measurements and has an alarm function with nonvolatile user-programmable upper and lower trigger points. The DS18B20 communicates over a 1-Wire bus that by definition requires only one data line (and ground) for communication with a central microprocessor. In addition, the DS18B20 can derive power directly from the data line ("parasite power"), eliminating the need for an external power supply.

Each DS18B20 has a unique 64-bit serial code, which allows multiple DS18B20s to function on the same 1-Wire bus. Thus, it is simple to use one microprocessor to control many DS18B20s distributed over a large area. Applications that can benefit from this feature include HVAC environmental controls, temperature monitoring systems inside buildings, equipment, or machinery, and process monitoring and control systems.

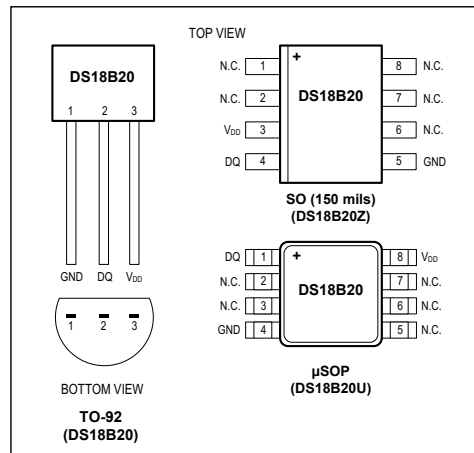
### Applications

- Thermostatic Controls
- Industrial Systems
- Consumer Products
- Thermometers
- Thermally Sensitive Systems

### Benefits and Features

- Unique 1-Wire® Interface Requires Only One Port Pin for Communication
- Reduce Component Count with Integrated Temperature Sensor and EEPROM
  - Measures Temperatures from -55°C to +125°C (-67°F to +257°F)
  - ±0.5°C Accuracy from -10°C to +85°C
  - Programmable Resolution from 9 Bits to 12 Bits
  - No External Components Required
- Parasitic Power Mode Requires Only 2 Pins for Operation (DQ and GND)
- Simplifies Distributed Temperature-Sensing Applications with Multidrop Capability
  - Each Device Has a Unique 64-Bit Serial Code Stored in On-Board ROM
- Flexible User-Definable Nonvolatile (NV) Alarm Settings with Alarm Search Command Identifies Devices with Temperatures Outside Programmed Limits
- Available in 8-Pin SO (150 mils), 8-Pin μSOP, and 3-Pin TO-92 Packages

### Pin Configurations



**Ordering Information** appears at end of data sheet.

1-Wire is a registered trademark of Maxim Integrated Products, Inc.

## Specifications – Heating Foils

Conrad Electronic  
 Artikelnr: 1216632



## Datenblatt Datasheet

## Heizfolie heater

<b>Nennspannung:</b> <i>Nominal Voltage:</i>	24 V (AC oder DC)
<b>Nennleistung:</b> <i>Effective Output:</i>	1 W +/-10%
<b>Abmessungen:</b> <i>Dimensions:</i>	20 x 51 mm 0,79" x 2,01"
<b>Oberflächentemperatur*:</b> <i>Surface temperature**:</i>	ca. 65 °C approx. 149 °F
<b>Sicherheitsthermostat:</b> <i>Safety Thermostat:</i>	nicht vorhanden <i>is not installed</i>
<b>Regelthermostat:</b> <i>Thermostat:</i>	nicht vorhanden <i>is not installed</i>
<b>Dicke:</b> <i>Thickness:</i>	ca. 0,40 mm approx. 0,02"
<b>Träger:</b> <i>Carrier:</i>	Polyesterfolie 125 µm 125 microns polyester foil
<b>Klebeband:</b> <i>Adhesive Tape:</i>	Flammhemmendes Polyesterklebeband mit Schutzpapier <i>Flame-retardant polyester tape with protective paper</i>
<b>Klebstofftyp:</b> <i>Adhesive:</i>	Modifiziertes Acrylat <i>Modified acrylate</i>
<b>Versiegelung:</b> <i>Sealing:</i>	Hochtemperaturbeständiger Dichtstoff <i>High-temperature resistant sealant</i>
<b>Elektro-Anschluss:</b> <i>Electrical Connection:</i>	Kabel FL 2x 0.25 mm <sup>2</sup> , Länge ca. 250 mm <i>cablE FL 2x 0.25 mm<sup>2</sup>, length approx. 250 mm</i>
<b>Temperaturbereich:</b> <i>Temperature Range:</i>	-40 °C bis + 95 °C (Dauerbelastung) <i>Long term loading -40 °F up to max. +203 °F</i>
<b>RoHS konform:</b> <i>RoHS compliant:</i>	Ja <i>yes</i>
<b>Schutzrad:</b> <i>Degree of Protection:</i>	IP X4
<b>Bemerkung:</b>	<b>Achtung:</b> Aufgrund hoher Heizleistung, bezogen auf die Fläche, kann die Heizfolie je nach Einbausituation, ohne ausreichende Kühlung oder Temperaturregelung, überhitzen und dadurch zerstört werden!
<b>Comment:</b>	<b>Attention:</b> Overheating and the resulting destruction, as a consequence of high heating power of the heating foil, can be prevented by providing enough cooling or temperature control, depending on the positioning of the high power heating foil.
	* Heizfolie frei in der Luft hängend, die Wärmeabgabe erfolgt nur an die Umgebungsluft
	** Temperature was measured with the heater suspended freely in the air, the heat was only given off to the ambient air

Rev.-  
 08/14

# Specifications – Peltier-Element -



## Specification of Thermoelectric Module

### TEC1-12706

#### Description

The 127 couples, 40mm × 40mm size single stage module is made of selected high performance ingots to achieve superior cooling performance and greater delta T up to 70°C Designed for superior cooling and heating. If higher operational temperature is required, please specify. We can design and manufacture custom made modules according to your requirements. Please contact us for further information. Minimums do apply.

#### Features

- High effective cooling and efficiency.
- No moving parts, no noise, and solid-state
- Compact structure, small in size, light in weight
- Environmental friendly, RoHS compliant
- Precise temperature control
- Exceptionally reliable in quality, high performance

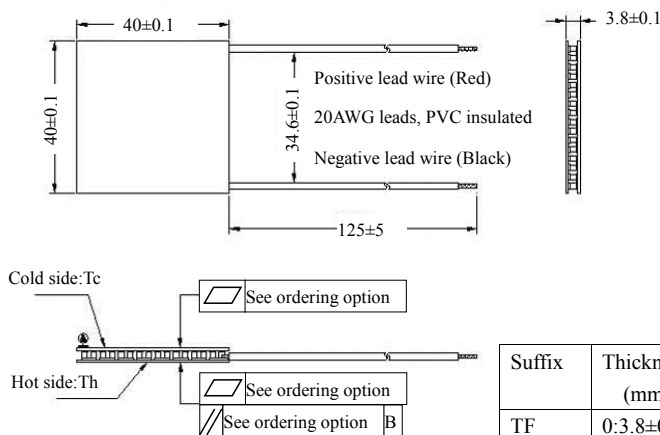
#### Application

- Food and beverage service refrigerator
- Portable cooler box for cars
- Liquid cooling
- Temperature stabilizer
- Photonic and medical systems

#### Performance Specification Sheet

Th(°C)	27	50	Hot side temperature at environment: dry air, N <sub>2</sub>
DT <sub>max</sub> (°C)	70	79	Temperature Difference between cold and hot side of the module when cooling capacity is zero at cold side
U <sub>max</sub> (Voltage)	16.0	17.2	Voltage applied to the module at DT <sub>max</sub>
I <sub>max</sub> (amps)	6.1	6.1	DC current through the modules at DT <sub>max</sub>
Q <sub>Cmax</sub> (Watts)	61.4	66.7	Cooling capacity at cold side of the module under DT=0 °C
AC resistance(ohms)	1.8 ~ 2.2	2.0~2.4	The module resistance is tested under AC

#### Geometric Characteristics Dimensions in millimeters



#### Sealing Option

Suffix	Sealant
NS	No sealing
SS	Silicone sealant
EPS	Epoxy
OS	Customer specify sealing other than above

#### Ordering Option

Suffix	Thickness (mm)	Flatness/ Parallelism (mm)	Lead wire length(mm) Standard/Optional length
TF	0:3.8±0.1	0:0.035/0.035	125±1/Specify
TF	1:3.8±0.05	1:0.025/0.025	125±1/Specify
TF	2:3.8±0.03	2:0.015/0.015	125±1/Specify

Eg. TF01: Thickness 3.8 ± 0.1 (mm) and Flatness 0.025 / 0.025 (mm)

#### Additional

Ceramic material: Alumina (Al<sub>2</sub>O<sub>3</sub>, white 96%)  
 Solder tinning: Bismuth Tin (BiSn) M.P. 138 °C

## Specifications – Temperature Sensor – Trotec T210



## Technische Daten

Parameter	Wert
Modell	T210
<b>Temperatur</b>	
Sensortyp	NTC
Messbereich	-20 °C bis +50 °C oder -4 °F bis 122 °F
Genauigkeit	+/-0,4 °C oder +/-0,7 °F
Auflösung	0,1 °C oder 0,1 °F
<b>Relative Luftfeuchtigkeit</b>	
Sensortyp	kapazitiv
Messbereich	0,0 bis 100,0 % r.F.
Genauigkeit	±2 % r.F.
Auflösung	0,1 % r.F.
<b>Allgemeine technische Daten</b>	
Display	LCD
Messfrequenz	2 mal pro Sekunde
Schnittstelle	USB
Betriebsbedingungen	0 °C bis 50 °C bei <95 % r.F. (nicht kondensierend)
Lagerbedingungen	-30 bis 60°C bei <95 % r.F. (nicht kondensierend)
Energieversorgung	4 x 1,5 V, AA Batterien
Gewicht	ca. 270 g
Abmessungen (Länge x Breite x Höhe)	202 mm x 63 mm x 35 mm

## Lieferumfang

- 1 x Gerät T210
- 4 x Batterie 1,5 V, Typ AA
- 1 x Werkprüfzeugnis
- 1 x Kurzanleitung

## Transport und Lagerung

**Hinweis**

Wenn Sie das Gerät unsachgemäß lagern oder transportieren, kann das Gerät beschädigt werden. Beachten Sie die Informationen zum Transport und zur Lagerung des Gerätes.

**Transport**

Transportieren Sie das Gerät trocken und geschützt, z. B. in einer geeigneten Tasche, um es vor Einwirkungen von außen zu schützen.

**Lagerung**

Halten Sie bei Nichtbenutzung des Gerätes die folgenden Lagerbedingungen ein:

- trocken und vor Frost und Hitze geschützt
- an einem vor Staub und direkter Sonneneinstrahlung geschützten Platz
- die Lagertemperatur entspricht dem im Kapitel Technische Daten angegebenen Bereich.
- Batterien aus dem Gerät entfernen.

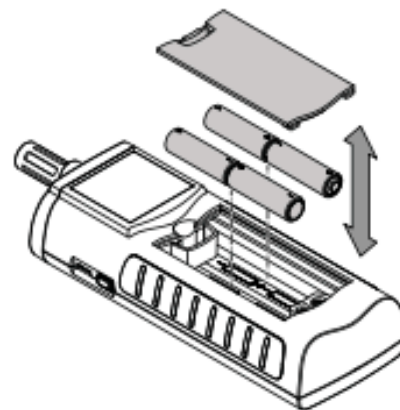
## Bedienung

**Batterien einsetzen**

Setzen Sie vor dem ersten Gebrauch die mitgelieferten Batterien ein.

**Vorsicht**

Vergewissern Sie sich, dass die Oberfläche des Gerätes trocken und das Gerät ausgeschaltet ist.



1. Entfernen Sie den Batteriefachdeckel (3).
2. Setzen Sie die Batterien polungsrichtig in das Batteriefach ein.
3. Setzen Sie den Batteriefachdeckel (3) ein.  
⇒ Das Gerät kann jetzt eingeschaltet werden.

# Specifications – DC Powersupply – HP E3610 A

**Specifications**

	E3610A	E3611A	E3612A	E3614A	E3615A	E3616A	E3617A	E3620A	E3630A
<b>Features</b>	Dual range, 10 turn pots, Constant Voltage (CV), Constant Current (CC) modes.			Adjustable overvoltage protection, voltage & resistance programming, remote sense, rear outputs, ten turn pots, CV, CC modes. Multiple supplies can be connected for tracking or higher power.			Isolated dual outputs, 10 turn pots CV, CL		Tracking, CV, CL ( $\pm 20$ V) CV, CF (+6 V)
<b>Number of outputs</b>	1							2	3
<b>Number of output Ranges</b>	2	2	2	1	1	1	1	1	1
<b>dc Output Rating</b>	8 V, 3 A 15 V, 2 A	20 V, 1.5 A 35 V, 0.85 A	60 V, 0.5 A 120 V, 0.25 A	8 V, 6 A	20 V, 3 A	35 V, 1.7 A	60 V, 1 A	25 V, 1 A 25 V, 1 A	+6 V, 2.5 A +20 V, 0.5 A -20 V, 0.5 A
<b>Load and Line Regulation</b>	<0.01% + 2 mV								
<b>Ripple and Noise</b> (20 Hz to 20 MHz)									
Normal mode voltage	<200 $\mu$ Vrms, <2 mVpp			<200 $\mu$ Vrms, <1 mVpp				<350 $\mu$ Vrms, <1.5 mVpp	
Normal mode current	<200 $\mu$ Vrms / 1 mA			<0.02%+ 3 mA	<0.02%+ 1.5 mA	<0.02%+ 1 mA	<0.02%+ 0.5 mA	–	
Common mode current	not specified							<1 $\mu$ Arms	
<b>Transient Response Time:</b>	<50 $\mu$ sec following change in output current from full load to half load for output to recover to within:								
	10 mV				15 mV				
<b>Meter Accuracy</b>	$\pm 0.5\%$ + 2 counts at 25°C $\pm 5^\circ$ C								
<b>Meter Resolution</b>									
Voltage	10 mV	100 mV	100 mV	10 mV	10 mV (0-20 V), 100 mV (>20 V)				10 mA
Current	10 mA	10 mA	1 mA	10 mA	10 mA	1 mA	1 mA	1 mA	10 mA
<b>Isolation</b>	240 Vdc								

**Supplemental Characteristics**

<b>Control Mode</b>	CV/CC						CV/CL	CV/CL ( $\pm 20$ V) CV/CF (+6 V)
<b>Temperature Coefficient per °C</b>								
Voltage	<0.02% + 1 mV		<0.02% + 500 $\mu$ V				<0.02% + 1 mV	
Current	<0.02% + 2 mA		<0.02% + 3 mA	<0.02% + 1.5 mA	<0.02% + 1 mA	<0.02% + 0.5 mA	–	
<b>Output Drift</b>								
Voltage	Less than 0.1% + 5 mV total drift for 8 hours after an initial warm-up of 30 minutes.							
Current	Less than 0.1% + 10 mA total drift for 8 hours after an initial warm-up of 30 minutes.							
<b>Temperature Range</b>								
	0 to 40°C for full rated output. Derate output current 1% per °C between 40°C and 55°C						Derate output current 3.3% per °C	
<b>Cooling</b>	Convection cooling							
<b>Isolation</b>	$\pm 240$ Vdc							
<b>AC Input</b>	100 Vac $\pm 10\%$ , 47–63 Hz (opt. 0E9) 115 Vac $\pm 10\%$ , 47–63 Hz (std) 230 Vac $\pm 10\%$ , 47–63 Hz (opt. 0E3)							
<b>Weight</b>	3.8 kg (8.4 lb.) net, 5.1 kg (11.3 lbs) shipping		5.5 kg (12.1 lb.) net, 6.75 kg (14.9 lbs) shipping				Same as E3610A	
<b>Size</b>	91 mm H x 213 mm W x 319 mm D 3.6" H x 8.4" W x 12.6" D		91 mm H x 213 mm W x 373 mm D 3.6" H x 8.4" W x 14.7" D					
<b>Warranty</b>	1 year							
<b>Product Regulation</b>	Certified to CSA 22.2 No. 231; conforms to IEC 1010-1; carries CE mark; complies with CISPR-11, Group 1, Class A							